

THE SOLAR MAXIMUM MISSION ATLAS OF GAMMA-RAY FLARES

W. THOMAS VESTRAND

Space Science Center, Morse Hall, University of New Hampshire, Durham, NH 03824

GERALD H. SHARE AND RONALD J. MURPHY

Naval Research Laboratory, Code 7652, 4555 Overlook Avenue, SW, Washington, DC 20375

DAVID J. FORREST

Space Science Center, Morse Hall, University of New Hampshire, Durham, NH 03824

ERICH RIEGER

Max-Planck-Institut für extraterrestrische Physik, Garching, Germany

EDWARD L. CHUPP

Space Science Center, Morse Hall, University of New Hampshire, Durham, NH 03824

AND

GOTTFRIED KANBACH

Max-Planck-Institut für extraterrestrische Physik, Garching, Germany

Received 1998 April 2; accepted 1998 September 21

ABSTRACT

We present a compilation of data for all 258 gamma-ray flares detected above 300 keV by the Gamma Ray Spectrometer (GRS) aboard the *Solar Maximum Mission* satellite. This gamma-ray flare sample was collected during the period from 1980 February to 1989 November; covering the latter half of the 21st solar sunspot cycle and the onset of the 22d solar sunspot cycle. We describe the SMM/GRS instrument, its in-orbit operation, and the principal data reduction methods used to derive the gamma-ray flare properties. Utilizing measurements for 185 flares that were sufficiently intense to allow the derivation of gamma-ray spectra, we present an atlas of time profiles and gamma-ray spectra. The flare parameters derived from the gamma-ray spectra include bremsstrahlung fluence and best-fit power-law parameters, narrow nuclear line fluence, positron annihilation line fluence, neutron capture line fluence, and an indication of whether or not emissions greater than 10 MeV were present. Since a uniform methodology was adopted for deriving the parameters, this atlas should be very useful for future statistical and correlative studies of solar flares.

Subject headings: catalogs — gamma rays: bursts — Sun: flares

1. INTRODUCTION

1.1. Background

The intense explosive releases of energy in the solar atmosphere that we call solar flares are known to rapidly accelerate electrons and ions to high energies, and to generate gamma rays and high-energy neutrons as the accelerated particles interact with the ambient material. It had long been recognized that measurements of these uncharged secondary emissions, who freely traverse the interplanetary medium, would allow one to probe directly the properties of the highest energy particles near the flare site and could provide a firm observational foundation for understanding particle acceleration during flares (Biermann et al. 1951; Morrison 1958). However, before the 21st Solar Maximum, direct knowledge of neutral high-energy flare emission was based almost entirely on the measurements of only two flares by gamma-ray detectors on the *OSO-7* satellite (Chupp et al. 1973). Our understanding of high-energy flare emission and flare particle acceleration was therefore primarily conjecture based on radio observations, X-ray observations, and solar energetic particle measurements made well away from the flare site.

The launching, during the 21st Solar Maximum, of sensitive high-energy detectors on both the *Solar Maximum Mission* (SMM) satellite (Bohlin et al. 1980) and the *Hinotori* satellite (Okudaira et al. 1981) dramatically changed the observational status of high-energy solar physics. For, con-

trary to even the most optimistic expectations of the instrument teams, gamma-ray flares (GRFs) were found to be quite common during periods of high solar activity. During their lifetimes, the *Hinotori* instrument detected about 40 flares at energies above 300 keV and the gamma-ray spectrometer (GRS) aboard *SMM* detected 258 flares above 2300 keV. This surprisingly large number of events initiated a new era where one could statistically study GRFs as a class, and thereby avoid the risk of incorrect generalizations driven by extrapolation of properties potentially associated with only a handful of giant flares. The gamma-ray flare spectra measured by *SMM/GRS* that are displayed in this atlas show lines from prompt nuclear de-excitation, neutron capture, and positron annihilation; as well as continuum emission from pion decay, nuclear de-excitation, and electron bremsstrahlung. Concurrently with the collection of these rich flare spectra, theoretical studies of high-energy flare processes yielded useful gamma-ray diagnostics for assaying properties of the accelerated flare particles and the target material (e.g., Ramaty & Murphy 1987). The bringing together of a large database of flare gamma-ray observations and well-developed diagnostic techniques, permitted the first large-scale observational tests of models for flare particle acceleration.

The power of gamma-ray measurements as a probe of particle acceleration processes was clearly demonstrated by the way in which early *SMM/GRS* measurements changed our understanding of particle acceleration by solar flares.

For example, the discovery of gamma-ray emission from flares of even rather modest size made it clear that one could not relegate particle acceleration to the category of pathology associated with giant flares. Further, the measurements showed that the acceleration of particles to high energies is not, as was previously thought, a slow process requiring minutes to an hour, but is instead a rapid process that can energize electrons to relativistic energies in less than 2 seconds as well as boost ions to energies as high as a few GeV in less than 16 seconds (Forrest & Chupp 1983; Chupp et al. 1987).

The early *SMM/GRS* observations also gave us a glimpse of the rich phenomenology associated with particle acceleration and the generation of high-energy photons. Statistical studies of the high-energy emission provided evidence for radiation directivity (Rieger et al. 1983; Vestrand et al. 1987). Modeling of the temporal evolution observed at high energies showed that the transport of particles in flare loops could produce signatures that were previously attributed to acceleration (e.g., Ryan 1986; Mandzhavidze & Ramaty 1992). Comparison of the characteristics of interacting particles with those measured in space showed a large scatter in their properties and indicated that typically most of the gamma-ray-producing particles remain trapped at the Sun (e.g., Cliver et al. 1989). Studies of the observed gamma-ray lines also gave us valuable information about accelerated particle compositions, flare energetics, and about elemental and isotopic abundances in the solar atmosphere (Murphy et al. 1991; Ramaty et al. 1995; Share & Murphy 1997).

1.2. The Present Atlas

The GRS monitored solar X-ray and gamma-ray emission almost continuously from launch in 1980 February until increased atmospheric drag, associated with the onset of the 22d Solar Maximum, led to satellite reentry in 1989 November. The 258 flares detected at energies greater than 300 keV during the mission lifetime constitute a database which in many ways is still unsurpassed for studying the high-energy phenomena associated with solar flares. The objective of this atlas is to present, for the first time, a complete listing of the key physical parameters for the gamma-ray flares¹ detected by *SMM/GRS* along with their spectra and time histories. Since we plan to use these flare parameters in future statistical studies of gamma-ray flares, an effort was made to adopt a uniform methodology and to derive the flare parameters in a consistent way for all events. In addition its utility as a database for studying gamma-ray emission from flares, we expect this atlas to be useful for correlative studies of other flare phenomena, such as coronal mass ejection (CME) and solar energetic particle (SEP) measurements.

In § 3 we present the complete list of all gamma-ray flares detected by *SMM/GRS* and a discussion of how the flare parameters were derived. In § 4 we present an atlas of time histories and spectra for flares that were intense enough to allow spectroscopic study. First, however, we review the

¹ There is a vagueness in the current usage of the term "gamma-ray flare." In this atlas, we use the term to mean a flare from which photons with energies greater than 300 keV were detected. Using that definition, gamma-ray flares are therefore flares which are associated with energetic ion and/or relativistic electron acceleration.

SMM/GRS instrument properties and on orbit operation of the instrument in § 2.

2. THE GAMMA-RAY SPECTROMETER ABOARD THE SOLAR MAXIMUM MISSION SATELLITE

2.1. Instrument Properties

The *SMM/GRS* instrument (see Fig. 1) was composed of three sensor systems, which together measured the spectra of flare X-rays and gamma rays over the energy range from 14 keV to 140 MeV (Forrest et al. 1980). These three sensor systems were the "Main-Channel" Spectrometer (MCS), the High Energy Monitor (HEM), and the X-Ray Spectrometer (XRS).

The MCS, which measured gamma rays with energies between 300 keV and 9 MeV, was the primary sensor system for *SMM/GRS*. This sensor system was composed of seven 7.6 cm × 7.6 cm NaI(Tl) scintillation detectors housed in an anticoincidence well which was constructed from a 2.5 cm thick by 25 cm diameter CsI(Na) annulus and a 7.5 cm thick CsI(Na) backplate. The anticoincidence well was operated with an energy threshold of 100 keV and provided rejection of background photons entering from side and backward directions as well as strong suppression of the Compton continuum photons associated with incomplete energy deposition in the seven central scintillators. Energetic particle rejection was provided by veto signals from 1 cm thick front and back plastic shields with 500 keV energy thresholds and the CsI anticoincidence well with an energy threshold of 100 keV. To minimize pulse pile-up effects generated by the intense flare X-ray flux, the full entrance aperture of the MCS was covered by a Al-Pb filter with a 50% transmission energy of 250 keV.

The combination of thick detectors with a large total geometric area (317 cm^2) and an energy resolution that was quite good for a scintillation spectrometer ($> 7\%$ FWHM at 662 keV) gave the MCS unprecedented capabilities for flare gamma-ray spectroscopy. Further, the stability of the MCS was quite remarkable and allowed collection of flare spectra with a constant response throughout the mission. In fact, the instrument response was so stable that *SMM/GRS* was able to extend its scientific mission beyond solar flare studies to include long time base surveys of galactic gamma-ray line emission from Al^{26} and positron annihilation (see, e.g., Share et al. 1988). The stability of the MCS was achieved by placing the seven detectors in a closed gain-control loop that employed gated ${}^{60}\text{Co}$ calibration sources to force each of the detectors to a common gain (Gleske & Forrest 1980). The outputs of the gain-controlled detectors were summed together every 16.384 s to form two separate 476 channel energy spectra—a "singles" spectrum and a "multiples" spectrum. The "singles" spectrum represented the energy loss distribution for events that excited only one of the seven NaI detectors, and the "multiples" spectrum gave the energy loss distribution for events that deposited energy in more than one of the detectors. The spectra used in this atlas were formed by summing together the "singles" and "multiples" spectra. The basic time resolution for MCS spectral measurements was 16.384 s clock time. The MCS system also measured the count rate in a 50 keV wide "burst window" near 300 keV every 64 ms and in three "Main Channel Windows" covering the energy band from 4.1 to 6.4 MeV every 2.048 s. Furthermore, the live time of the detection circuits was continuously measured so that

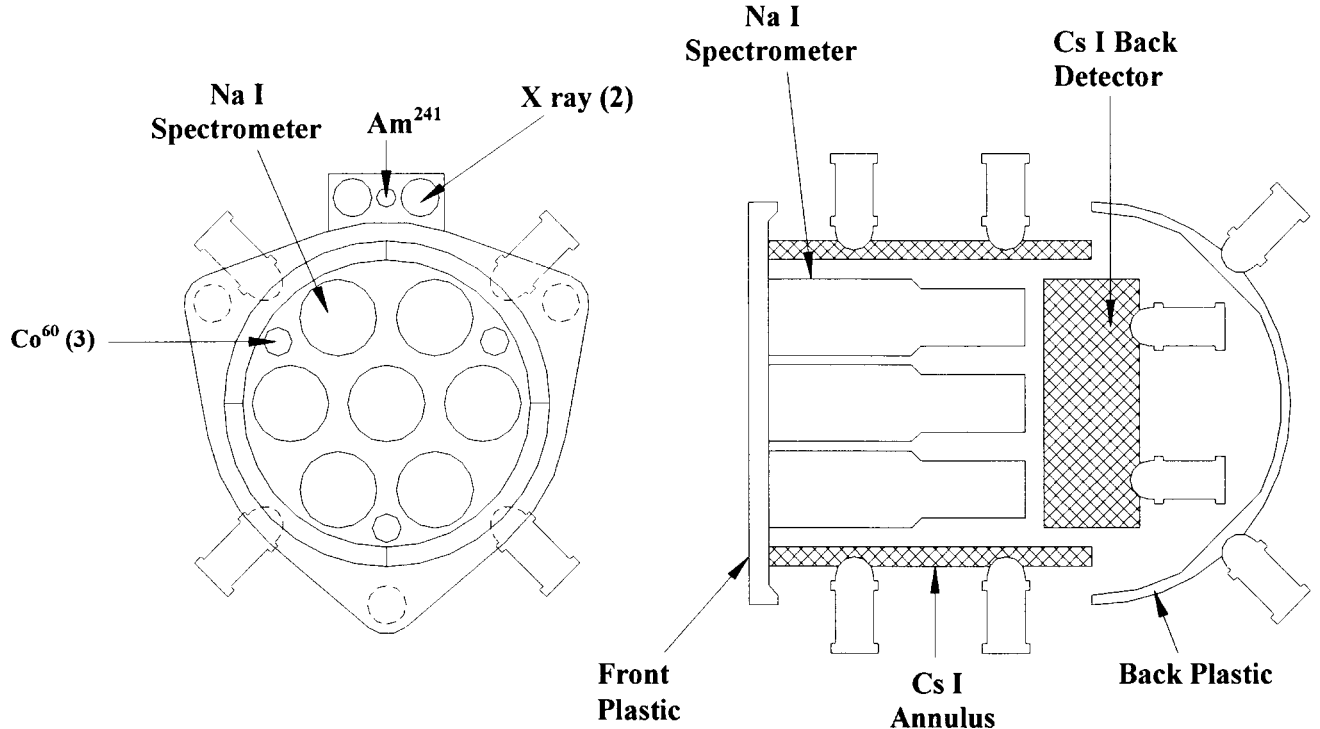


FIG. 1.—Schematic drawing of the *SMM*/GRS instrument showing the location of the seven NaI(Tl) detectors that comprise the Main Channel Spectrometer (MCS) as well as the thick CsI(Na) backplate which is used together with the NaI detectors to form the High Energy Monitor (HEM). The relative locations of the X-ray detectors, shield elements, and calibration detectors are also shown.

the observed count spectra could be corrected for instrument dead time.

The High-Energy Monitor (HEM) measured flare photon spectra in the energy band from 10 to 140 MeV and was sensitive to incident neutrons with energies greater than 20 MeV. HEM events were formed from the union of 10–100 MeV energy deposits measured in the forward NaI detector array together with deposits measured in the same energy band by the 25 cm × 7.5 cm CsI(Na) backplate. To reject background events, the HEM output was registered only if it was not in coincidence with an energy deposit exceeding 100 keV in the plastic shields or an energy deposit exceeding 2.5 MeV in the CsI annulus.

The final sensor system, XRS, was designed to provide the measurements of hard X-ray emission from large flares that is needed to place the gamma-ray measurements in their proper observational context. The XRS sensor system consisting of two detectors, X1 and X2, employing identical 8 cm² × 0.6 cm NaI crystals. Each detector accumulated a four channel energy loss spectrum every 1.024 s with an energy resolution of 30% (FWHM) at 60 keV. In order to monitor spectral distortion from instrumental pulse pileup during intense flares, the identical detectors were covered by different entrance filters. One detector (X1) had an Al filter with a 50% transmission energy of 14 keV, and the other detector (X2) had an Al-Fe filter with a 50% transmission energy of 35 keV. The X1 and X2 detectors had energy ranges of 14–114 keV and 14–200 keV, respectively. The nominal channel boundaries were arranged so that the fourth channel of X1 and the third channel of X2 both covered the identical 56–114 keV band. The occurrence of different count rates in those two channels was therefore a clear signature of pulse pile-up and allowed us to identify those spectra that are distorted by pulse pile-up effects.

2.2. Instrument Operation

The *SMM* satellite was deployed into a low Earth orbit at an altitude of ∼570 km on 1980 February 14, and GRS was operated, with a few short duration exceptions, in essentially the same mode from that day until satellite reentry on 1989 November 29. The GRS collected data almost continuously during each nominal 90 minute orbit. Regular interruption of the data stream occurred whenever the satellite was located at a position within the South Atlantic Anomaly (SAA). During those intervals the instrument high voltage was switched off to protect the instrument from overload by the intense particle background. The other routine interruption was for five minute in-flight calibration sessions. Early in the mission the in-flight calibrations were performed twice during each orbit—just after sunset and just before sunrise. Later in the mission this calibration frequency was reduced to once each orbit—just before sunrise, and finally, after the stability of the GRS was well established, to once every 24 hours.

As a dedicated solar observatory, the spacecraft viewing direction was normally kept oriented toward the Sun's location, including the interval of Earth occultation that occurred during each orbit. However, approximately 9 months after *SMM* was deployed, the attitude control system partially failed, compromising the fine pointing capability of the spacecraft. From the time of that failure on 1980 November 25 until the repair by astronauts of *Challenger* mission 41-C in 1984 April, the pointing axis of the *SMM* satellite oscillated about the solar direction with an angular excursion as large as 15°. That oscillation of the pointing axis varied the solar-viewing effective area of all X-ray instruments aboard *SMM*. For *SMM*/GRS angular excursions of more than 7° placed the aluminum frame of

the XRS window along the detector's line of sight to the Sun. The 0.45 g cm^{-2} thickness of the frame significantly attenuated emission in the lowest energy XRS channel, 14–21 keV, but always generated less than 11% attenuation for the 56–199 keV energy band. The broad field of view of the MCS gamma-ray detector limited the variations in the solar-viewing effective area to less than 3% at 300 keV and less than 1% above 1 MeV. Corrections for the early mission pointing oscillations are therefore not significant for the energy channels presented in the time histories of § 4.

3. DERIVATION OF GAMMA-RAY FLARE PROPERTIES

Table 1 is a complete listing of all 258 gamma-ray flares that were detected during the nearly 10 years of *SMM/GRS* operation. The table presents the occurrence time, *GOES* X-ray class, $H\alpha$ class, and heliocentric angle for each gamma-ray flare in the sample. For the subset of 185 flares that were strong enough for spectral analysis, we list bremsstrahlung fluence and best-fitting power-law parameters, narrow nuclear line fluence, neutron capture line fluence, and whether or not emissions greater than 10 MeV were present. In this section we discuss the methodology employed for identifying gamma-ray flares in the *SMM/GRS* data stream and deriving the properties listed in Table 1.

3.1. Gamma-Ray Flare Identification

We employed two approaches to search the continuous GRS data stream for high-energy transients. The first approach employed a computer automated search for greater than 5.7σ increases in the 350–800 keV count rate at the native time resolution (16.384 s) of the MCS system. This search technique was complemented by a second approach that employed a visual examination of the MCS count rates in two energy bands near 300 and 500 keV with widths of 80 and 100 keV, respectively. Both techniques identified candidate transients that were subsequently studied and classified on the basis of their response measured in the *SMM/GRS* sensor systems and shield systems. After filtering out candidate transients that were data and telemetry errors, the transients in the data stream could be classified as solar flares, cosmic gamma-ray bursts, particle precipitation events, and “man-made” events associated with satellite reactor encounters.

The relative response of the *SMM/GRS* sensor and shield systems allowed straightforward classification for most of the detected transients. For example, the plastic anti-coincidence shields were rather insensitive to photons but quite sensitive to charged particles. As a consequence, particle precipitation events, which typically occurred at locations with low geomagnetic rigidity during geomagnetically disturbed periods, were easily identified by their high shield count rates and relatively weak MCS response. The transients associated with particles and radiation emitted by Soviet nuclear reactor-powered satellites (Share et al. 1989) occurred primarily ($\sim 80\%$) in 1987 and 1988. Those reactor-generated transients displayed a complex phenomenology with three types of events (Rieger et al. 1989), but all types could be straightforwardly identified by their recurrence periodicities and unusual spectral properties. The remaining classes of transients, cosmic gamma-ray bursts and solar flares, were distinguished primarily by their properties at X-ray energies. Gamma-ray bursts are relatively weak X-ray emitters and typically have X-ray spectra

that are harder than those measured for flares. This, combined with the fact that the XRS had a much narrower field of view than the MCS, resulted in gamma-ray bursts typically showing no detectable or relatively low count rates in the low-energy X-ray channels. On the other hand, it is well known that solar flares generate strong thermal X-ray emission. By definition, solar flares are “a transient increase in $H\alpha$ brightness to at least two times chromospheric intensity, usually impulsive, accompanied by some increase in the X-ray or radio flux from the Sun” (Zirin 1989, p. 347). Our working definition for identification of a gamma-ray flare (GRF) was therefore the following: transient photon emission at energies above 300 keV from the direction of the Sun which is accompanied by strong thermal X-ray emission and, normally, by a $H\alpha$ flare.

3.2. Position Determination and $H\alpha$ /GOES Association

An important parameter for flare studies is the flare viewing angle. If we assume that the flare symmetry axis is parallel to the solar surface normal at the flare position, then, for a satellite in low Earth orbit like *SMM*, the viewing angle is essentially the heliocentric angle of the flare. Each position was determined by searching the NOAA Solar-Geophysical Data Comprehensive Reports for a temporally coincident $H\alpha$ flare and then assigning the $H\alpha$ position to the GRF. Typically we found that a given GRF was temporally coincident with a single $H\alpha$ flare, and that the high-energy emission peaks at, or slightly before, the peak of the $H\alpha$ emission. Whenever more than one $H\alpha$ flare showed a time coincidence, the position of the most significant flare, as measured by IAU importance class, was selected. This criterion was employed because GRFs that are temporally isolated were generally found to have high $H\alpha$ importance. We associated 250 GRFs in the *SMM/GRS* sample with $H\alpha$ flares and determined their positions on the solar disk in this manner. These disk positions were then used to derive the heliocentric angle of each GRF using the procedure described in Appendix B of Vestrand et al. (1987).

All but two of the GRFs were associated with soft X-ray flares detected by the *GOES* solar X-ray monitoring detectors. The association with a *GOES* event was made on the basis of GRF temporal coincidence with an event listed in the NOAA Solar-Geophysical Data reports. Again, as for $H\alpha$ flares, the gamma-ray emission was typically found to reach maximum intensity at, or slightly before, the peak intensity for the soft X-ray emission.

3.3. Spectral Parameters

The first step in deriving flare gamma-ray spectra was accumulation of the MCS count spectrum for each GRF. The integration interval was identified by visual inspection of the time profile in the 300–800 keV band. We also summed spectra into 1 minute intervals and did fits looking for delayed 2.22 and 0.5 MeV line emission from the flares. The latter method was more sensitive and caused us to increase the accumulation interval for many flares. Bad data, bit errors, and, for intense flares, intervals comprised by instrumental gain shifts, were dropped from the accumulations. The integration time interval selected for each fitted flare is denoted on the corresponding time history plot.

The next step was subtraction of background counts from the measured MCS count spectra. This background count spectrum depended on the satellite's proximity to the SAA, the geomagnetic cutoff rigidity, and the detector-

TABLE 1
GAMMA-RAY FLARE LIST

Date (1)	Time UT (2)	Duration (s) (3)	Position (4)	GOES/H α Class (5)	Θ (deg) (6)	Power-Law Amplitude (7)	Power-Law Index (8)	Bremsstrahlung Fluence (9)	Narrow Nuclear Line Fluence (10)	0.511 MeV Line Fluence (11)	2.23 MeV Line Fluence (12)	Comments (13)
1980 Mar 29 ...	09:17:40	33	N27E42	C9.6/SB	53	1.13 ± 0.24	-4.16 ± 0.89	3.5 ± 1.3
1980 Mar 29 ...	09:55:05	32	N07W10	M1.1/SB	17	3.22 ± 0.26	-4.51 ± 0.36	8.8 ± 1.1
1980 Apr 26 ...	20:31:30	...	S17E61	M5.0/1B	61
1980 Apr 28 ...	20:39:55	...	S14W69	C9.9/SB	69
1980 May 9 ...	07:12:17	...	S21W32	M7.2/1B	36
1980 May 21 ...	20:55:40	82	S14W15	X14/2B	19	1.89 ± 0.16	-3.54 ± 0.28	18.3 ± 2.6
1980 Jun 4 ...	06:54:19	48	S14E59	M6.7/SB	60	3.62 ± 0.14	-2.00 ± 0.04	50.3 ± 3.2
1980 Jun 6 ...	11:42:32	...	S12E33	C3.6/SB	35
1980 Jun 6 ...	23:34:43	...	S13E35	C3.5/1N	37
1980 Jun 7 ...	01:17:16	81	N13W72	M2.5/SB	72	2.94 ± 0.09	-2.53 ± 0.06	46.6 ± 2.3
1980 Jun 7 ...	03:11:57	343	N12W74	M7.6/SB	74	6.34 ± 0.17	-3.16 ± 0.05	301.6 ± 10.6	10.5 ± 2.3	2.1 ± 1.1	5.7 ± 0.9	3, 5
1980 Jun 21 ...	01:18:20	491	N20W90	X2.6/1B	89	1.71 ± 0.11	-2.65 ± 0.10	152.2 ± 13.5	3.0 ± 2.0	8.8 ± 1.0	7.0 ± 0.9	...
1980 Jun 29 ...	10:41:40	82	S27W90	M4.2/1F	91	1.10 ± 0.12	-2.48 ± 0.20	18.2 ± 3.2
1980 Jul 1 ...	16:26:52	163	S12W37	X2.5/1B	40	5.21 ± 0.25	-3.47 ± 0.10	103.0 ± 6.3	3.5 ± 1.5	0.8 ± 0.7	2.1 ± 0.6	...
1980 Jul 21 ...	02:55:47	98	S15W60	M8.0/1B	63	3.51 ± 0.10	-2.54 ± 0.5	66.5 ± 3.0
1980 Aug 31 ...	12:48:31	245	N12E28	M2.8/SB	28	0.34 ± 0.05	-2.82 ± 0.34	13.8 ± 3.3
1980 Sep 4 ...	02:01:00	...	S07W18	M6.4/2B	23
1980 Sep 8 ...	05:03:50	65	N11E90	M3.4/1N	89	0.71 ± 0.12	-2.80 ± 0.38	7.7 ± 2.1
1980 Oct 9 ...	11:23:53	278	S13E51	M8.9/1B	54	0.33 ± 0.05	-2.72 ± 0.34	15.9 ± 4.1
1980 Oct 20 ...	18:31:58	...	S17E45	M1.1/SB	50
1980 Oct 23 ...	10:34:01	130	N06W75	M1.0/SB	75	0.51 ± 0.06	-2.31 ± 0.20	15.0 ± 3.0
1980 Nov 2 ...	14:18:56	16	S20W59	C3.3/SB	63	0.82 ± 0.19	-2.48 ± 0.45	2.6 ± 1.0
1980 Nov 5 ...	22:32:50	...	N11E07	M4.0/1B	10
1980 Nov 6 ...	03:44:07	294	S13E70	X9.0/2N	72	12.04 ± 0.24	-2.90 ± 0.03	557.9 ± 14.3	10.5 ± 2.2	1.8 ± 1.1	8.9 ± 0.9	...
1980 Nov 7 ...	02:04:12	180	N07W11	X2.5/2B	12	1.67 ± 0.19	-4.07 ± 0.31	29.4 ± 4.5	2.4 ± 1.2	1.5 ± 0.7	0.9 ± 0.5	...
1980 Nov 8 ...	14:52:30	...	S09E37	M2.4/1B	39
1980 Nov 11 ...	17:43:45	...	S11W71	M4.8/2B	72
1980 Nov 12 ...	04:48:32	327	N10W72	X2.5/2B	72	0.35 ± 0.04	-2.11 ± 0.15	30.0 ± 5.6
1980 Nov 15 ...	15:42:27	...	S12W53	X1.9/1B	55
1980 Nov 16 ...	09:04:20	...	N17W03	M8.7/2B	15
1980 Dec 17 ...	08:45:14	...	N10E07	C7.6/SB	13
1980 Dec 18 ...	19:21:17	32	N07W11	C5.7/SN	14	1.17 ± 0.22	-3.01 ± 0.49	5.6 ± 1.7
1980 Dec 23 ...	21:15:03	...	M3.0/-
1981 Jan 28 ...	04:11:48	147	S13E55	M8.9/1B	55	0.34 ± 0.05	-1.97 ± 0.17	14.8 ± 3.6
1981 Feb 10 ...	02:23:37	49	N09E14	C4.4/SN	21	0.39 ± 0.11	-2.37 ± 0.48	4.2 ± 2.0

TABLE 1—Continued

Date (1)	Time UT (2)	Duration (s) (3)	Position (4)	GOES/H α Class (5)	Θ (deg) (6)	Power-Law Amplitude (7)	Power-Law Index (8)	Bremsstrahlung Fluence (9)	Narrow Nuclear Line Fluence (10)	0.511 MeV Line Fluence (11)	2.23 MeV Line Fluence (12)	Comments (13)
1981 Feb 10 ...	03:20:09	48	S14W82	M2.1/SN	81	0.65 ± 0.11	-2.55 ± 0.33	6.0 ± 1.7
1981 Feb 17 ...	21:46:02	114	N20W20	X1.0/1B	33	1.09 ± 0.11	-3.34 ± 0.29	15.9 ± 2.5
1981 Feb 20 ...	06:44:58	...	N19W50	X2.4/2N	56
1981 Feb 24 ...	00:10:27	48	S13E86	M5.2/SB	85	0.89 ± 0.14	-3.10 ± 0.42	6.1 ± 1.6
1981 Feb 24 ...	19:36:11	245	S14E75	X1.4/2B	74	0.47 ± 0.04	-2.33 ± 0.15	25.5 ± 4.0
1981 Feb 26 ...	14:24:29	114	S12E53	X1.8/SB	52	4.15 ± 0.35	-3.38 ± 0.14	59.7 ± 6.2	4.0 ± 1.1	0.3 ± 0.5	0.8 ± 0.5	...
1981 Mar 23 ...	06:55:37	82	N10W52	M8.5/2N	55	1.33 ± 0.12	-2.97 ± 0.22	16.6 ± 2.4
1981 Apr 1 ...	01:33:04	1376	S43W52	X2.3/3B	58	1.94 ± 0.07	-2.96 ± 0.06	408.5 ± 19.1	25.1 ± 4.1	8.0 ± 1.7	17.7 ± 1.5	1
1981 Apr 2 ...	11:04:53	...	S43W63	X2.2/1N	66
1981 Apr 10 ...	16:46:30	524	N07W36	X2.3/2B	38	3.83 ± 0.13	-3.33 ± 0.07	258.3 ± 11.4	24.9 ± 2.7	4.7 ± 1.4	16.1 ± 1.1	1
1981 Apr 14 ...	23:39:27	...	N13E73	M3.4/1N	75
1981 Apr 15 ...	06:43:15	...	N21W69	M1.8/1N	73
1981 Apr 18 ...	10:49:20	X1.0/-
1981 Apr 26 ...	11:44:05	556	N15W74	X1.2/2N	76	4.27 ± 0.11	-3.04 ± 0.06	349.1 ± 13.3
1981 Apr 26 ...	17:39:12	...	N14W79	/SN	81
1981 Apr 27 ...	08:03:28	1916	N16W90	X5.5/1N	91	4.25 ± 0.07	-3.03 ± 0.03	1201.3 ± 24.9	127.7 ± 5.4	9.1 ± 2.7	10.6 ± 1.9	1
1981 May 4 ...	08:38:08	213	N15E18	M9.0/1B	26	1.05 ± 0.07	-3.03 ± 0.16	32.9 ± 3.3
1981 May 13 ...	04:12:00	1344	N09E58	X1.5/3B	59	1.11 ± 0.03	-2.70 ± 0.05	260.8 ± 10.4
1981 Jul 18 ...	12:22:46	...	N07W18	C9.6/SF	18
1981 Jul 19 ...	05:33:20	393	S09E68	X2.7/2B	69	0.83 ± 0.04	-2.12 ± 0.06	84.7 ± 6.6
1981 Jul 19 ...	05:58:44	130	S28W56	X2.7/2B	63	12.43 ± 0.34	-3.18 ± 0.05	222.2 ± 7.6	5.6 ± 1.4	-0.6 ± 0.8	1.0 ± 0.6	1
1981 Jul 26 ...	08:05:41	82	S14E30	X1.0/2B	36	0.62 ± 0.11	-3.04 ± 0.44	7.5 ± 2.1
1981 Jul 26 ...	13:53:18	...	S15E29	X3.5/2B	35
1981 Jul 28 ...	20:09:37	66	S09W18	M3.4/1B	23	1.12 ± 0.12	-3.37 ± 0.33	9.4 ± 1.6
1981 Jul 31 ...	05:55:36	...	S13W41	C8.5/1N	45
1981 Aug 10 ...	06:58:52	...	S13W15	M4.8/1B	25
1981 Aug 30 ...	09:09:35	...	S12E80	M2.1/1N	82
1981 Sep 5 ...	06:59:34	...	N08E68	C5.9/SN	67
1981 Sep 6 ...	00:01:07	...	S12W66	M8.1/1N	68
1981 Sep 7 ...	05:10:40	98	N09E45	M9.5/1N	45	2.96 ± 0.36	-3.24 ± 0.21	38.9 ± 5.9	4.5 ± 1.1	0.7 ± 0.6	0.5 ± 0.5	...
1981 Sep 7 ...	22:22:51	...	N11W29	M4.2/SB	29
1981 Sep 10 ...	07:28:12	...	S11W70	C6.7/1N	72
1981 Sep 10 ...	09:38:43	...	N07E04	M8.4/2B	4
1981 Sep 15 ...	21:13:57	131	N05W82	X2.3/2N	82	1.42 ± 0.08	-2.47 ± 0.10	37.7 ± 3.4
1981 Sep 19 ...	05:51:03	...	N08E46	M2.6/1B	46

TABLE 1—Continued

Date (1)	Time UT (2)	Duration (s) (3)	Position (4)	GOES/H α Class (5)	Θ (deg) (6)	Power-Law Amplitude (7)	Power-Law Index (8)	Bremsstrahlung Fluence (9)	Narrow Nuclear Line Fluence (10)	0.511 MeV Line Fluence (11)	2.23 MeV Line Fluence (12)	Comments (13)
1981 Oct 7 ...	22:56:15	...	S13E90	X3.6/1B	91	32.97 ± 1.50	-1.98 ± 0.07	950.7 ± 83.4	5.4 ± 7.4	-0.7 ± 1.6	... 1.0 ± 0.8	1, 3
1981 Oct 14 ...	17:05:45	98	S06E86	X3.0/SB	87	0.18 ± 0.04	-1.77 ± 0.15	15.1 ± 4.2
1981 Nov 1 ...	18:12:49	...	S13E41	M1.6/1F	44	1.03 ± 0.13	-3.63 ± 0.44	11.5 ± 2.4
1981 Nov 5 ...	08:32:54	229	S10W12	M3.5/SB	18
1981 Nov 12 ...	16:00:40	98	N18W20	X1.2/1B	25
1981 Nov 22 ...	03:22:26	...	S20W74	M1.2/1B	76
1981 Dec 7 ...	14:50:40	82	S06E90	M1.9/SB	90	0.78 ± 0.10	-3.04 ± 0.33	9.4 ± 1.9
1982 Jan 2 ...	06:10:12	115	N19W88	M8.1/1B	89	1.23 ± 0.07	-2.17 ± 0.07	35.4 ± 3.0	2
1982 Jan 28 ...	07:21:24	770	N07E46	M8.8/3B	48	0.92 ± 0.08	-3.49 ± 0.19	85.6 ± 10.0	13.3 ± 2.8	1.0 ± 1.3	5.8 ± 1.2	2
1982 Feb 3 ...	01:14:31	557	S15W29	X1.1/2B	30	2.24 ± 0.16	-2.70 ± 0.11	220.0 ± 21.5	4.7 ± 2.8	4.5 ± 1.7	6.8 ± 1.4	2
1982 Feb 5 ...	09:05:10	212	S14W44	M4.7/1B	44	1.01 ± 0.06	-3.09 ± 0.15	30.7 ± 2.9
1982 Feb 8 ...	12:49:17	426	S13W88	X1.4/1B	87	11.32 ± 0.20	-2.78 ± 0.03	810.8 ± 19.1	16.3 ± 3.1	4.0 ± 1.8	2.1 ± 1.2	2, 3
1982 Feb 12 ...	21:57:07	...	S12W22	M4.6/SB	22
1982 Mar 26 ...	05:48:05	180	S20E71	M2.2/SB	70	0.42 ± 0.06	-2.87 ± 0.35	12.2 ± 3.0
1982 Mar 30 ...	05:36:25	393	N13W11	X2.8/3B	23	1.85 ± 0.14	-3.65 ± 0.18	82.2 ± 8.2	0.1 ± 2.1	2.2 ± 1.0	2.7 ± 1.0	1
1982 Apr 2 ...	09:07:17	81	N09W62	M6.7/2B	64	3.73 ± 0.10	-2.47 ± 0.05	61.1 ± 2.6
1982 Apr 16 ...	21:25:00	...	S04W90	M2.0/SN	90
1982 Jun 3 ...	11:42:44	1195	S09E72	X8.0/2B	72	5.06 ± 0.12	-2.76 ± 0.04	1026.9 ± 320	56.1 ± 53	86.8 ± 27	2036 ± 30	1, 3, 4, 5
1982 Jun 4 ...	19:17:24	48	S10E53	M2.9/2B	54	1.24 ± 0.11	-2.82 ± 0.20	9.8 ± 1.4
1982 Jun 5 ...	01:28:47	...	S09E48	M6.2/1B	49
1982 Jun 5 ...	06:15:30	65	S10E40	X1.1/SB	41	0.91 ± 0.12	-2.86 ± 0.33	9.5 ± 2.1
1982 Jun 6 ...	16:39:00	65	S09E25	X12.0/3B	27	0.30 ± 0.07	-1.72 ± 0.21	7.3 ± 3.1	2
1982 Jun 15 ...	00:30:15	82	S12W90	M5.4/1B	90	3.68 ± 0.16	-2.17 ± 0.06	76.0 ± 5.3	3
1982 Jun 15 ...	10:19:23	147	N13E47	X3.0/3B	48	0.82 ± 0.05	-2.08 ± 0.07	32.3 ± 2.9
1982 Jun 15 ...	15:11:34	295	S22E66	X1.3/2B	68	9.00 ± 0.21	-2.80 ± 0.03	442.5 ± 13.3	7.9 ± 1.9	3.4 ± 0.9	4.6 ± 0.8	...
1982 Jun 20 ...	01:13:22	...	N11W26	M1.0/SB	28
1982 Jun 25 ...	21:33:30	98	N17W61	M7.5/1B	62	0.72 ± 0.08	-2.63 ± 0.24	12.9 ± 2.5
1982 Jun 26 ...	00:48:00	179	N16W65	X1.9/2B	65	0.50 ± 0.08	-3.03 ± 0.43	13.2 ± 3.5
1982 Jul 9 ...	07:35:26	327	N17E73	X9.8/3B	73	23.03 ± 0.28	-2.96 ± 0.02	1150.6 ± 18.1	33.4 ± 2.9	11.5 ± 1.9	21.9 ± 1.2	1, 3
1982 Jul 9 ...	21:06:10	262	N18E79	M8.3/2B	78	6.26 ± 0.19	-2.83 ± 0.05	267.7 ± 10.8	6.8 ± 1.8	2.8 ± 0.7	4.7 ± 0.7	3
1982 Jul 9 ...	22:50:45	...	N09E69	M1.9/SB	69
1982 Jul 10 ...	02:00:00	...	N18E68	M1.7/1B	68
1982 Jul 10 ...	03:16:43	49	N16E69	M1.2/SB	69	1.29 ± 0.12	-2.70 ± 0.19	11.1 ± 1.6
1982 Jul 10 ...	04:08:20	65	N16E69	M1.1/1B	69	0.55 ± 0.10	-2.66 ± 0.37	6.4 ± 1.8
1982 Jul 10 ...	08:30:44	131	N16E64	M2.4/1F	64	2.19 ± 0.18	-3.16 ± 0.15	39.7 ± 4.2	3.4 ± 1.2	0.4 ± 0.5	0.7 ± 0.4	...

TABLE 1—Continued

Date (1)	Time UT (2)	Duration (s) (3)	Position (4)	GOES/H α Class (5)	Θ (deg) (6)	Power-Law Amplitude (7)	Power-Law Index (8)	Bremsstrahlung Fluence (9)	Narrow Nuclear			0.511 MeV Line Fluence (11)	2.23 MeV Line Fluence (12)	Comments (13)	
									Line Fluence (10)	Line Fluence (11)	Line Fluence (12)				
1982 Jul 11 ...	06:36:53	...	N15E53	C9.9/1N	53	
1982 Jul 17 ...	02:03:00	...	N11W34	M8.5/1B	34	
1982 Jul 19 ...	01:00:21	81	N20W45	X1.2/2B	46	3.03 ± 0.13	-2.92 ± 0.10	38.2 ± 2.6	
1982 Jul 20 ...	04:17:15	48	N22W59	M3.9/SN	60	2.99 ± 0.11	-2.77 ± 0.07	24.2 ± 1.3	
1982 Jul 20 ...	21:54:00	...	N20W69	M2.1/1B	69	
1982 Jul 21 ...	18:22:41	49	N23W88	M3.4/SN	86	1.87 ± 0.12	-2.64 ± 0.13	16.6 ± 1.7	
1982 Jul 22 ...	05:12:19	49	N22W90	M2.0/1N	88	2.73 ± 0.12	-2.34 ± 0.07	29.6 ± 2.1	
1982 Aug 8 ...	02:03:56	98	S09W65	M7.2/1B	67	4.13 ± 0.11	-2.52 ± 0.05	79.6 ± 3.6	
1982 Nov 22 ...	12:23:12	16	S10W33	M2.0/SB	35	3.31 ± 0.28	-3.14 ± 0.21	7.4 ± 1.0	
1982 Nov 23 ...	13:45:40	...	N10W45	M1.2/3N	46	
1982 Nov 25 ...	04:14:03	16	S10W75	M2.4/1B	76	2.65 ± 0.25	-3.31 ± 0.26	5.5 ± 0.8	
1982 Nov 26 ...	02:29:04	393	S11W87	X4.5/2B	87	9.45 ± 0.18	-3.09 ± 0.03	533.4 ± 12.8	15.0 ± 2.3	1.1 ± 1.2	1.5 ± 0.8	1	
1982 Dec 7 ...	23:40:00	2703	S19W79	X2.8/1B	80	16.45 ± 0.10	-2.91 ± 0.01	6967.8 ± 52.3	178.2 ± 7.8	23.1 ± 6.2	40.4 ± 2.8	1,4	
1982 Dec 8 ...	14:36:36	327	N07E68	M6.7/2B	68	1.26 ± 0.06	-3.03 ± 0.12	60.5 ± 4.5	
1982 Dec 13 ...	03:24:32	262	S09E51	M8.3/2B	51	1.65 ± 0.05	-2.42 ± 0.05	90.5 ± 4.3	
1982 Dec 15 ...	16:30:44	360	S10E15	X5.0/2B	17	3.79 ± 0.13	-3.83 ± 0.08	144.3 ± 6.3	6.9 ± 1.8	2.7 ± 0.8	13.3 ± 0.8	
1982 Dec 17 ...	01:48:29	...	S10W03	M4.8/1B	9
1982 Dec 17 ...	18:56:44	246	S08W21	X10.1/3B	22	2.56 ± 0.15	-3.18 ± 0.10	86.9 ± 6.5	7.7 ± 1.7	4.7 ± 0.8	22.0 ± 0.8	2	
1982 Dec 18 ...	08:21:43	...	S10W20	X1.1/2B	22
1982 Dec 29 ...	06:44:10	197	S13W12	X1.9/2B	16	6.38 ± 0.19	-4.05 ± 0.08	123.7 ± 4.8	7.8 ± 1.5	2.2 ± 0.6	4.3 ± 0.6	
1982 Dec 30 ...	01:42:35	32	S13W22	M7.1/2B	24	1.09 ± 0.18	-3.01 ± 0.41	5.2 ± 1.4	
1983 Feb 3 ...	06:03:19	1212	S19W08	X4.1/3B	15	4.38 ± 0.10	-3.21 ± 0.04	720.9 ± 22.0	1.7 ± 4.2	5.4 ± 2.4	19.5 ± 1.8	
1983 Apr 27 ...	02:54:00	...	S17E23	M1.1/1N	26
1983 Apr 28 ...	10:49:00	...	S03E24	M1.2/1B	24
1983 May 7 ...	22:16:36	...	S29E66	X3.1/2B	67
1983 May 9 ...	23:04:17	409	S29E41	X2.4/2B	47	3.02 ± 0.18	-2.95 ± 0.09	189.4 ± 14.6	6.2 ± 2.5	0.9 ± 0.8	2.6 ± 1.0	
1983 May 25 ...	09:52:00	...	M2.2/-
1983 Jun 9 ...	21:58:00	...	S08E23	M1.8/SB	24
1983 Jun 25 ...	20:50:00	65	S07E89	M4.0/SN	89	0.29 ± 0.06	-2.00 ± 0.24	5.5 ± 1.9
1983 Jun 26 ...	14:08:00	165	S13E76	M7.0/SB	77	0.64 ± 0.07	-2.98 ± 0.29	15.8 ± 3.0
1984 Apr 24 ...	23:59:42	1097	S11E45	X13.0/3B	45	3.86 ± 0.13	-2.76 ± 0.05	717.6 ± 32.7	92.1 ± 6.3	208.8 ± 3.1	355.3 ± 3.4	1, 3, 4, 5	
1984 May 5 ...	18:09:50	899	S11W91	M7.5/?	90	0.59 ± 0.02	-2.04 ± 0.04	148.1 ± 8.0
1984 May 19 ...	21:53:30	213	S07E67	X4.1/1B	67	9.52 ± 0.25	-3.19 ± 0.04	277.3 ± 9.2	10.2 ± 1.8	2.7 ± 0.90	6.6 ± 0.8	3	
1984 May 20 ...	05:40:00	...	S11E63	M5.4/1N	63
1984 May 20 ...	21:53:29	33	S08E52	C5.7/SN	52	1.38 ± 0.22	-3.43 ± 0.48	5.6 ± 1.4

TABLE 1—Continued

Date (1)	Time UT (2)	Duration (s) (3)	Position (4)	GOES/Hz Class (5)	Θ (deg) (6)	Power-Law Amplitude (7)	Power-Law Index (8)	Bremsstrahlung Fluence (9)	Narrow Nuclear Line Fluence (10)	0.511 MeV Line Fluence (11)	2.23 MeV Line Fluence (12)	Comments (13)
1984 May 21 ...	02:19:00	...	S09E52	M5.7/SN	52	0.98 ± 0.05	-2.78 ± 0.12	45.4 ± 4.0
1984 May 22 ...	14:56:57	277	S09E26	M6.3/2B	27	0.50 ± 0.07	-2.49 ± 0.27	8.0 ± 1.9
1984 Nov 10 ...	20:02:00	81	N17E06	M3.7/1B	15	3.65 ± 0.16	-3.82 ± 0.10	152.8 ± 8.4	6.4 ± 2.0	2.0 ± 1.2	7.6 ± 1.0	1
1985 Jan 21 ...	23:58:19	393	S10W40	X4.7/1N	40	2.42 ± 0.09	-2.73 ± 0.06	451.1 ± 24.3	0.3 ± 4.9	6.2 ± 2.0	10.6 ± 1.7	2
1985 Apr 24 ...	09:28:53	1081	N05E24	X1.9/2B	26
1985 Jul 2 ...	21:20:00	...	S14E57	M4.5/2B	60
1986 Feb 4 ...	07:35:36	163	S04E21	X3.0/3B	21	7.94 ± 0.23	-4.32 ± 0.09	117.0 ± 4.5	6.0 ± 1.3	1.3 ± 0.6	3.3 ± 0.5	1
1986 Feb 4 ...	10:24:13	327	S03E66	M6.4/2N	66	2.93 ± 0.07	-2.63 ± 0.05	175.7 ± 6.4
1986 Feb 6 ...	06:20:33	1228	S07W02	X1.7/2B	2	5.48 ± 0.09	-4.09 ± 0.04	653.6 ± 13.7	43.1 ± 3.8	25.3 ± 1.5	96.3 ± 2.0	...
1986 Feb 14 ...	09:10:00	...	N01W76	M6.4/1B	76
1986 Oct 19 ...	00:40:27	1294	N23W62	M4.7/2N	62	1.04 ± 0.04	-3.01 ± 0.10	199.9 ± 13.0
1988 Apr 14 ...	19:37:59	262	N25E37	X1.2/2B	47	2.98 ± 0.19	-3.38 ± 0.11	98.3 ± 7.7	5.1 ± 1.7	2.0 ± 0.9	1.3 ± 0.7	...
1988 Jun 24 ...	16:43:12	409	S17W57	X2.4/2B	55	2.03 ± 0.05	-2.65 ± 0.05	150.2 ± 6.2
1988 Jul 8 ...	12:02:12	114	N13W80	M4.4/1B	79	0.37 ± 0.09	-2.52 ± 0.52	8.3 ± 3.6
1988 Jul 18 ...	16:25:46	48	S20W15	C4.6/1F	29	0.43 ± 0.17	-3.36 ± 1.19	2.6 ± 1.7
1988 Sep 19 ...	11:01:52	147	N29E77	M1.6/1N	75	0.49 ± 0.07	-2.77 ± 0.31	12.1 ± 2.7
1988 Sep 25 ...	00:33:34	229	S17E67	M2.3/2N	70	2.36 ± 0.06	-2.62 ± 0.05	100.0 ± 4.0
1988 Sep 27 ...	16:12:05	376	S28E66	M7.9/2B	72	1.18 ± 0.05	-2.63 ± 0.09	81.3 ± 5.6	1
1988 Oct 3 ...	15:11:34	82	S27W16	X3.2/2B	37	8.41 ± 0.44	-3.25 ± 0.10	92.0 ± 6.3	3.6 ± 1.6	0.7 ± 0.8	3.2 ± 1.0	2
1988 Oct 13 ...	20:28:56	212	S20W88	M6.4/SN	89	2.56 ± 0.16	-2.77 ± 0.10	91.9 ± 7.9	2.1 ± 1.3	0.5 ± 0.6	0.3 ± 0.5	...
1988 Nov 1 ...	10:58:10	32	N11E82	M3.4/1N	81	0.97 ± 0.14	-2.45 ± 0.25	6.4 ± 1.5	1
1988 Nov 6 ...	18:21:35	180	S20W39	M4.9/2B	45	0.84 ± 0.06	-2.39 ± 0.13	32.3 ± 3.8
1988 Nov 13 ...	05:36:02	65	N34E35	M7.0/1N	45	1.00 ± 0.11	-2.74 ± 0.24	11.2 ± 2.0
1988 Nov 13 ...	23:05:02	245	S24W27	M3.2/1B	38	0.59 ± 0.05	-2.67 ± 0.18	26.1 ± 3.7	1
1988 Nov 16 ...	04:09:24	65	N33W13	M4.7/1B	33	0.50 ± 0.08	-2.64 ± 0.35	5.9 ± 1.6
1988 Dec 10 ...	23:02:32	114	S34E73	M1.8/SF	76	1.08 ± 0.07	-2.66 ± 0.14	22.2 ± 2.4
1988 Dec 13 ...	10:27:33	49	N20W40	C7.6/1B	44	1.21 ± 0.08	-2.28 ± 0.11	13.7 ± 1.5
1988 Dec 14 ...	10:12:00	...	N31E59	C6.3/SN	64
1988 Dec 14 ...	13:36:49	65	N30E61	M2.1/1N	66	1.49 ± 0.11	-2.60 ± 0.14	18.2 ± 2.1
1988 Dec 15 ...	05:03:00	...	N27E58	X1.1/2B	62
1988 Dec 16 ...	08:28:50	3555	N27E33	X4.7/2B	43	7.24 ± 0.09	-3.39 ± 0.02	3226.9 ± 51.7	337.7 ± 13.1	168.2 ± 4.4	606.7 ± 6.9	1, 2, 3, 4
1988 Dec 20 ...	12:26:12	1458	M7.3/-	2.47 ± 0.07	-2.26 ± 0.04	845.9 ± 37.0	2.9 ± 4.2	3.0 ± 2.2	4.9 ± 1.5	1, 2
1988 Dec 28 ...	23:42:36	98	N20W54	M3.6/1B	58	4.81 ± 0.10	-2.48 ± 0.03	94.7 ± 2.9
1989 Jan 10 ...	20:24:36	377	S31E30	X1.4/1B	39	2.05 ± 0.16	-3.25 ± 0.13	102.8 ± 10.2	2.4 ± 1.0	4.0 ± 0.9
1989 Jan 15 ...	15:49:43	98	S31W34	M4.5/1N	41	0.76 ± 0.10	-2.72 ± 0.28	12.8 ± 2.8	2

TABLE 1—Continued

Date (1)	Time UT (2)	Duration (s) (3)	Position (4)	GOES/H α Class (5)	Θ (deg) (6)	Power-Law Amplitude (7)	Power-Law Index (8)	Bremsstrahlung Fluence (9)	Narrow Nuclear Line Fluence (10)	0.511 MeV Line Fluence (11)	2.23 MeV Line Fluence (12)	Comments (13)
1989 Jan 16 ...	22:16:32	49	S30W51	M7.2/1B	54	0.52 ± 0.13	-3.41 ± 0.76	3.2 ± 1.3
1989 Jan 26 ...	14:11:00	...	N16W01	M1.2/SN	22
1989 Jan 26 ...	23:30:23	98	S22E73	M3.2/1N	72	0.45 ± 0.05	-2.23 ± 0.19	10.6 ± 2.1
1989 Feb 8 ...	09:45:38	81	N34E41	M1.1/1B	56	0.25 ± 0.11	-2.62 ± 0.87	3.7 ± 2.7
1989 Feb 9 ...	12:59:48	196	N21E39	X3.9/2B	47	0.89 ± 0.22	-2.77 ± 0.37	29.6 ± 9.7	4.0 ± 1.8	1.7 ± 0.7	6.2 ± 0.7	2
1989 Mar 6 ...	14:04:51	3515	N33E71	X15/3B	76	17.60 ± 0.11	-3.03 ± 0.01	9115.3 ± 70.3	370.7 ± 12.0	102.6 ± 8.3	173.4 ± 4.7	1, 2, 3, 4
1989 Mar 7 ...	05:57:27	48	N30E69	M2.0/1N	76	12.16 ± 0.52	-4.34 ± 0.16	52.5 ± 3.3	3
1989 Mar 7 ...	13:18:19	114	N30E65	M4.1/1B	73	7.93 ± 0.18	-2.84 ± 0.04	147.4 ± 4.9	3
1989 Mar 7 ...	13:43:00	...	N30E65	M2.4/1B	73
1989 Mar 7 ...	14:51:58	229	N31E65	X1.8/2B	73	1.54 ± 0.08	-3.42 ± 0.15	43.8 ± 3.6
1989 Mar 7 ...	16:53:00	...	N32E74	M3.8/1F	81
1989 Mar 7 ...	21:04:59	49	4.51 ± 0.10	-2.42 ± 0.03	46.1 ± 1.6
1989 Mar 8 ...	14:46:48	65	N28E48	M1.2/2B	58	0.71 ± 0.08	-2.60 ± 0.21	8.7 ± 1.5
1989 Mar 8 ...	18:52:01	278	...	M4.6/-	...	0.46 ± 0.05	-3.07 ± 0.28	18.4 ± 3.2
1989 Mar 10 ...	19:03:40	3341	N32E22	X4.5/3B	44	5.05 ± 0.05	-3.20 ± 0.02	2294.4 ± 31.2	90.1 ± 6.9	28.8 ± 3.9	76.1 ± 2.7	2, 3, 6
1989 Mar 11 ...	15:36:00	...	N29E12	X1.2/2B	38
1989 Mar 12 ...	08:39:00	...	N29E05	M6.7/1N	37
1989 Mar 13 ...	03:16:43	65	N29W02	X1.2/3N	36	0.30 ± 0.05	-1.50 ± 0.11	94.4 ± 3.4
1989 Mar 15 ...	06:47:09	83	N35W33	M4.8/2N	52	0.68 ± 0.06	-2.36 ± 0.14	12.3 ± 1.7
1989 Mar 16 ...	15:23:41	360	N36W47	X3.6/2B	62	6.77 ± 0.18	-2.67 ± 0.04	435.4 ± 15.9	10.9 ± 2.5	7.0 ± 1.4	30.8 ± 1.2	3, 5
1989 Mar 17 ...	03:31:16	49	N32W59	M2.5/1B	68	1.15 ± 0.13	-2.99 ± 0.30	8.5 ± 1.6
1989 Mar 17 ...	07:16:08	66	N34W61	M6.8/2B	71	3.38 ± 0.11	-2.30 ± 0.05	51.0 ± 2.5
1989 Mar 17 ...	17:31:22	835	N33W61	X6.5/2B	70	10.86 ± 0.19	-2.90 ± 0.03	1426.7 ± 32.0	45.7 ± 5.5	15.3 ± 2.0	37.4 ± 2.2	3
1989 Mar 18 ...	12:42:00	...	N36W75	C9.2/1F	82
1989 Mar 18 ...	21:56:00	...	M3.1/-
1989 Mar 23 ...	19:35:59	787	N18W28	X1.5/3B	37	1.15 ± 0.04	-3.07 ± 0.09	130.5 ± 7.2
1989 Mar 24 ...	20:27:00	...	N14W43	M1.2/2B	48	31.1 ± 3.5	6.2 ± 1.6	21.1 ± 1.4	...
1989 May 3 ...	03:42:48	1376	N28E32	X2.3/3B	44	2.10 ± 0.06	-3.31 ± 0.05	375.3 ± 14.0
1989 May 4 ...	08:18:46	65	S19W31	M2.8/SN	34	1.44 ± 0.14	-3.85 ± 0.35	9.9 ± 1.6
1989 May 4 ...	09:55:58	65	S16W31	C5.9/SB	33	1.01 ± 0.11	-2.72 ± 0.23	11.4 ± 2.0
1989 May 4 ...	11:13:15	147	S20W33	M5.4/2N	36	1.15 ± 0.07	-2.88 ± 0.13	26.8 ± 2.4	3.3 ± 1.0	7.4 ± 1.1
1989 May 5 ...	07:28:16	605	N30E04	X2.4/3B	34	2.23 ± 0.11	-3.24 ± 0.09	181.2 ± 11.1
1989 May 6 ...	17:01:02	164	S30E61	M4.2/2B	63	2.04 ± 0.06	-2.56 ± 0.06	64.1 ± 3.2
1989 Jun 2 ...	10:14:00	65	S18E60	M1.5/2B	61	2.55 ± 0.40	-3.76 ± 0.31	18.0 ± 3.5	4.3 ± 0.9	0.1 ± 0.3	0.3 ± 0.3	...
1989 Jun 2 ...	16:01:28	229	S21E59	X1.3/1B	61	0.81 ± 0.04	-2.62 ± 0.10	34.4 ± 2.9

TABLE 1—Continued

Date (1)	Time UT (2)	Duration (s) (3)	Position (4)	GOES/H α Class (5)	Θ (deg) (6)	Power-Law Amplitude (7)	Power-Law Index (8)	Bremsstrahlung Fluence (9)	Narrow Nuclear Line Fluence (10)	0.511 MeV Line Fluence (11)	2.23 MeV Line Fluence (12)	Comments (13)
1989 Jun 3 ...	03:09:00	...	S19E47	M2.1/2N	50
1989 Jun 3 ...	12:17:35	16	S21E78	M2.5/1N	79	0.83 ± 0.16	-2.90 ± 0.46	2.1 ± 0.7
1989 Jun 3 ...	18:29:13	115	S22E77	X1.0/1N	78	1.15 ± 0.06	-2.34 ± 0.08	29.2 ± 2.4
1989 Jun 4 ...	21:16:54	65	S21E69	M6.0/2N	70	0.40 ± 0.09	-2.82 ± 0.49	4.3 ± 1.5	1
1989 Jun 5 ...	21:35:13	147	S21E52	X1.0/2B	55	1.29 ± 0.06	-2.77 ± 0.09	32.1 ± 2.2
1989 Jun 8 ...	08:14:06	65	...	C6.4/-	...	0.32 ± 0.06	-2.41 ± 0.35	4.3 ± 1.4
1989 Jun 14 ...	06:06:58	48	S19E29	M1.0/SB	31	0.58 ± 0.10	-3.10 ± 0.43	4.0 ± 1.0
1989 Jun 14 ...	13:52:32	33	S14W78	M2.7/1N	79	12.93 ± 0.73	-3.06 ± 0.09	62.2 ± 4.4	2.4 ± 0.9	0.1 ± 0.4	0.5 ± 0.3	3
1989 Jun 15 ...	10:01:41	180	S17W81	M3.2/SF	82	0.40 ± 0.50	-2.66 ± 0.26	13.0 ± 2.6
1989 Jun 15 ...	19:11:46	98	S20E08	X4.1/3B	23	4.89 ± 0.34	-4.31 ± 0.18	43.3 ± 3.8	0.9 ± 1.1	0.4 ± 0.5	1.1 ± 0.4	...
1989 Jun 16 ...	07:38:29	147	S17E03	X3.0/1N	18	0.99 ± 0.08	-3.09 ± 0.21	20.9 ± 2.8
1989 Jun 20 ...	14:55:44	344	N24W70	X1.6/3N	71	0.42 ± 0.03	-2.36 ± 0.12	31.7 ± 3.7
1989 Jun 29 ...	21:10:00	409	N30W41	M3.7/1N	47	2.77 ± 0.05	-2.66 ± 0.03	204.1 ± 5.2
1989 Jun 30 ...	15:00:26	81	N20W23	M2.5/1N	28	1.79 ± 0.12	-3.26 ± 0.19	19.3 ± 2.1
1989 Jul 3 ...	01:35:29	32	S14E44	C6.8/SF	47	0.92 ± 0.21	-4.92 ± 1.14	2.2 ± 0.8
1989 Jul 4 ...	00:00:20	...	N24E54	M7.4/1B	56
1989 Jul 20 ...	20:26:59	114	S16E09	M3.3/1B	23	0.37 ± 0.05	-2.08 ± 0.19	11.4 ± 2.7
1989 Aug 6 ...	23:39:43	278	S26W24	M4.8/1N	40	1.72 ± 0.11	-3.36 ± 0.13	60.8 ± 5.2	1.8 ± 1.6	1.1 ± 0.7	0.8 ± 0.6	...
1989 Aug 7 ...	20:52:35	721	S26W38	M7.6/1N	49	3.72 ± 0.11	-3.09 ± 0.05	384.6 ± 14.3	0.1 ± 10.0	0.8 ± 1.3	3.8 ± 1.2	...
1989 Aug 12 ...	14:18:22	541	S16W38	X2.6/2B	44	0.40 ± 0.08	-2.55 ± 0.34	41.9 ± 12.9	3.1 ± 2.5	2.1 ± 1.0	4.4 ± 0.9	2
1989 Aug 14 ...	00:42:01	753	S15W60	X3.5/3B	63	2.90 ± 0.10	-2.68 ± 0.05	389.6 ± 17.6	7.4 ± 2.9	6.6 ± 0.9	8.3 ± 1.1	...
1989 Aug 15 ...	02:35:58	2980	S16W73	X1.0/1N	76	10.38 ± 0.10	-2.90 ± 0.01	4880.2 ± 59.3	26.8 ± 9.4	-10.2 ± 6.0	20.8 ± 2.7	6
1989 Aug 16 ...	01:22:56	916	S15W85	X20/2N	87	3.55 ± 0.09	-2.46 ± 0.04	661.1 ± 24.8	51.8 ± 3.8	25.4 ± 1.5	17.1 ± 1.3	2, 3
1989 Aug 17 ...	00:47:52	2228	S17W88	X2.9/SN	90	9.04 ± 0.09	-2.23 ± 0.02	4843.1 ± 80.8	22.5 ± 7.9	3.0 ± 3.3	2.2 ± 2.2	4, 6
1989 Aug 31 ...	16:18:00	...	S20E50	M1.4/1N	56
1989 Sep 1 ...	08:09:34	672	S20E65	X2.3/SB	69	1.22 ± 0.08	-2.61 ± 0.11	152.9 ± 14.6	5.3 ± 2.8	-1.3 ± 0.7	5.0 ± 1.0	...
1989 Sep 5 ...	22:22:26	32	S17E03	M5.7/1B	24	2.52 ± 0.21	-2.97 ± 0.18	12.3 ± 1.5
1989 Sep 8 ...	04:07:00	...	S19W29	M1.1/SN	39	12.5 ± 1.1	41.9 ± 1.3	3
1989 Sep 9 ...	09:09:51	541	N17E30	X1.4/1B	30	7.99 ± 0.14	-3.62 ± 0.03	493.7 ± 10.5	21.2 ± 2.6
1989 Sep 10 ...	12:56:44	262	N18E13	C9.4/1N	17	0.46 ± 0.03	-2.54 ± 0.13	23.2 ± 2.7
1989 Sep 11 ...	19:39:45	164	N19W02	M6.2/2B	12	1.88 ± 0.15	-4.21 ± 0.23	29.7 ± 3.2	3.1 ± 1.2	1.2 ± 0.5	1.5 ± 0.4	1
1989 Sep 14 ...	06:59:35	146	N16W41	M2.4/1N	41	0.27 ± 0.04	-2.59 ± 0.32	7.3 ± 1.9	1
1989 Sep 25 ...	23:41:27	278	S16E78	M3.3/1N	80	0.21 ± 0.03	-2.25 ± 0.20	13.6 ± 3.0
1989 Sep 29 ...	11:33:32	1245	S26W105	X9.8	100	4.98 ± 0.09	-2.45 ± 0.03	1272.3 ± 35.4	28.4 ± 4.4	11.9 ± 2.6	12.3 ± 1.6	1, 2, 3
1989 Oct 14 ...	17:50:00	...	N16W76	C4.8/1N	75

TABLE 1—Continued

Date (1)	Time UT (2)	Duration (s) (3)	Position (4)	GOES/H α Class (5)	Θ (deg) (6)	Power-Law Amplitude (7)	Power-Law Index (8)	Bremsstrahlung Fluence (9)	Narrow Nuclear Line Fluence (10)	0.511 MeV Line Fluence (11)	2.23 MeV Line Fluence (12)	Comments (13)
1989 Oct 19 ...	12:56:39	3260	S25E09	X13/3B	32	4.36 ± 0.08	-2.90 ± 0.03	2241.3 ± 57.4	252.6 ± 12.8	263.8 ± 3.4	705.0 ± 7.1	1, 3, 4
1989 Oct 20 ...	15:09:00	...	S28W02	M1.6/1N	33
1989 Oct 21 ...	01:53:10	...	S27W09	M2.4/2N	34
1989 Oct 24 ...	17:53:18	819	S29W57	X5.7/2N	64	14.64 ± 0.14	-3.21 ± 0.02	1628.7 ± 19.6	52.2 ± 3.7	9.2 ± 2.2	33.4 ± 1.4	1
1989 Oct 24 ...	19:15:59	441	S29W57	?/2N	64	0.39 ± 0.04	-2.71 ± 0.19	29.9 ± 4.4
1989 Oct 25 ...	16:35:47	115	S29W68	M8.7/1N	73	3.59 ± 0.26	-3.39 ± 0.14	51.8 ± 4.8	2.2 ± 1.4	1.4 ± 0.5	0.8 ± 0.5	
1989 Oct 27 ...	11:30:51	131	S33W88	M6.2/1N	91	3.94 ± 0.17	-3.29 ± 0.11	67.5 ± 4.2	
1989 Oct 27 ...	19:00:11	98	S31W81	X1.0/1F	85	1.07 ± 0.08	-2.20 ± 0.11	25.6 ± 3.2	
1989 Nov 7 ...	03:19:07	147	N19E12	M6.9/2N	19	1.79 ± 0.07	-2.62 ± 0.08	48.5 ± 3.1	
1989 Nov 9 ...	08:21:00	...	N13E52	M1.1/SN	52	
1989 Nov 12 ...	05:59:44	130	N13W39	X1.5/3B	40	2.88 ± 0.18	-2.96 ± 0.10	57.3 ± 4.7	1.3 ± 1.0	1.2 ± 0.5	0.8 ± 0.3	
1989 Nov 15 ...	19:33:15	1016	N16W27	X1.8/2B	30	5.69 ± 0.10	-3.46 ± 0.03	704.5 ± 15.0	34.3 ± 4.0	9.9 ± 2.1	38.9 ± 1.6	
1989 Nov 19 ...	06:21:18	98	S25W25	X1.1/1B	37	7.21 ± 0.30	-3.19 ± 0.07	96.9 ± 5.0	4.9 ± 1.1	1.2 ± 0.5	1.2 ± 0.4	3

Note.—Col. (1): Date of gamma-ray flare occurrence. Col. (2): Approximate Universal Time at the onset of greater than 300 keV emission. Col. (3): Duration of spectral accumulation in seconds. Col. (4): Position of the associated H α flare. Most positions were obtained from the NOAA Solar-Geophysical Data Comprehensive Reports. Col. (5): GOES X-ray class and H α properties as reported in the NOAA Solar-Geophysical Data reports. Col. (6): Heliocentric viewing angle for the flare. Derived using the method described in Vestrand et al. 1987. Col. (7): Amplitude of best power-law fit to the flare bremsstrahlung fluence. Measured at 0.3 MeV with the units photons cm $^{-2}$ s $^{-1}$ MeV $^{-(6+1)}$, where s is the index given in col. (8). Col. (8): Index for the best single-power-law fit to the flare bremsstrahlung fluence. Col. (9): Total flare bremsstrahlung fluence (photons cm $^{-2}$) measured in the 0.3–8.5 MeV energy band. Col. (10): Total narrow nuclear line fluence in photons cm $^{-2}$ derived from the best fit employing a template derived from observations of the 1981 April 27 flare (see, e.g., Share & Murphy 1995). Col. (11): Fluence (photons cm $^{-2}$) derived for positron annihilation line. Value is based on the best fit of a single Gaussian line with a width fixed at the instrumental energy resolution and centered at 511 keV. The values listed here were derived by fitting over the restricted 0.3–0.75 MeV energy band. Col. (12): Fluence (photons cm $^{-2}$) derived for the neutron capture line emission associated with deuterium formation. The value is based on the best fit of a single Gaussian line centered at 2.223 MeV that has a width fixed at the nominal energy resolution for that energy. The delayed nature of this emission means the fluence will be underestimated for events that are truncated by Earth occultation or missing data. Col. (13): (1) events that are missing late data; (2) events that are missing early data; (3) events that were detected at energies greater than 10 MeV; (4) an event where narrow nuclear line fluence is better estimated by the sum, given in Table 2, of individual line fits instead of our standard template (see Murphy & Share 1995); (5) events that are missing data due to detector saturation; (6) events that are missing data in the middle of the event.

atmosphere aspect angle during each flare. Fortunately, the orbital parameters of the *SMM* satellite produced background conditions that were very similar every 15 orbits—approximately every 24 hours. For each flare an average background spectrum was therefore constructed by averaging and live-time correcting measurements taken 15 orbits before and after the flare. Each background spectrum was checked using data accumulated for about 10 minutes prior to the flare and, if acceptable, was subtracted from the count spectrum for the flare. Occasionally this background subtraction procedure could not be employed because background data on either the preceding or the following days were missing or the flare occurred soon after passage through the SAA. Measurements shortly after an SAA passage were often problematic because the activation produced background rate enhancements that varied in a non-linear fashion from day to day. For problematic impulse flares (less than 5 minutes), we were sometimes able to employ a second technique that interpolates measurements taken just before and just after the flare to derive a flare background.

Two approaches were taken to rebinning the spectral data in order to improve the statistical precision for fitting the model components. For low-fluence flares, we rebinned the 476 logarithmically spaced channels with eight-channel accumulations to produce 60 channel spectra. Since this binning results in an energy resolution that is comparable to the actual instrumental energy resolution, we found that the eight-channel accumulations do not significantly degrade, even for intrinsically narrow lines like the 2.223 MeV line from neutron capture on hydrogen, the ability to measure line intensities accurately. For high-fluence flares, a second approach was employed that accumulates channels sequentially toward high energies until a 0.5σ significance in the flare counts is achieved for the accumulation; subsequent higher energy channel accumulations were then required to have a monotonically increasing number of channels. The two approaches were found to yield similar results for high-fluence flares where it was possible to derive parameters using both accumulation methods.

Spectral parameters for the GRFs were derived using standard “forward folding” fitting procedures. Model photon spectra were convolved with the instrument response function to predict count spectra, while the component parameters were varied to minimize the χ^2 of the fit to the background-subtracted count spectrum measured during the flare. The model photon spectra were composed of seven independent components: (1) an electron bremsstrahlung continuum represented by a single or broken power law, (2) a narrow-line resolved nuclear component based on a template derived from the 1981 April 27 flare (Murphy et al. 1990), (3) a broad-line nuclear component based on fits to the 1981 April 27 flare, (4) a broad line near 450 keV due to α - α interactions, (5) a positron annihilation line at 511 keV, (6) a three-photon positronium annihilation continuum, and (7) a narrow line at 2.223 MeV due to neutron capture on hydrogen.

A significant electron bremsstrahlung component was found in all of the flares that were intense enough to allow spectral fitting. When characterizing the properties of this bremsstrahlung component, we restricted the spectral shape to a single power law during the global seven-component fits. This single power-law model generally gave acceptable χ^2 values when fitting the observations. For a few of the

largest flares, where the statistics were quite good, improved fits could be obtained by allowing spectral curvature. By integrating the best-fitting power-law spectra we were able to determine 0.3–8.5 MeV bremsstrahlung fluence values for 185 flares. The values, listed in column (8) of Table 1, range from our detection threshold of ~ 2 photons cm^{-2} to almost 10^4 photons cm^{-2} .

The “narrow” nuclear component was fitted by a fixed template. That template was composed of 10 narrow features in the energy band from 0.8 to 8.5 MeV which are primarily generated by prompt nuclear de-excitation of solar atmosphere nuclei excited by bombardment with energetic solar flare ions. The relative amplitudes of the template feature were fixed at the values observed for the intense 1981 April 27 flare (Murphy et al. 1990). Since the properties derived for the nuclear component were sometime sensitive to the shape of the bremsstrahlung component, we also allowed broken or summed power-law models for the bremsstrahlung photon model whenever they improved the global spectral fit. There were 40 flares for which the global fit required a narrow-line nuclear component with an amplitude of greater than 3σ significance. The derived fluence values are listed in column (9) of Table 1.

For the largest flares, where the statistics allow one to study individual nuclear lines, the measured line strengths can deviate from the predictions of our best-fitting nuclear template. Therefore, for the 19 *SMM* flares that have spectra with sufficient statistical precision, we have fitted individual nuclear line features and derived spectral parameters using the techniques presented in Share & Murphy (1995). Table 2 presents the spectral parameters determined in that manner. Comparison of the derived nuclear fluences indicates that seven of the 19 flares have values that differ by more than 2σ from the template-based value presented in Table 1: 1982 June 3, 1982 December 7, 1984 April 24, 1988 December 16, 1989 March 6, 1989 August 17, and 1989 October 19. For those flares, we consider the values given Table 2 to be better estimates of the spectral parameters.

Often the strongest nuclear line in GRF spectra is the 2.223 MeV line generated by neutron capture on solar atmospheric hydrogen. All of our photon models place an unresolved neutron capture line with variable amplitude at 2.223 MeV. The amplitudes derived by our spectral fits indicated a neutron capture line with greater than 3σ significance for 48 flares. The derived fluences are listed in column (11) of Table 1. The typical capture time for energetic neutrons in the solar photosphere is ~ 100 s. For events that are missing data, identified in the notes column of Table 1, one must be careful when comparing the neutron capture line fluence with that measured for the prompt nuclear lines (see, e.g., Vestrand & Forrest 1993).

Our photon model also includes a line feature at 511 keV, which is due to direct positron annihilation, and a positronium continuum. There are 23 flares in the sample where the amplitude of the 511 keV feature in the 0.3–8.5 MeV global fits indicates detection at the greater than 3σ level of significance. We also did fits over a smaller energy range, 300–750 keV, to derive the fluence in the narrow 511 keV annihilation line. Those narrow energy band fits used an incident photon model containing a power-law bremsstrahlung component, a narrow 511 keV annihilation line, a positronium continuum, instrumentally degraded emission

TABLE 2
PARAMETERS FOR 19 LARGE FLARES FITTED WITH INDIVIDUAL NUCLEAR LINES

Date (1)	Time UT (2)	Accumulation Time (s) (3)	Power-Law Amplitude (4)	Power-Law Index (5)	Bremsstrahlung Fluence (6)	Narrow Nuclear Line Fluence (7)	2.23 MeV Line Fluence (8)	Comments (9)
1981 Apr 10	16:46:13	524	3.78 ± 0.06	-3.24 ± 0.08	265.5 ± 10.5	23.5 ± 3.1	16.1 ± 1.2	1
1981 Apr 27	08:04:01	1916	4.21 ± 0.03	-3.02 ± 0.03	1194.9 ± 21.8	113.1 ± 6.2	9.8 ± 2.1	1
1982 Jun 3	11:44:22	1195	5.13 ± 0.05	-2.67 ± 0.04	1097.9 ± 27.6	28.6 ± 6.9	204.0 ± 3.0	1
1982 Jul 9	07:35:09	327	11.09 ± 0.17	-4.34 ± 0.09	1249.0 ± 10.0	33.6 ± 3.4	22.0 ± 1.2	2
1982 Nov 26	02:29:21	393	9.56 ± 0.08	-3.15 ± 0.04	523.2 ± 10.2	16.2 ± 2.7	1.8 ± 0.9	1
1982 Dec 7	23:38:29	2703	16.68 ± 0.04	-2.92 ± 0.01	7030.8 ± 40.6	147.9 ± 8.8	41.6 ± 2.8	
1984 Apr 25	00:03:48	1097	3.36 ± 0.05	-2.77 ± 0.06	915.8 ± 24.0	55.3 ± 6.2	353.4 ± 3.5	1, 3
1986 Feb 6	06:20:19	1228	5.57 ± 0.05	-4.17 ± 0.05	646.2 ± 11.8	45.4 ± 4.5	95.7 ± 2.0	
1988 Dec 16	08:28:50	3555	7.04 ± 0.03	-3.29 ± 0.02	3283.7 ± 34.9	219.6 ± 10.7	616.6 ± 5.4	
1989 Mar 6	14:04:51	3515	17.49 ± 0.04	-2.98 ± 0.01	9310.2 ± 50.2	293.8 ± 11.6	179.9 ± 4.2	
1989 Mar 10	19:03:40	3341	5.07 ± 0.03	-3.26 ± 0.02	2251.0 ± 25.0	108.5 ± 7.5	76.0 ± 2.7	1
1989 Mar 17	17:31:22	835	11.38 ± 0.07	-3.01 ± 0.02	1416.2 ± 18.2	48.8 ± 4.6	36.0 ± 1.7	
1989 May 3	03:42:49	1376	2.10 ± 0.03	-3.30 ± 0.07	375.8 ± 12.4	24.3 ± 4.1	21.8 ± 1.5	
1989 Aug 16	01:22:56	916	3.46 ± 0.04	-2.35 ± 0.04	697.1 ± 20.4	45.9 ± 3.9	17.0 ± 1.3	1
1989 Aug 17	00:47:52	2228	8.80 ± 0.24	-2.23 ± 0.01	4689.3 ± 110.9	54.4 ± 7.3	4.1 ± 2.2	1, 4
1989 Sep 9	09:09:51	541	8.05 ± 0.07	-3.67 ± 0.04	489.1 ± 8.6	17.0 ± 2.9	42.3 ± 1.3	
1989 Oct 19	12:58:51	3260	4.16 ± 0.03	-2.75 ± 0.03	2317.5 ± 38.4	179.7 ± 10.3	703.4 ± 5.5	1
1989 Oct 24	17:56:50	8194	14.69 ± 0.07	-3.24 ± 0.02	1613.3 ± 14.3	44.7 ± 3.7	33.7 ± 1.4	1
1989 Nov 15	19:33:15	1016	5.67 ± 0.05	-3.47 ± 0.04	701.0 ± 12.9	32.6 ± 4.4	38.7 ± 1.6	

NOTE—Col. (1): Date of gamma-ray flare occurrence. Col. (2): Universal time for the beginning of the spectral accumulation. Col. (3): Duration of spectral accumulation in seconds. Col. (4): Amplitude of best power-law fit to the flare bremsstrahlung fluence. Measured at 0.3 MeV with the units photons cm⁻² s⁻¹ MeV^{-(s+1)}, where s is the index given in col. (5). Col. (5): Index for the best single-power-law fit to the flare bremsstrahlung fluence. Col. (6): Total flare bremsstrahlung fluence (photons cm⁻²) measured in the 0.3–8.5 MeV energy band. Col. (7): Total narrow nuclear line fluence in photons cm⁻² derived from the sum of the fluences from 10 nuclear line features as given in Share & Murphy 1995. Col. (8): Fluence (photons cm⁻²) derived for neutron capture line emission associated with deuterium formation. The value is based on the best fit of a single Gaussian line centered at 2.223 MeV that has a width fixed at the nominal energy resolution for that energy. The delayed nature of this emission means the the fluence will be underestimated for events that are truncated by Earth occultation or missing data. Col. (9): (1) events that are missing data; (2) an event that is best fitted by the sum of two power laws, the second of which has an amplitude of 12.40 at 300 keV and an index of -2.30; (3) an event that is also best fitted by the sum of two power laws, the second of which has an amplitude of 0.59 at 300 keV and an index of -1.57; (4) an event that is best fitted by a broken power law with break energy of 3.37 MeV and postbreak index of -4.00.

from energies above 750 keV, and a broad line near 450 keV from α - α fusion reactions. The 511 keV line fluences derived using both the broad and the narrow energy band fits were comparable. In column (10) of Table 1 we list the fluence values derived for the narrowband fits.

Our broadband fitting of both bremsstrahlung and nuclear components is the first that has been performed for the complete *SMM* sample of GRFs (cf. Murphy et al. 1990). In our earlier study of the gamma-ray bremsstrahlung from Cycle 21 flares (Vestrand et al. 1987), we restricted the fitted energy band to 300 keV–1 MeV in an effort to minimize the contribution from nuclear emission. Comparison of the derived spectral indices from that earlier study with those obtained by our current study indicates that contamination by the nuclear admixture resulted in a modest overestimate of the bremsstrahlung spectral hardness ($\Delta s \approx 0.1$) in high-fluence flares. Our subtraction of the nuclear component therefore makes the spectral indices listed in this atlas a better characterization of the gamma-ray bremsstrahlung for high-fluence flares. However, we caution the reader that the spectral indices we derive for low-fluence flares, where the nuclear component was not included in the fit because the amplitude had less than 2σ significance, are probably less reliable than our earlier narrowband fits. This decreased reliability is generated by the greater sensitivity of the broadband spectral index to

unsubtracted nuclear emission and background fluctuations. It is also worth remembering that while single-index power laws usually fit the data fairly well, examination of the atlas spectra show cases where the bremsstrahlung spectra are more complex. Therefore, the single index is probably best used as only a measure of the spectral hardness. Quantitative studies of individual bright flares are likely to warrant more complicated spectral models.

4. TIME HISTORY AND SPECTRAL PLOTS

One of the goals of this atlas is to facilitate the comparison of the properties of GRFs. Therefore, in Figures 2–23 we present time histories and spectra for all of the *SMM*/GRS flares that were intensive enough to allow spectroscopic study. The figures are arranged so that the time profiles for a given flare are presented on the left-hand page and the measured count rate spectrum along with the count rate spectrum predicted by the best-fitting model photon spectrum are presented at the same location on the facing page. An effort was also made to plot all flare time histories on the same time base. Nearly 90% of the GRFs detected by *SMM*/GRS were impulsive and produced gamma-ray emission that was only measurable for less than 900 s. However, the other 10% were so temporally extended that a single time base could not practically display the time profiles. We therefore adopted five time bases: 900, 1800, 2700, 3600, and

7200 s. The atlas is therefore divided into five subsections wherein flares with that duration are plotted in chronological order.

For compilation of the time histories onto a single plot for each flare, the measured time profiles in four selected energy bands were plotted at the native 16.384 s time resolution of the MCS. For those energy bands that were recorded with higher temporal resolution, the rates were summed to form 16.384 s accumulations. As an indication of the flare signal-to-noise ratio and the background count rates associated with each event, the background count rates have not been subtracted from the time profiles and short intervals of background measurements before and after the flare are included on the atlas plots. To clearly separate the time histories on the plots, each of the energy bands was multiplied by a scaling factor that was held constant for all of the plots presented in the atlas. The flare time history plots also note significant changes in the instrument status such as entry into the SAA region or an Earth occultation interval.

The time histories were plotted for four energy bands: 56–199 keV, 298–526 keV, 4–8 MeV, and 10–25 MeV. Those energy bands were selected because, during a flare, each is believed to have its count rate dominated by emission that samples a different characteristic of the energetic particle distributions. Counts in the lowest energy band, 56–199 keV, are primarily generated by bremsstrahlung from nonrelativistic electrons. Electrons with those energies were previously thought, in the old two-phase acceleration paradigm (e.g., Frost & Dennis 1971), to be the seed particles for the second-phase acceleration mechanism that accelerated particles to high energies. During a flare, the rate in the 298–526 keV band is usually dominated by bremsstrahlung from transrelativistic electrons. However, delayed emission from positron annihilation can make an important contribution to the 298–526 keV count rate during the fading portions of the gamma-ray emission. The flare count rate in the 4–8 MeV band is typically dominated by nuclear emission generated as energetic ions interact with ambient solar material (Ramaty & Murphy 1987). Finally, flare emission in the highest energy band, 10–25 MeV, is normally dominated by bremsstrahlung from

primary or secondary (generated via meson decay) ultrarelativistic electrons.

At the same location on the page opposite the time history, we have plotted the count rate spectrum for each flare. To facilitate adoption of a standard ordinate axis, each count rate spectrum was background subtracted and averaged over the flare duration. Adjacent channels were also summed until each data point on the plot had greater than 2σ significance. The curves drawn through the data points are the count rate spectra predicted by the best fitting of the composite photon models we described in §3.3. For those flares that display a strong nuclear component, a second curve, which falls well below the high-energy data points, denotes the predicted count rate associated with the best-fitting electron bremsstrahlung component.

5. SUMMARY

We have presented a comprehensive compilation of data for the complete sample of 258 gamma-ray flares detected by the *SMM/GRS* during a decade of nearly continuous operation. The size of the sample shows that gamma-ray emission is not, as was once believed, an unusual property that is associated only with rare, giant flares. For the 185 brightest flares in the sample, time profiles for the high-energy emission and gamma-ray spectra were presented. Spectral parameters were derived by fitting the broadband, 300 keV–10 MeV, measurements to standard spectral models for bremsstrahlung, prompt nuclear emission neutron capture line emission, and positron annihilation emission. A uniform methodology was employed throughout for deriving the GRF properties. The data will therefore be useful for studying the global properties of gamma-ray flares as well as their correlation with other aspects of flare phenomenology—subjects that will be the focus of forthcoming publications based on this atlas.

This work was supported by NASA grants NAGW-3538 and NAGW-5146 at the University of New Hampshire; DPR W-18895 at the Naval Research Laboratory; and in Germany by the Bundesministerium für Forschung und Technologie under 010K017-ZA/WS/WRK 0275:4.

REFERENCES

- Biermann, L., et al. 1951, *Z. Naturforsch.*, 6a, 47
- Bohlin, J. D., et al. 1980, *Sol. Phys.*, 65, 5
- Chupp, E. L., et al. 1973, *Nature*, 241, 333
- . 1987, *ApJ*, 318, 913
- Cliver, E. W., Forrest, D. J., Cane, H. V., Reames, D. V., McGuire, R. E., von Rosenvinge, T. T., Kane, S. R., & MacDowall, R. J. 1989, *ApJ*, 343, 953
- Forrest, D. J., & Chupp, E. L. 1983, *Nature*, 305, 291
- Forrest, D. J., et al. 1980, *Sol. Phys.*, 65, 15
- Frost, K. J., & Dennis, B. R., 1971, *ApJ*, 165, 655
- Gleske, I., & Forrest, D. J. 1980, *IEEE Trans. Nucl. Sci.*, 27, 313
- Haug, E. 1975, *Z. Naturforsch.*, 30a, 1099
- Kane, S. R., Chupp, E. L., Forrest, D. J., Share, G. H., & Rieger, E. 1986, *ApJ*, 300, 195
- Mandzhavidze, N., & Ramaty, R. 1992, *ApJ*, 396, L111
- Morrison, P. 1958, *Nuovo Cimento*, 7, 858
- Murphy, R. J., Ramaty, R., Kozlovsky, B., & Reames, D. V. 1991, *ApJ*, 371, 793
- Murphy, R. J., Share, G. H., Letaw, J. R., & Forrest, D. J. 1990, *ApJ*, 358, 298
- Okudaira, K., Hirasima, Y., Yoshimori, M., & Kondo, I. 1981, *Proc. 17th Int. Cosmic Ray Conf.*, 3, 11
- Ramaty, R., Mandzhavidze, N., Kozlovsky, B., & Murphy, R. J. 1995, *ApJ*, 455, L193
- Ramaty, R., & Murphy, R. J. 1987, *Space Sci. Rev.*, 18, 341
- Rieger, E., Reppin, C., Kanbach, G., Forrest, D. J., Chupp, E. L., & Share, G. H. 1983, *Proc. 18th Int. Cosmic Ray Conf.*, 10, 338
- Rieger, E., Vestrand, W. T., Forrest, D. J., Chupp, E. L., Kanbach, G., & Reppin, C. 1989, *Science*, 244, 441
- Ryan, J. M. 1986, *Sol. Phys.*, 105, 365
- Share, G. H., Kinzer, R. L., Kurfess, J. D., Messina, D. C., Purcell, W. R., Chupp, E. L., Forrest, D. J., & Reppin, C. 1988, *ApJ*, 326, 717
- Share, G. H., Kurfess, J. D., Marlow, K. W., & Messina, D. C. 1989, *Science*, 244, 444
- Share, G. H., & Murphy, R. J. 1995, *ApJ*, 452, 933
- . 1997, *ApJ*, 484, L165
- Vestrand, W. T., & Forrest, D. J. 1993, *ApJ*, 409, L69
- Vestrand, W. T., Forrest, D. J., Chupp, E. L., Rieger, E., & Share, G. H. 1987, *ApJ*, 322, 1010
- Yoshimori, M., Watanabe, H., & Nitta, N. 1985, *Publ. Phys. Soc. Japan*, 54, 4462
- Zirin, H. 1989, *Astrophysics of the Sun* (Cambridge: Cambridge Univ. Press)

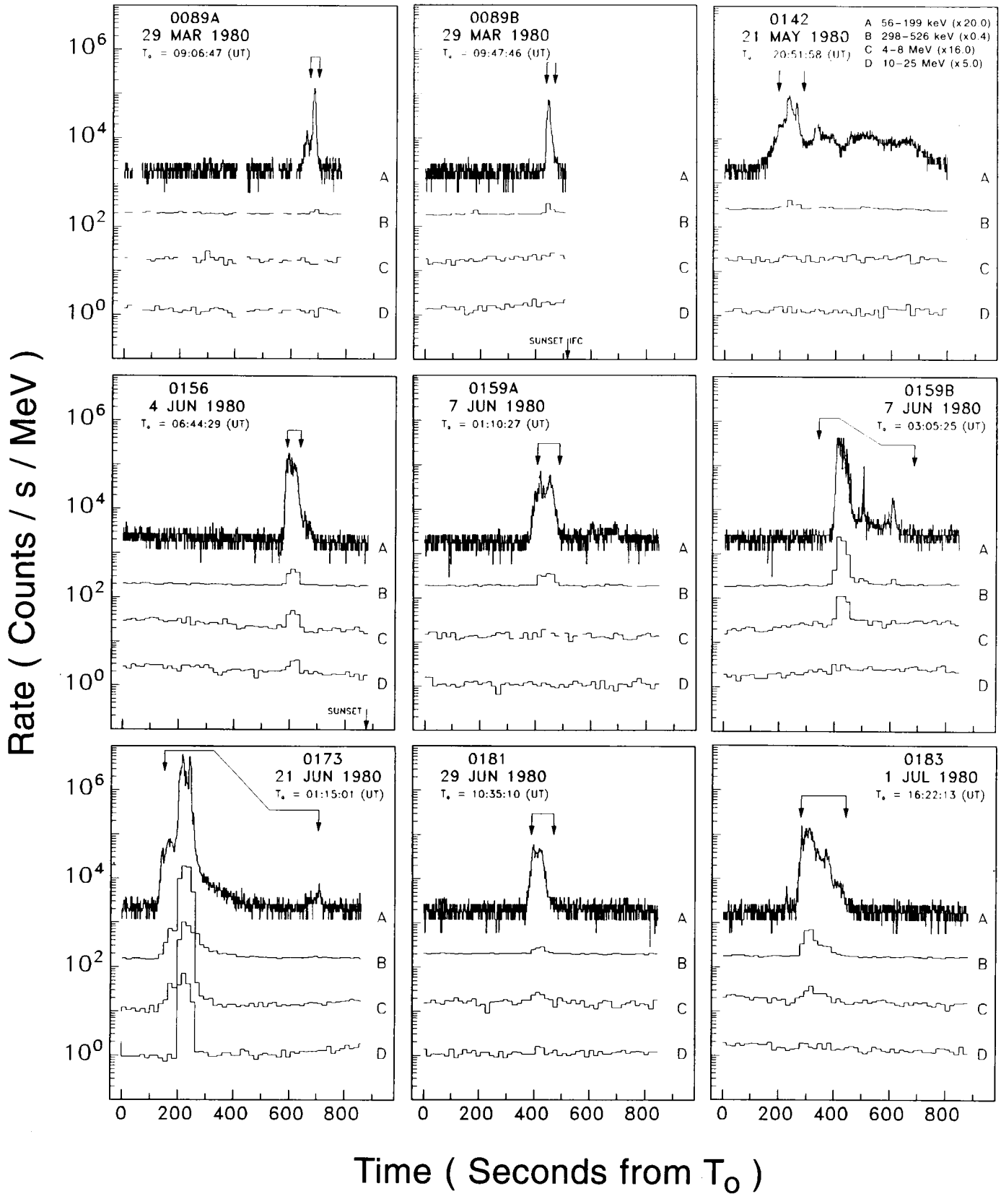


FIG. 2a

Figs. 2-23.—(a) Count rates ($\text{count s}^{-1} \text{ MeV}^{-1}$) measured by the SMM/GRS for four energy bands during time intervals that include a major gamma-ray flare. The plotted energy bands 56–199 keV, 298–526 keV, 4–8 MeV, and 10–25 MeV have been scaled by the factors 20.0, 0.4, 16.0, and 5.0, respectively, so that they fit on a single plot. The arrows denote the time interval over which the flare spectrum was accumulated for spectral study. The plotted rates have not been background subtracted, but the rates before and after the accumulation interval indicate the background count rates. (b) Background-subtracted count rate spectra for major gamma-ray flares detected by SMM/GRS. The solid line represents the count rate predicted by the best-fitted composite photon spectral model. For flares with a strong nuclear component we have also plotted a second curve which denotes the contribution from electron bremsstrahlung emission.

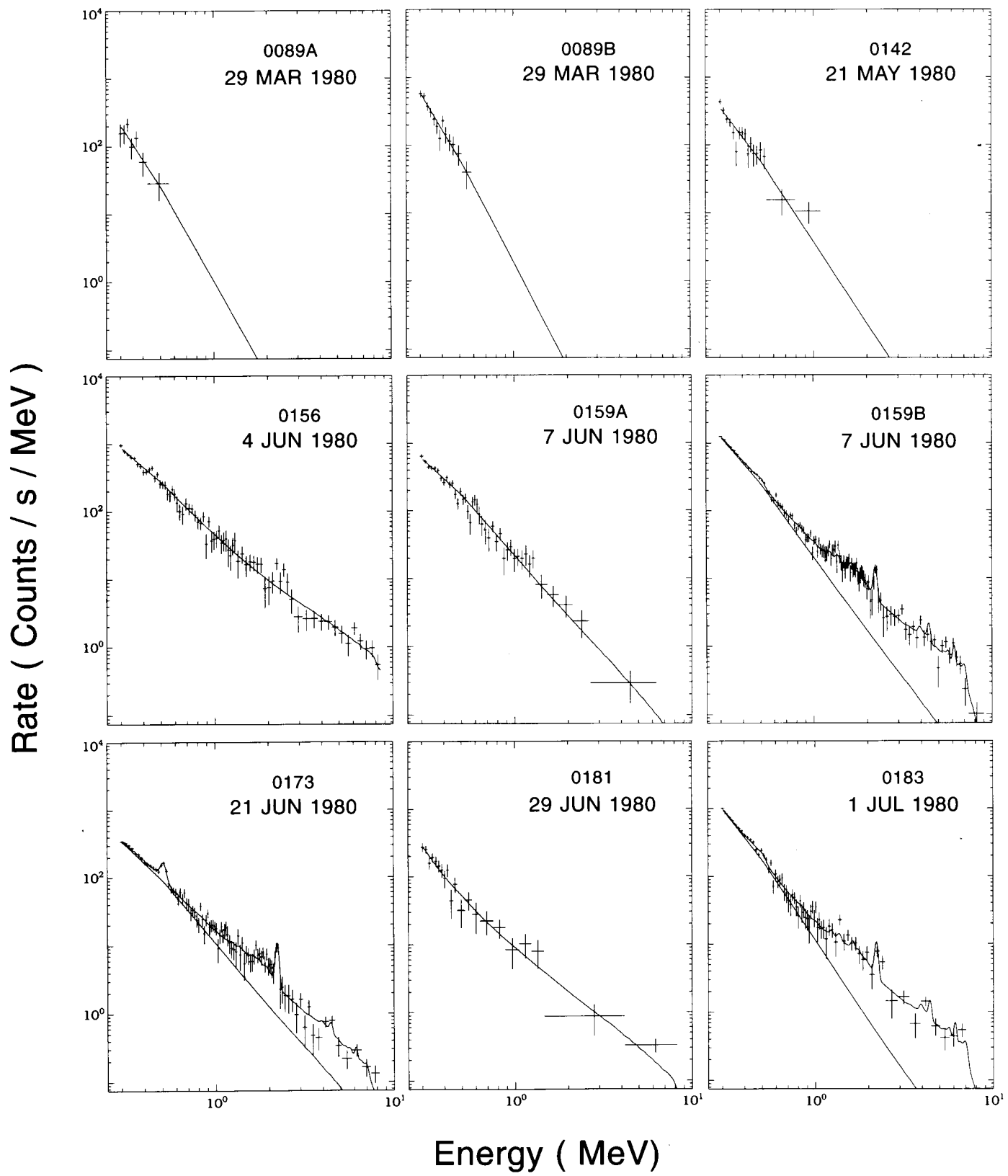


FIG. 2b

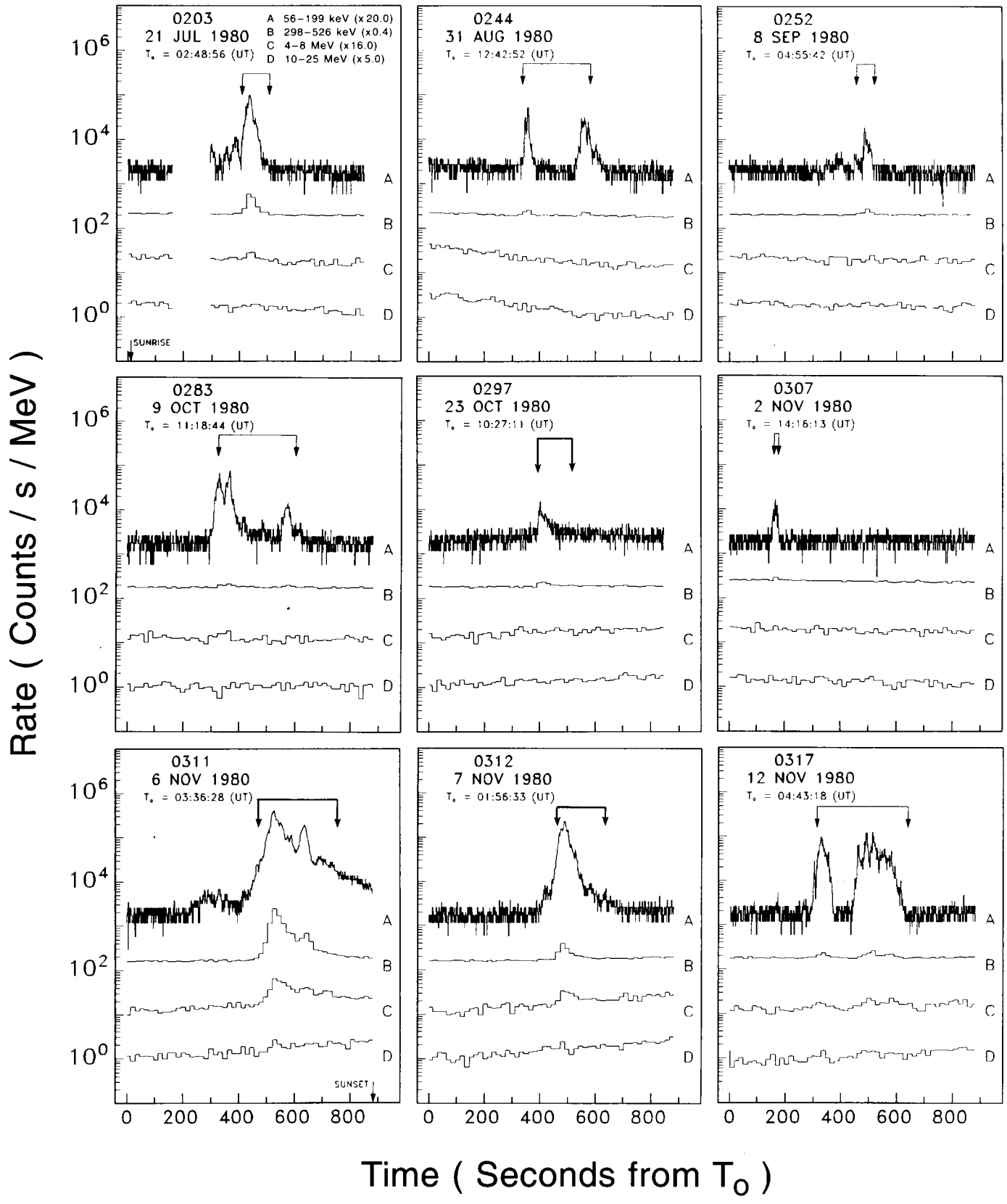


FIG. 3a

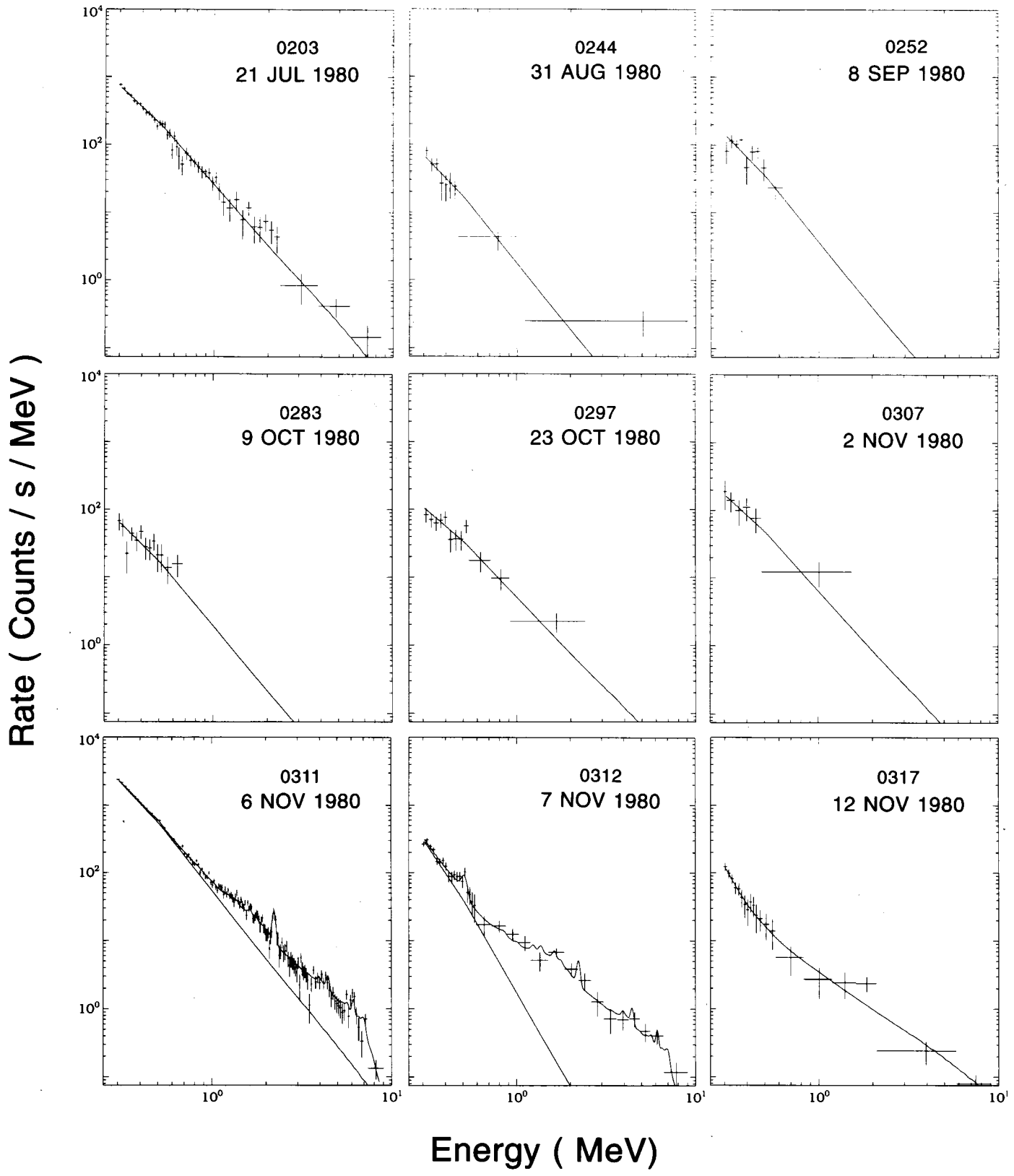


FIG. 3b

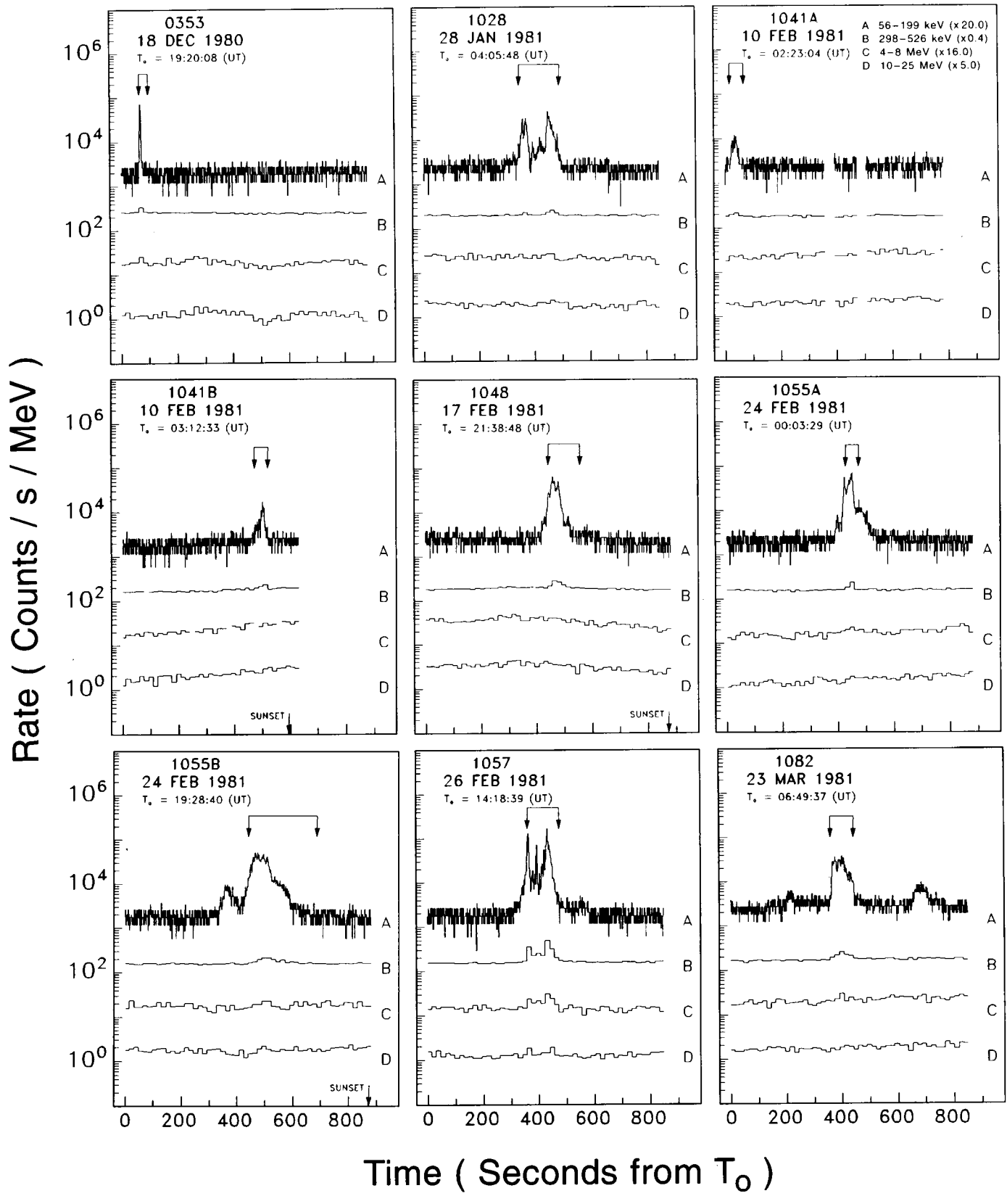


FIG. 4a

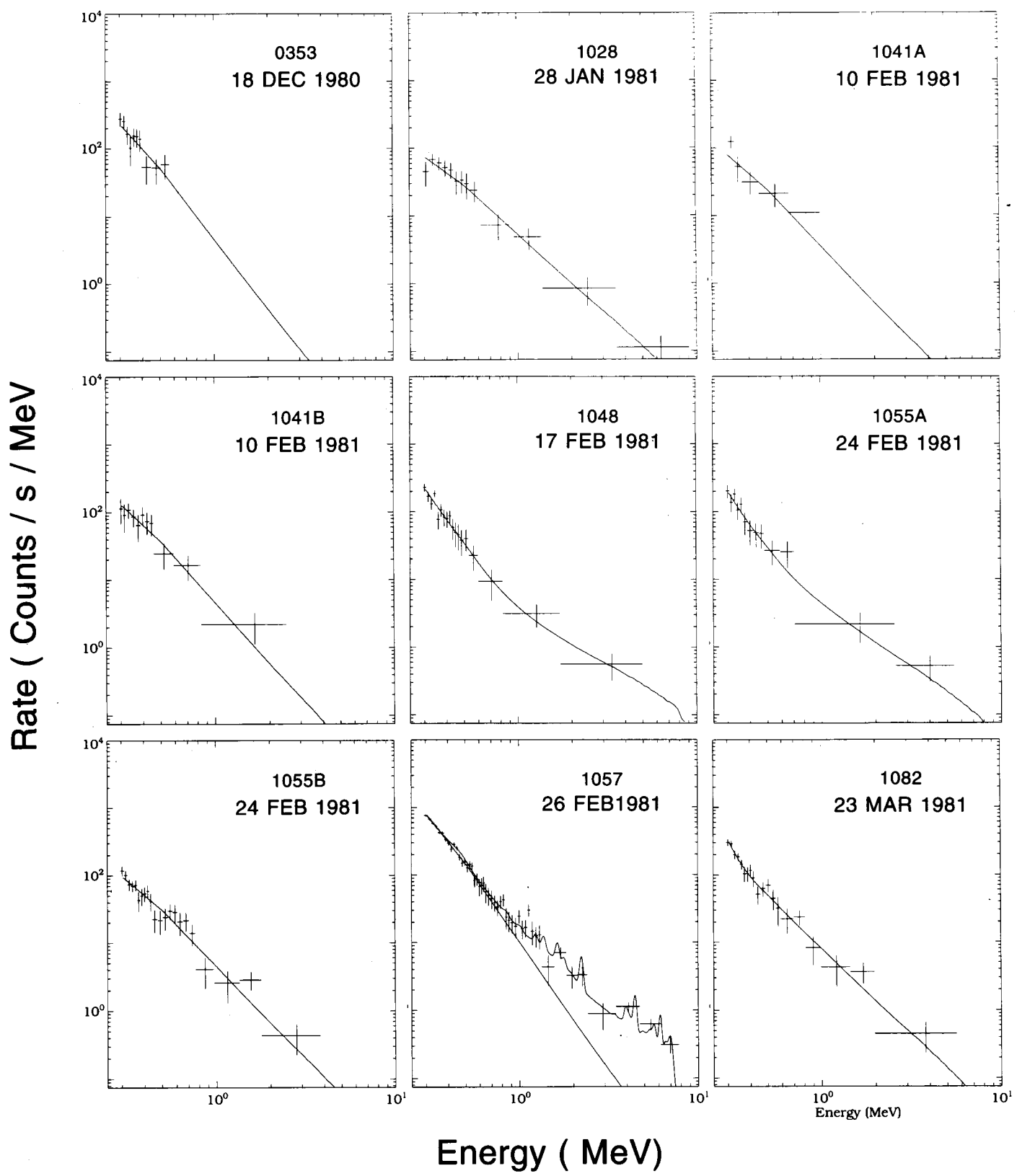


FIG. 4b

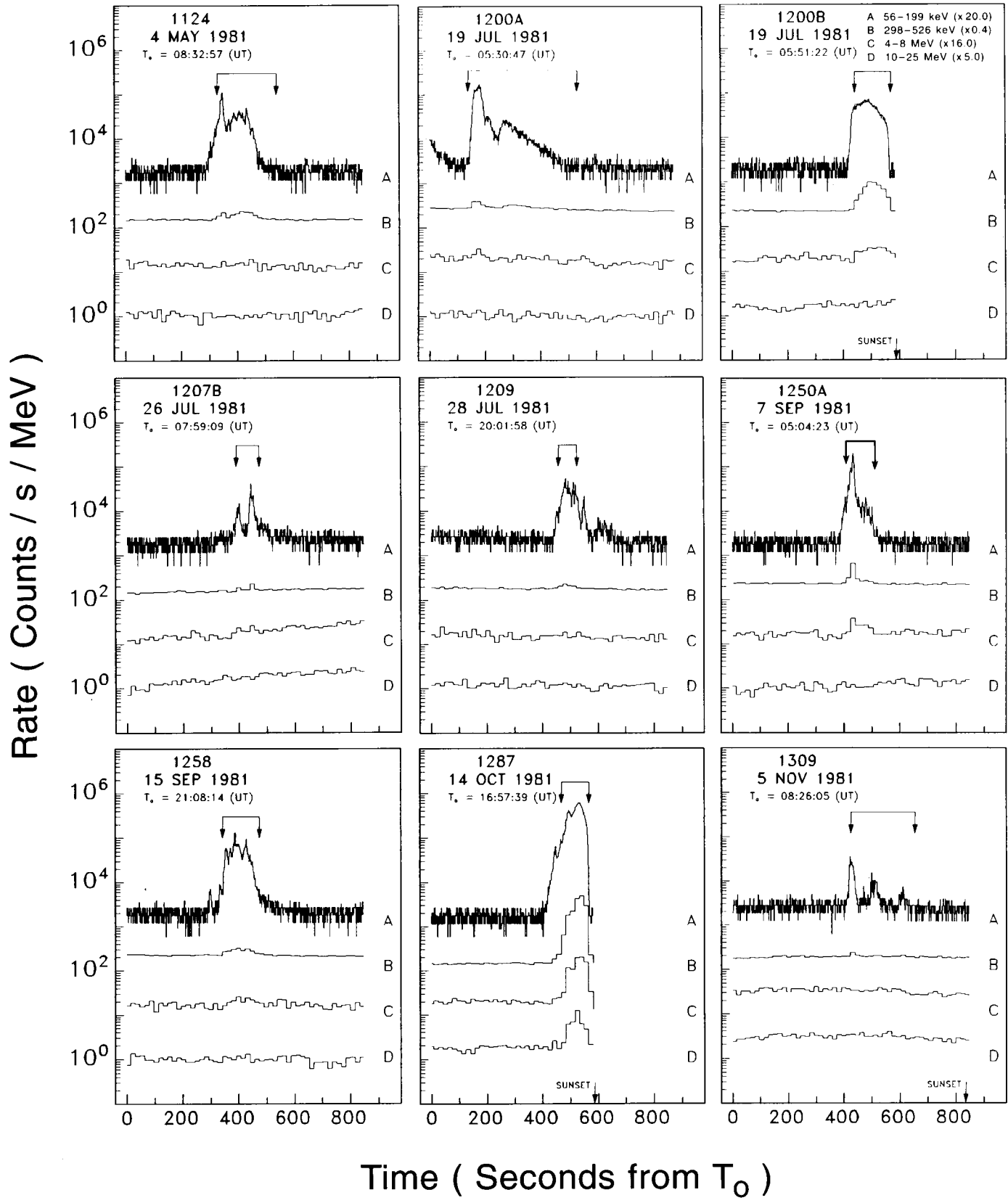


FIG. 5a

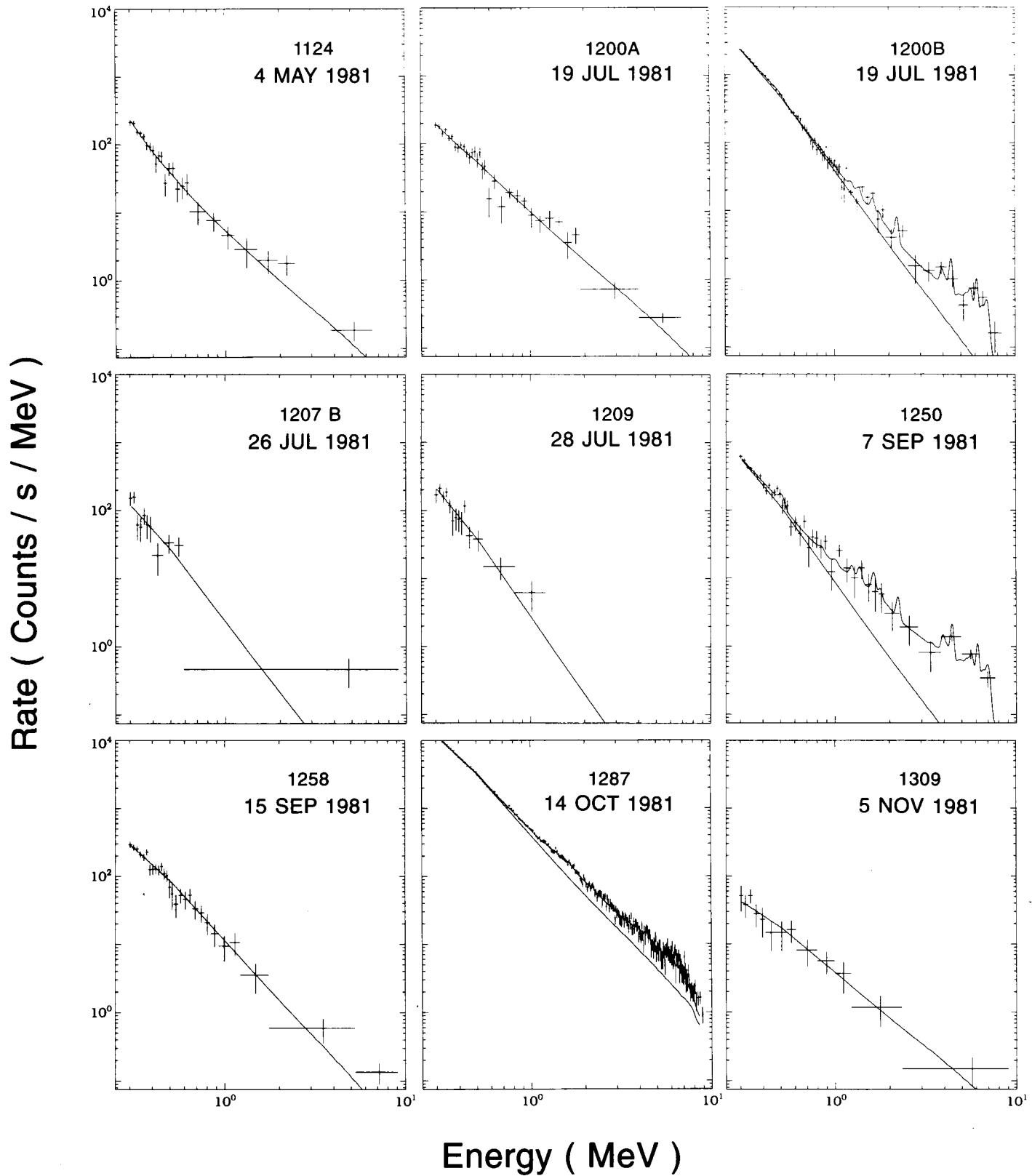


FIG. 5b

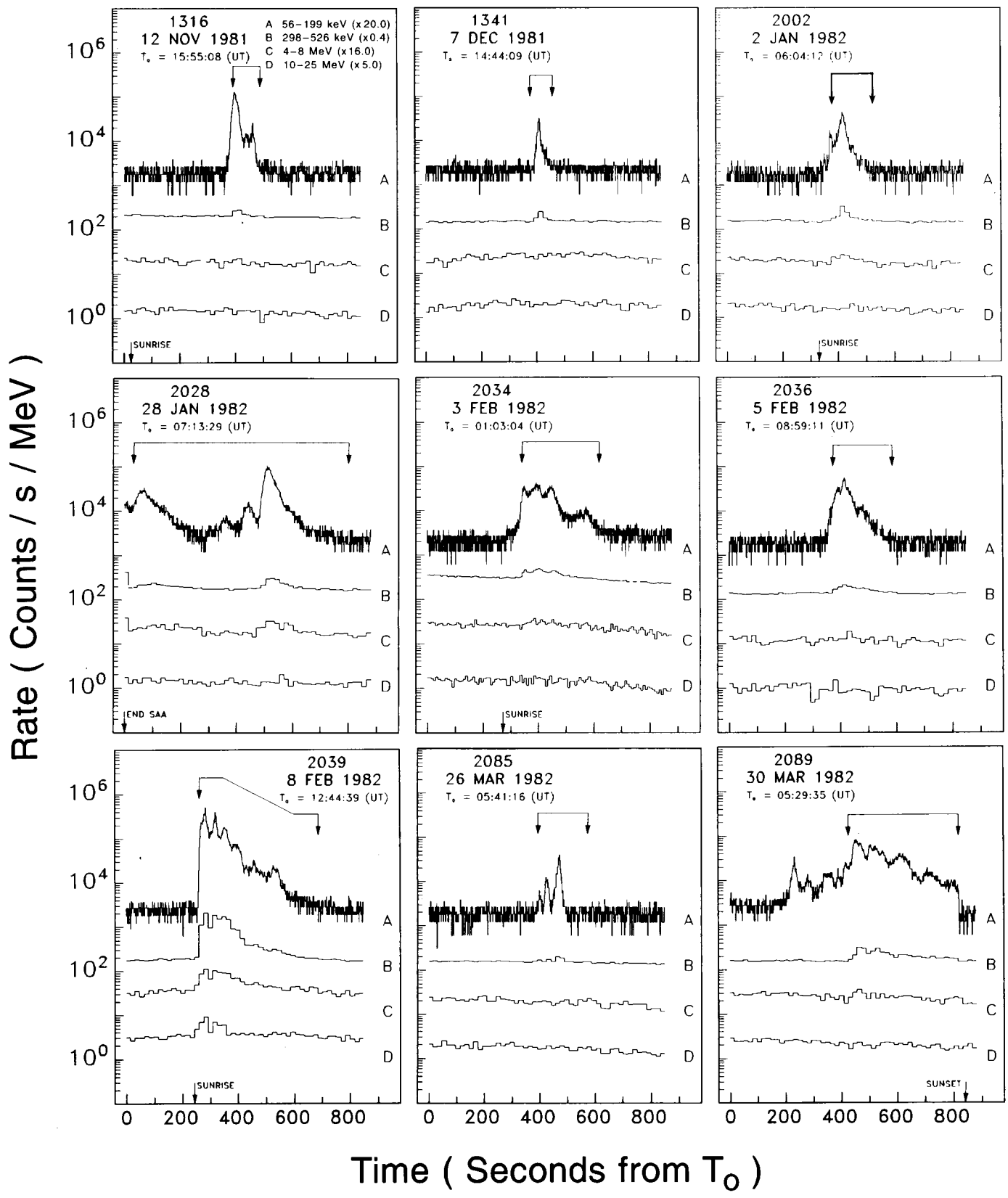


FIG. 6a

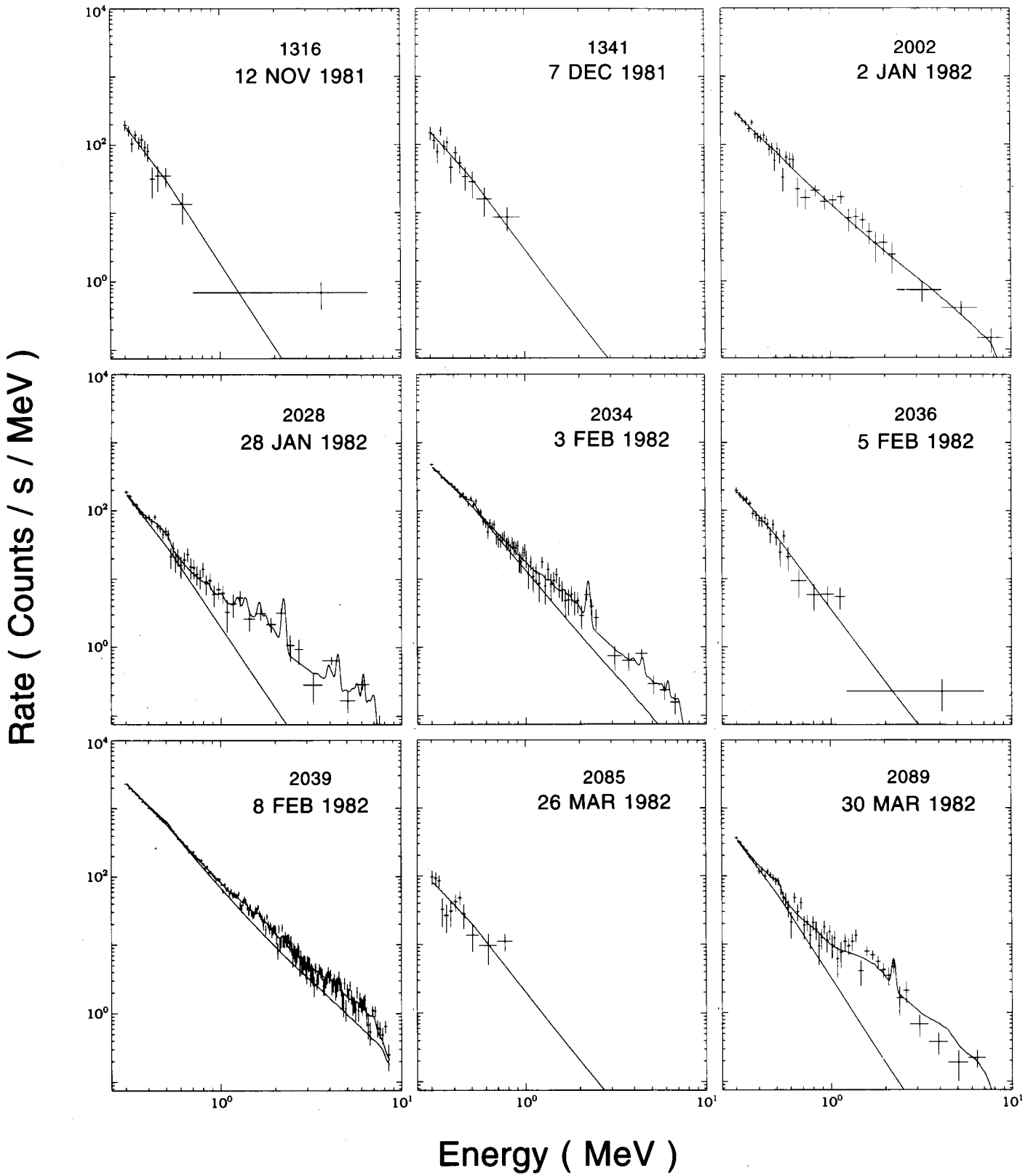


FIG. 6b

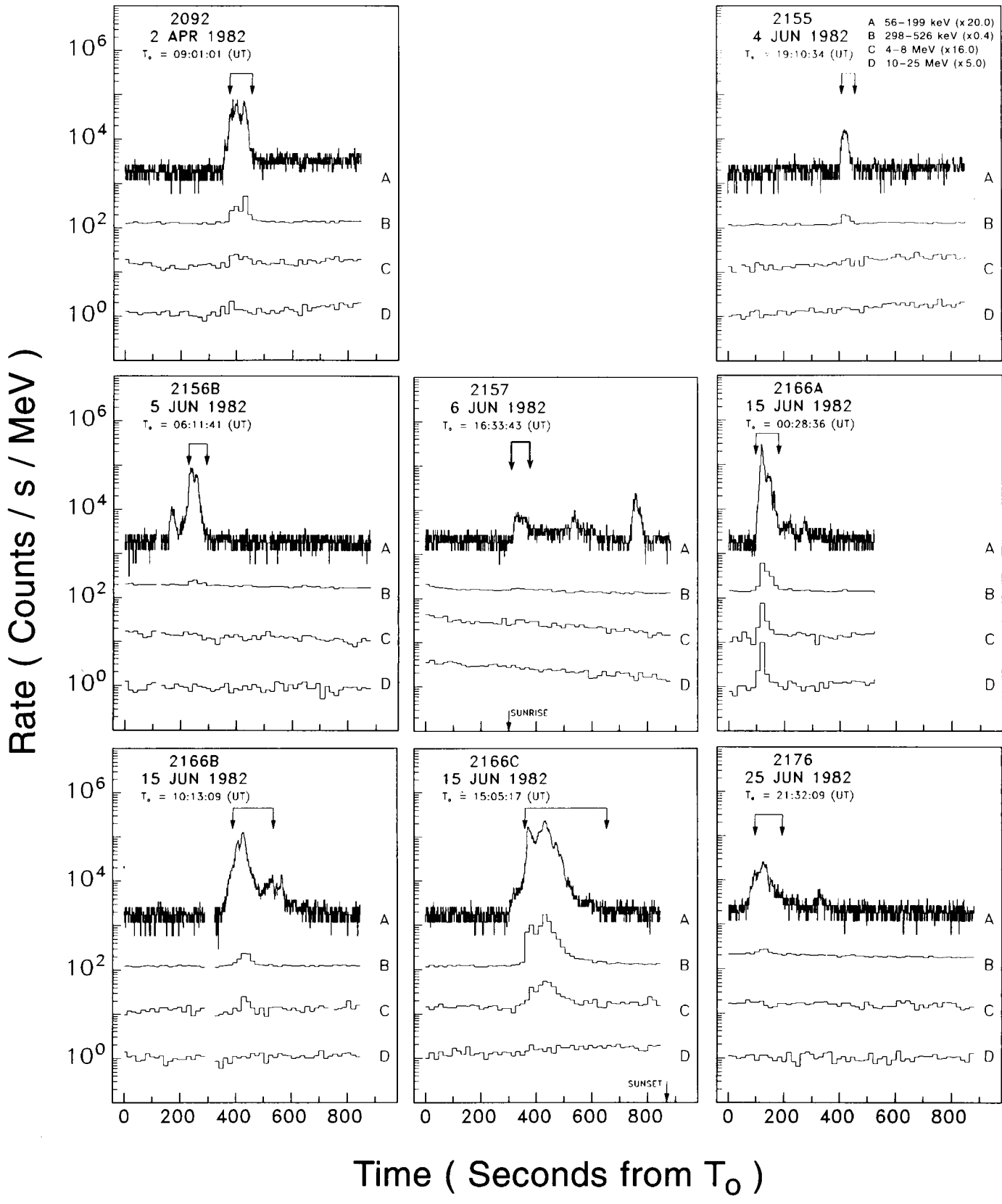


FIG. 7a

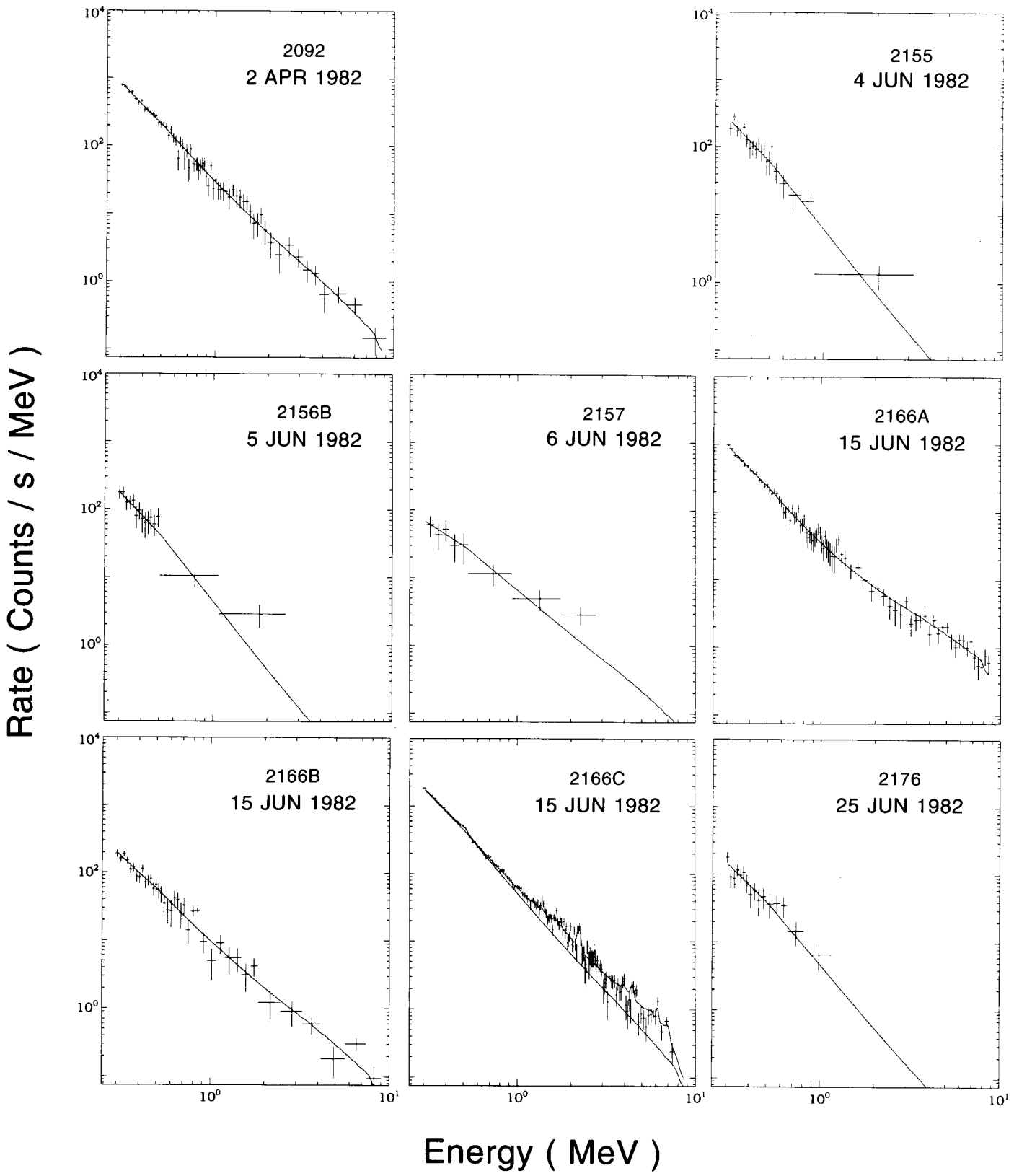


FIG. 7b

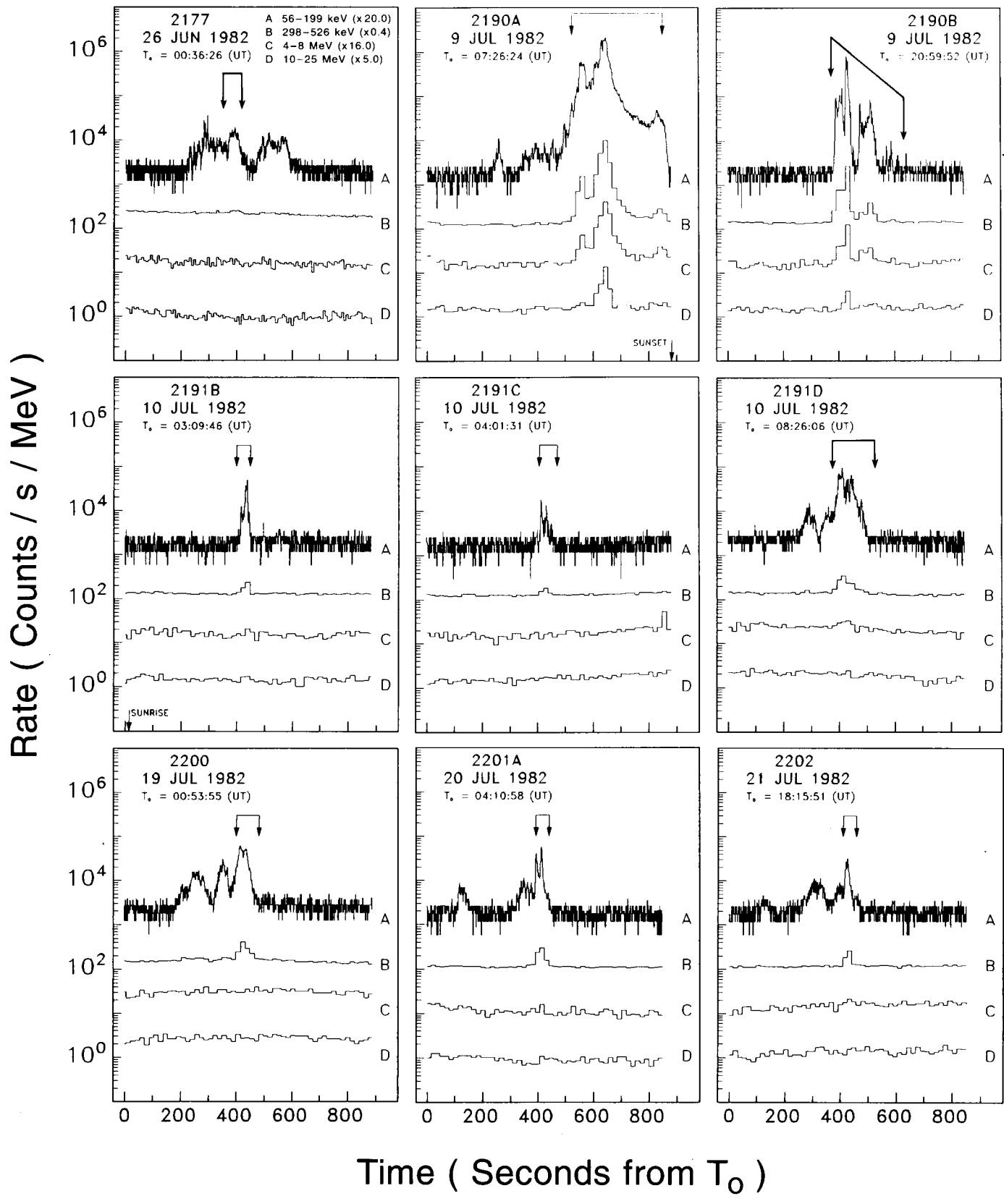


FIG. 8a

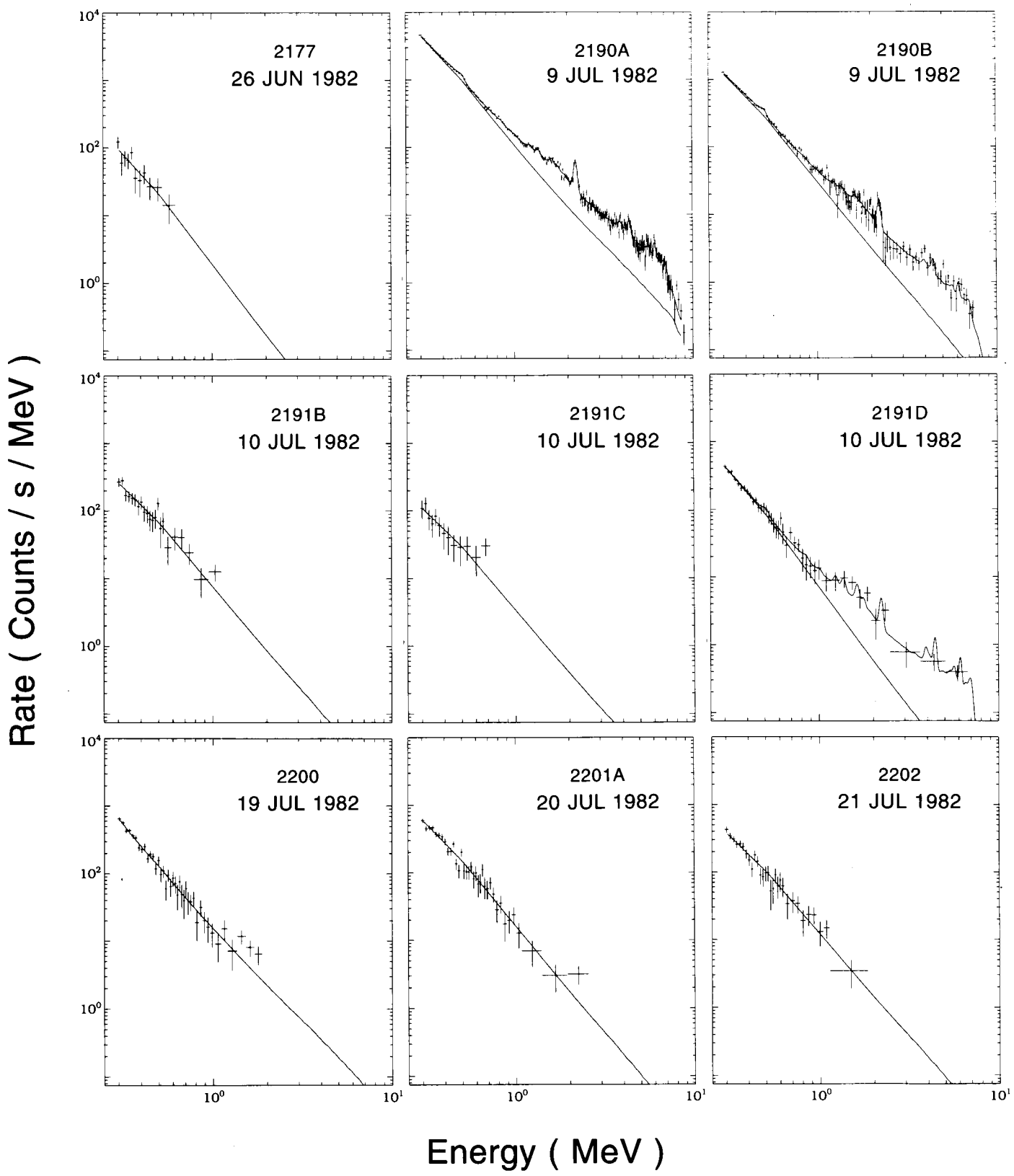


FIG. 8b

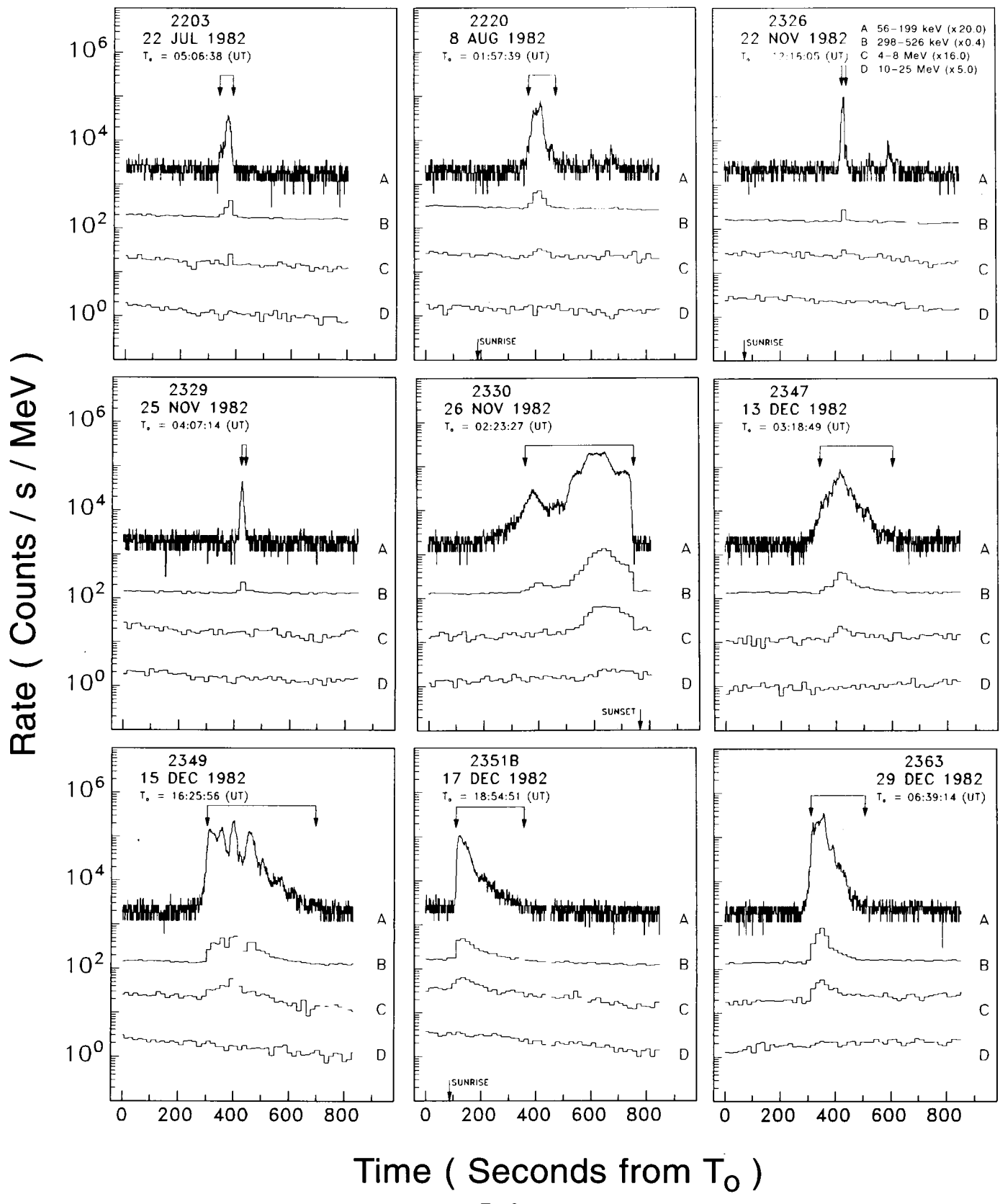


FIG. 9a

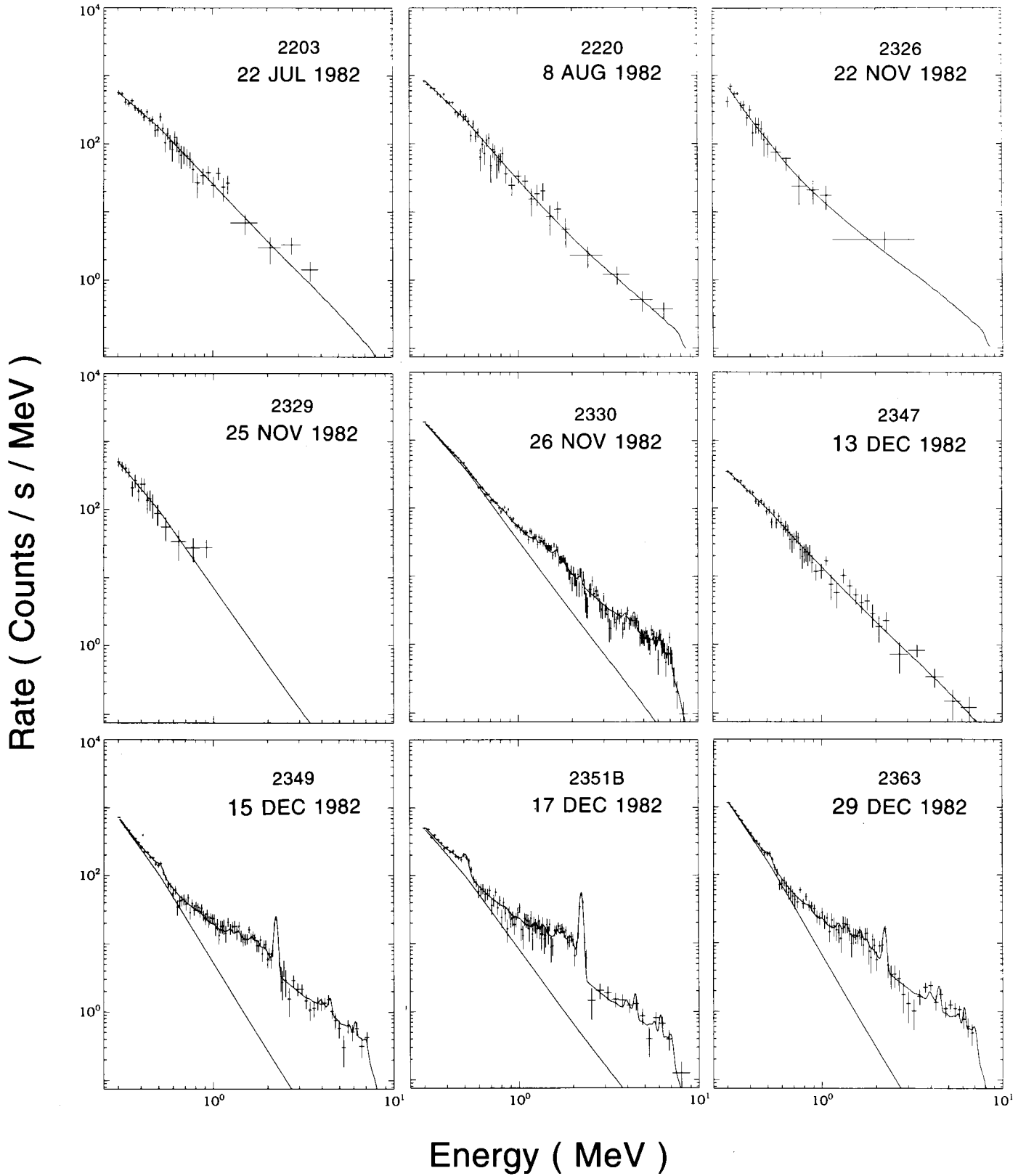


FIG. 9b

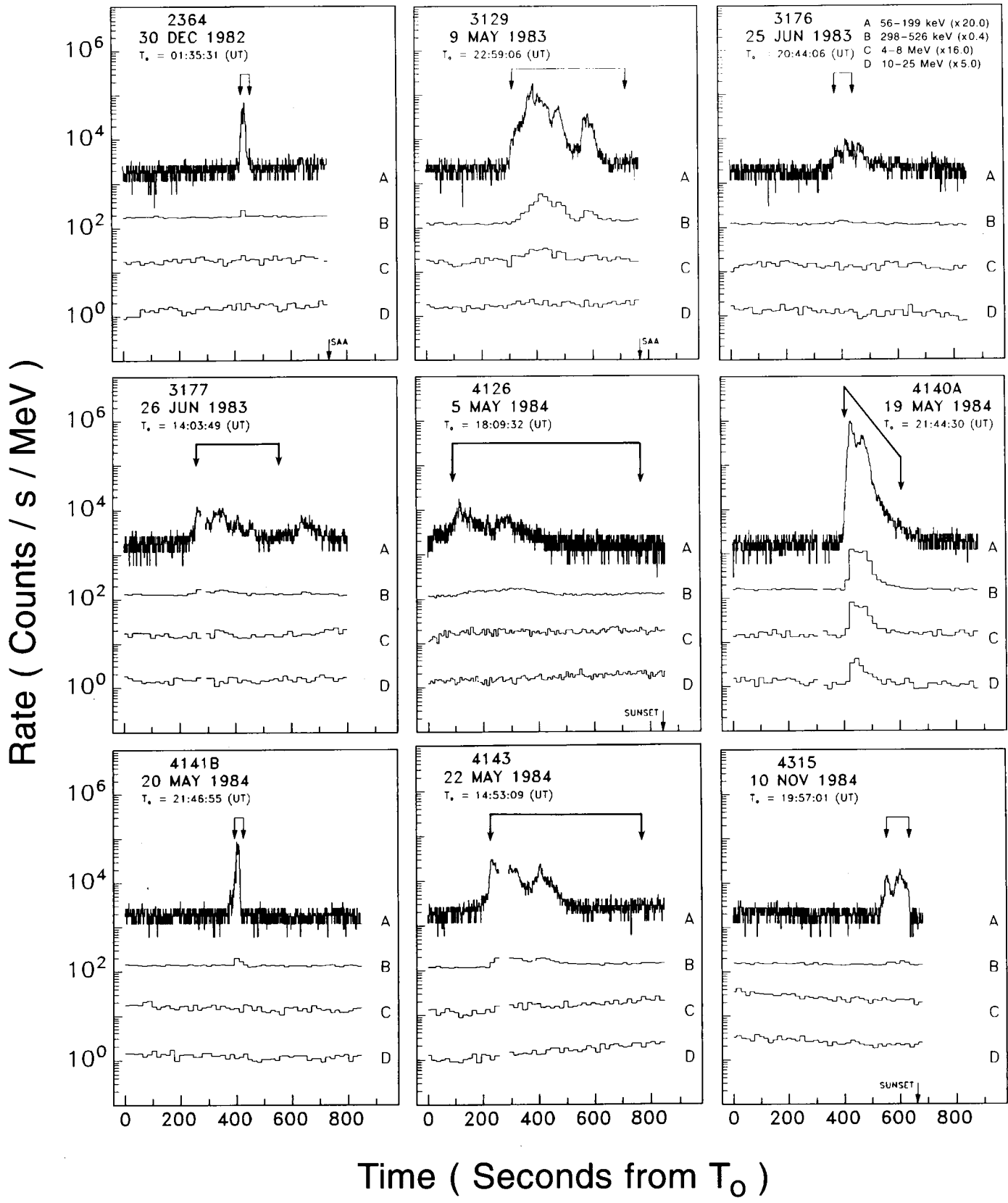


FIG. 10a

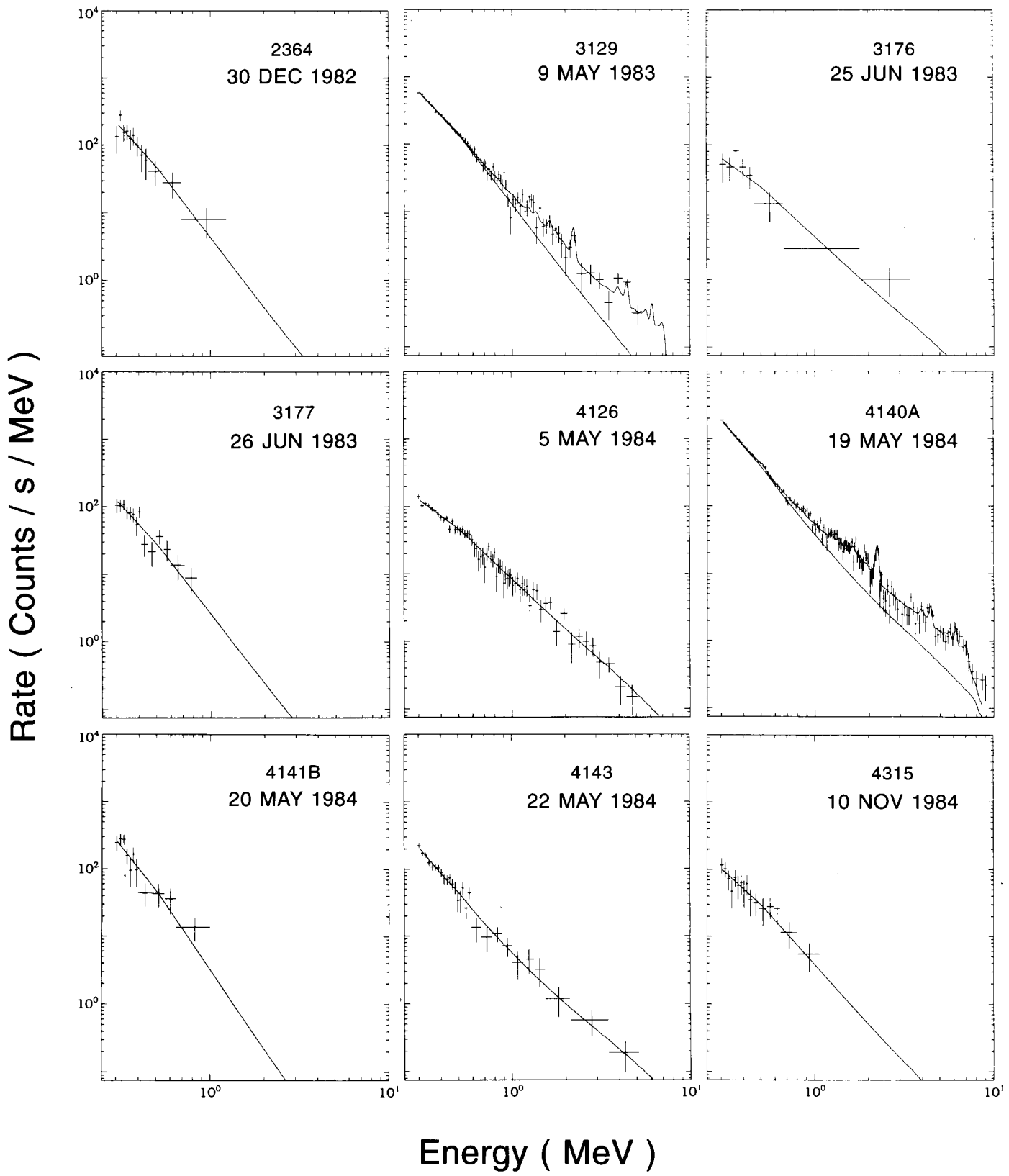


FIG. 10b

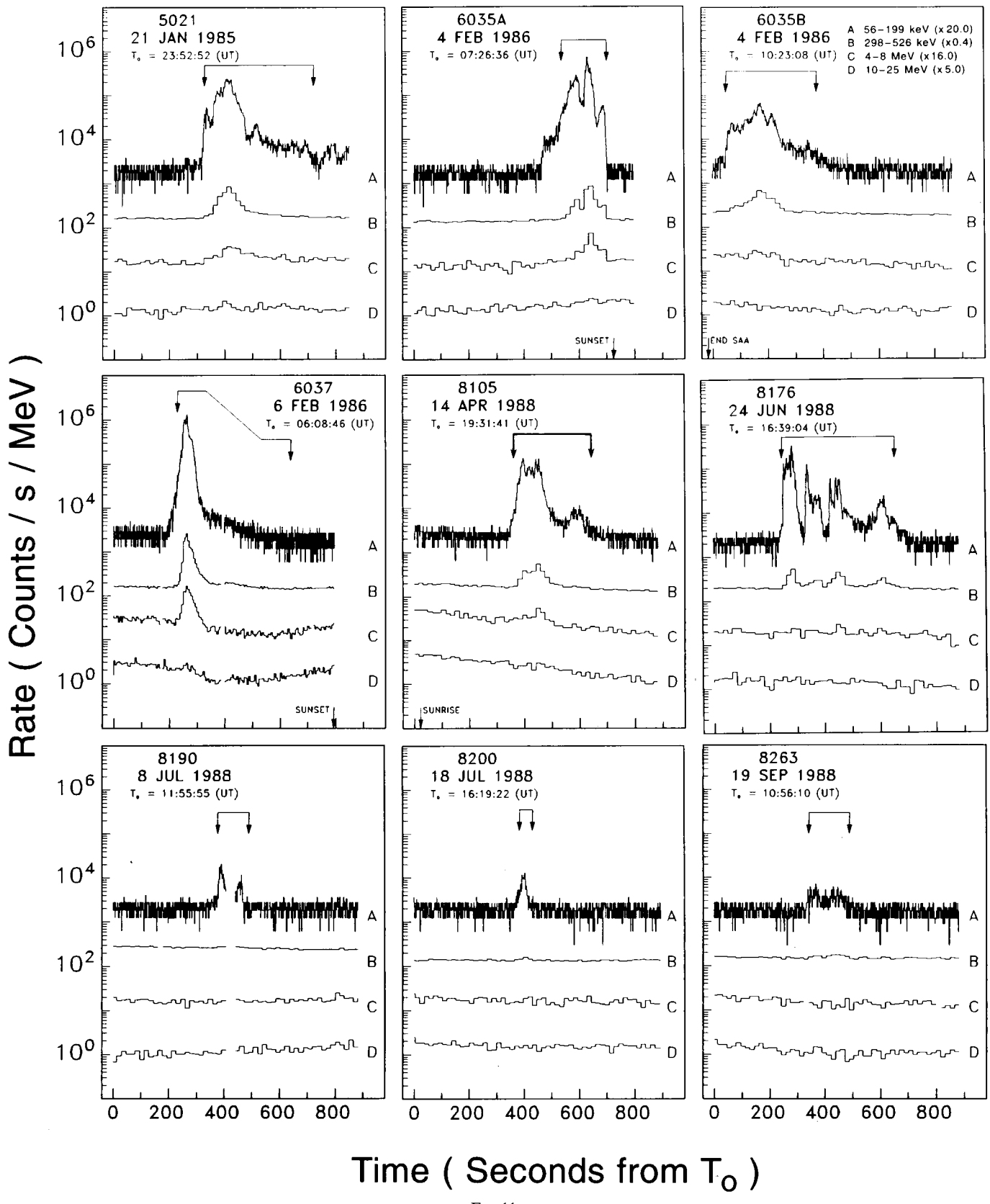


FIG. 11a

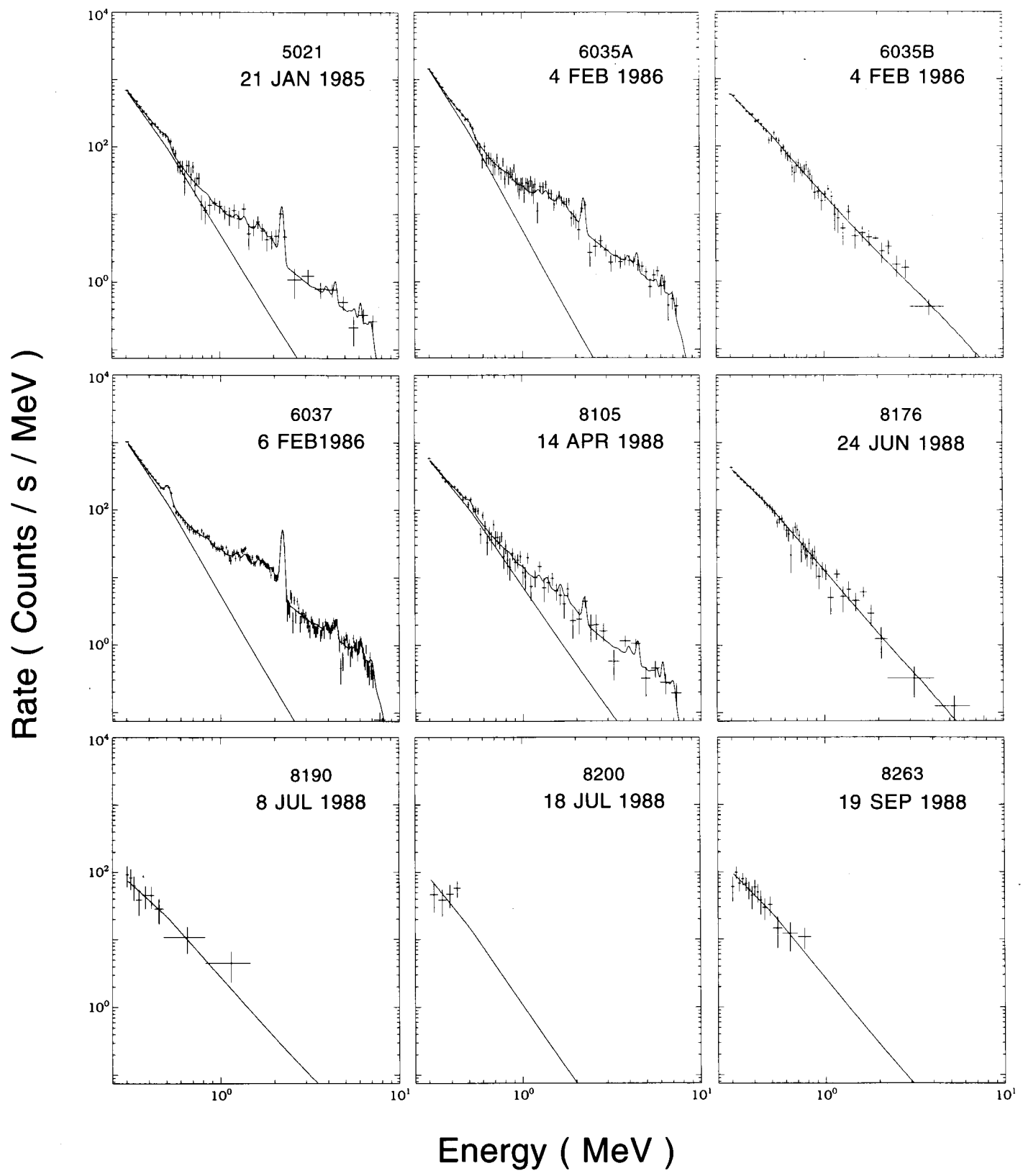


FIG. 11b

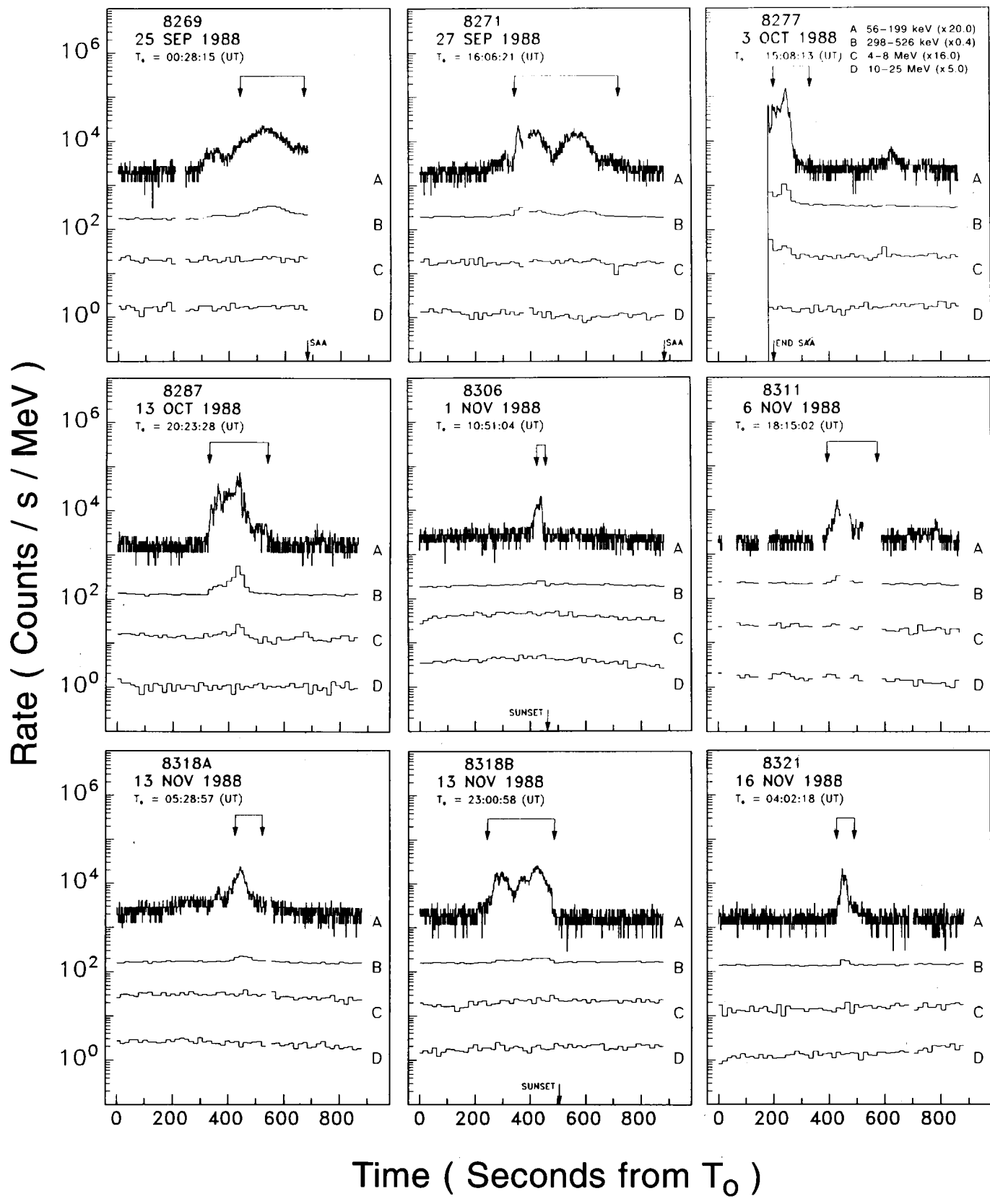


FIG. 12a

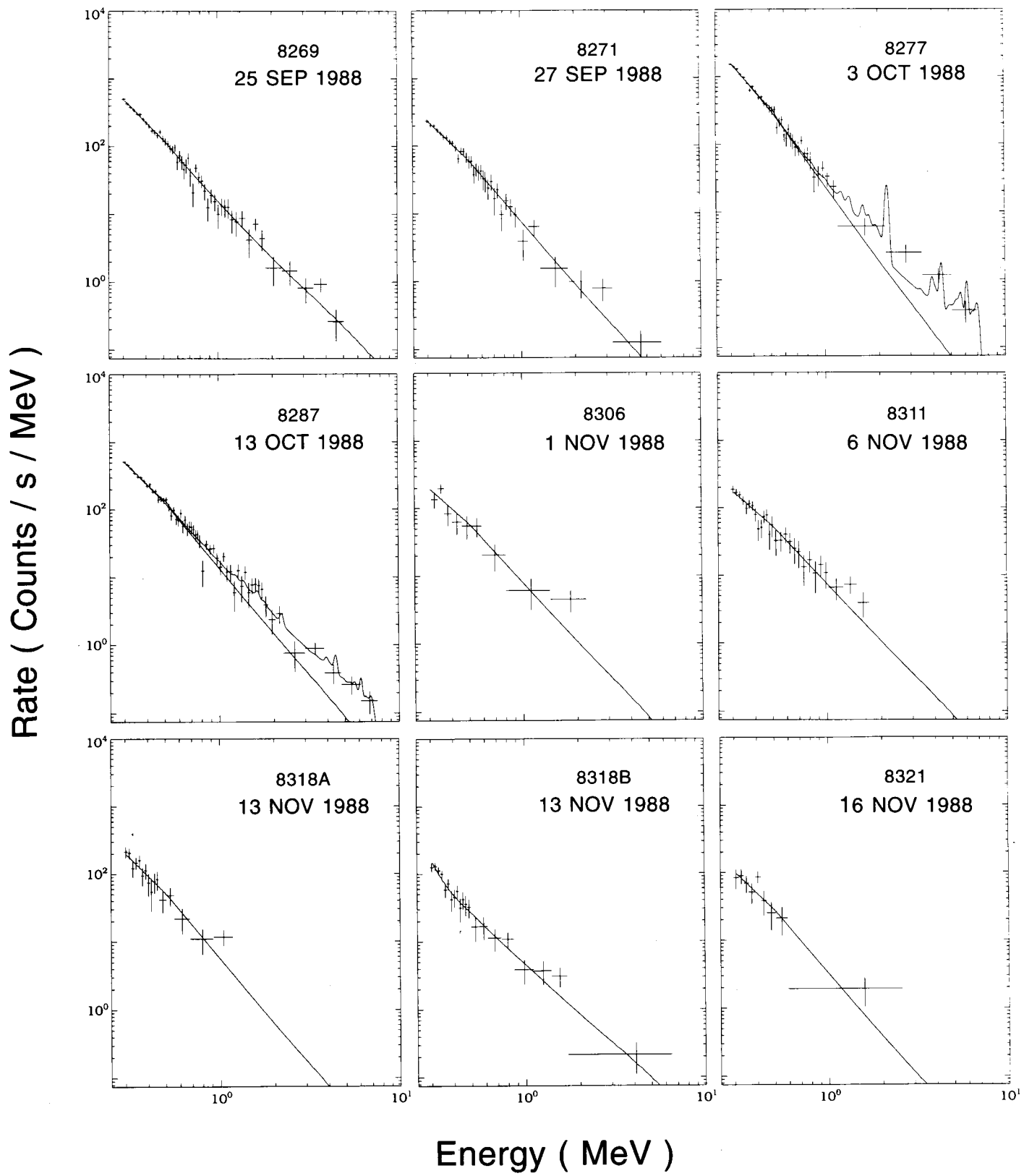


FIG. 12b

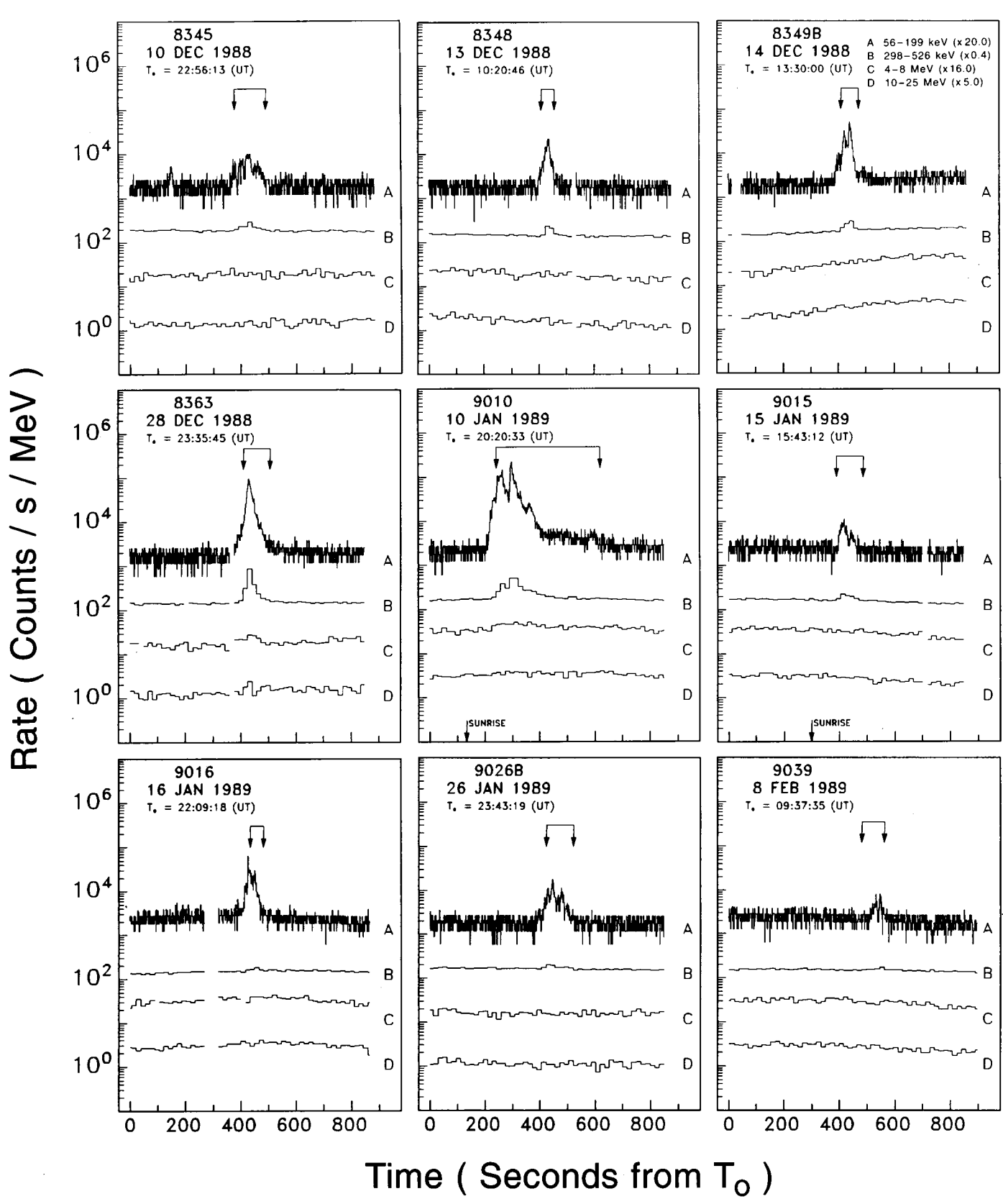


FIG. 13a

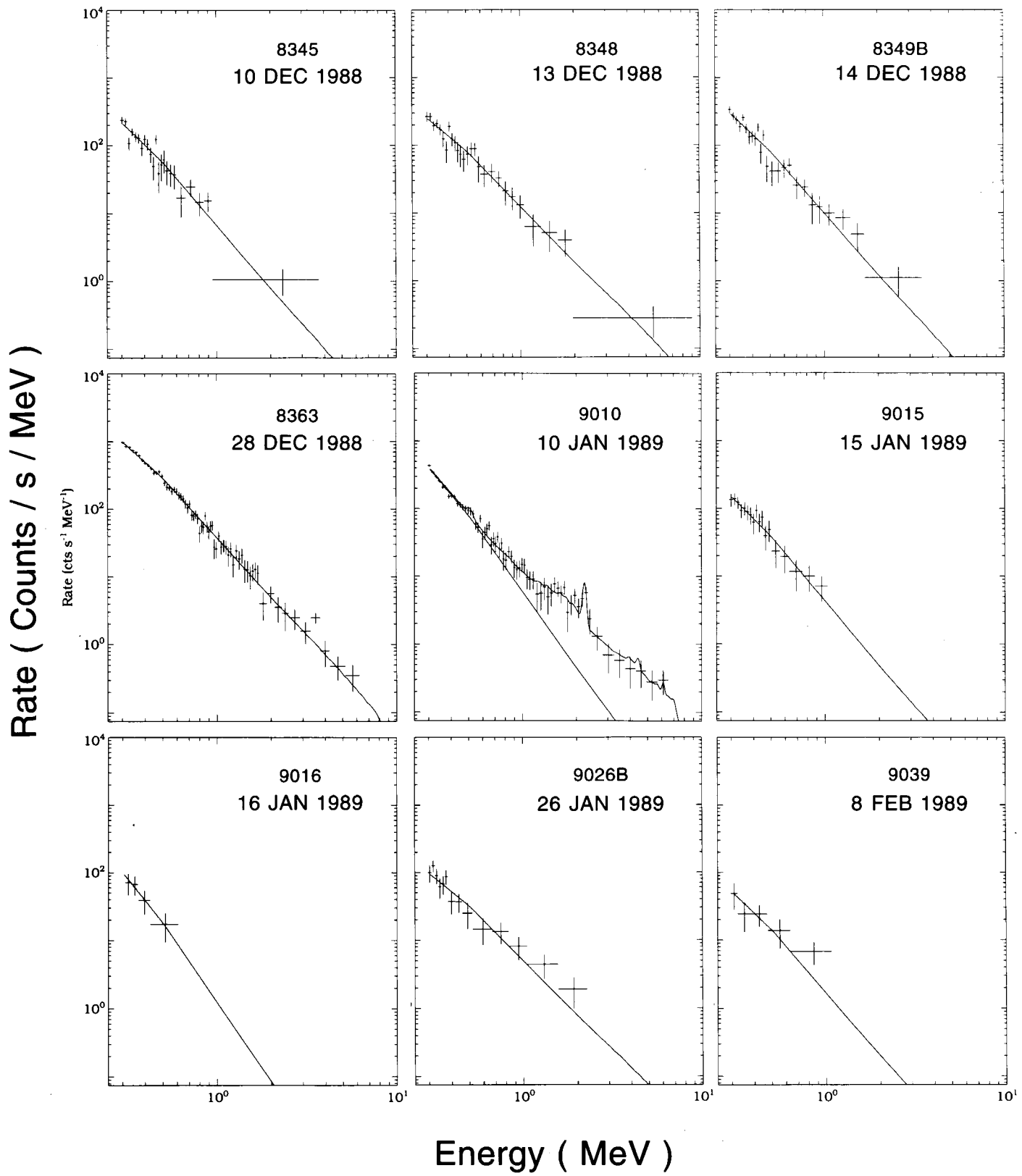


FIG. 13b

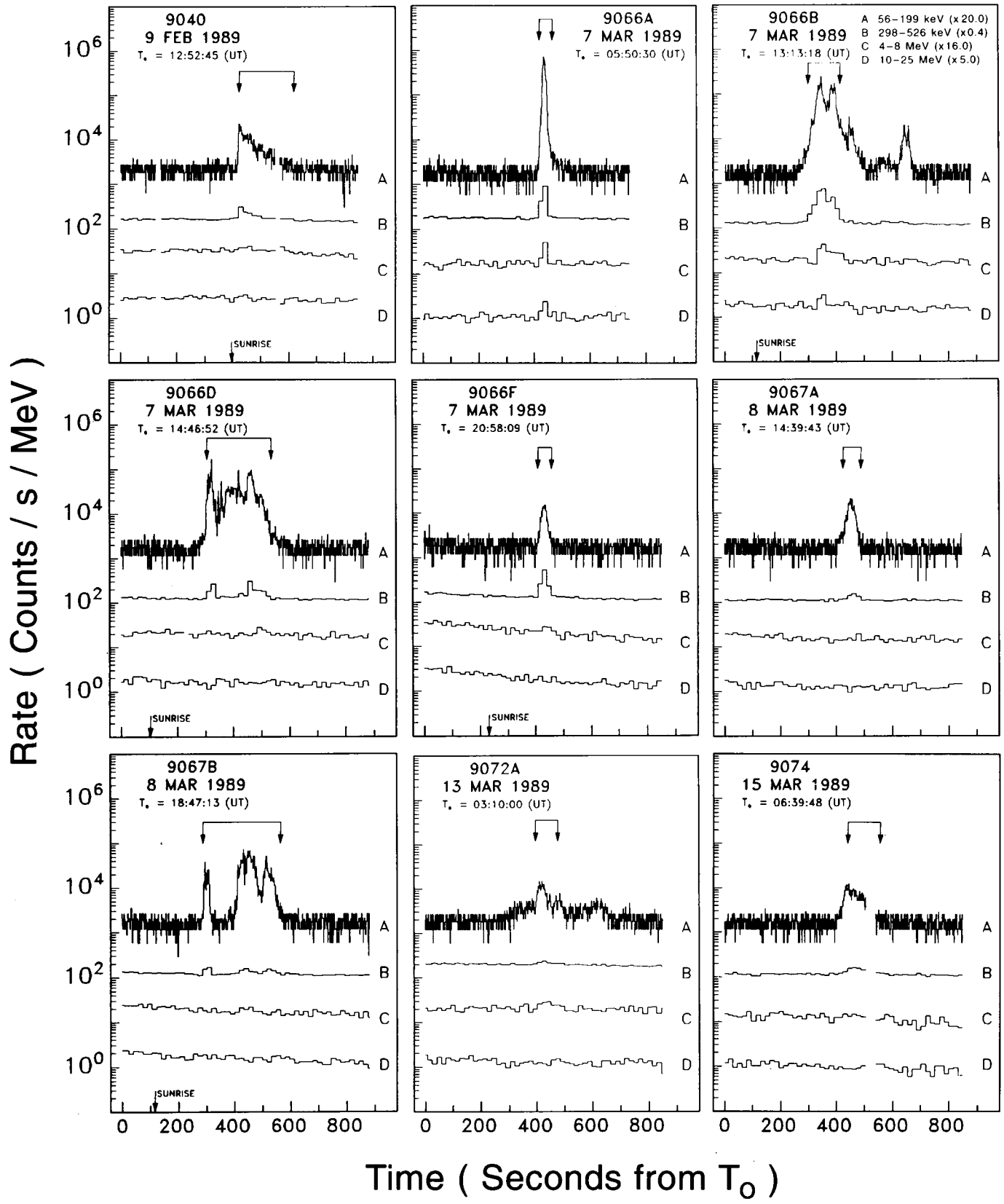


FIG. 14a

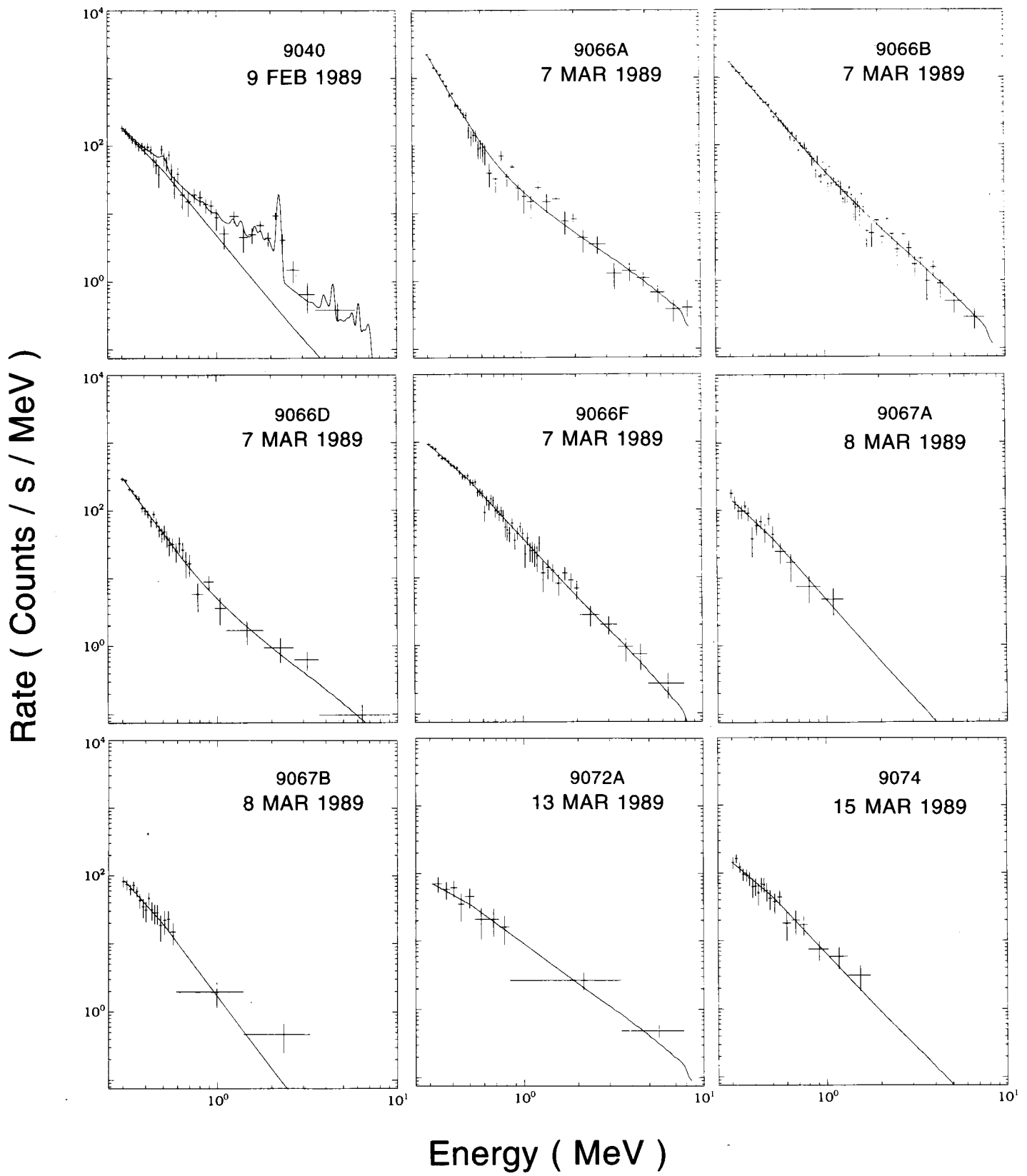


FIG. 14b

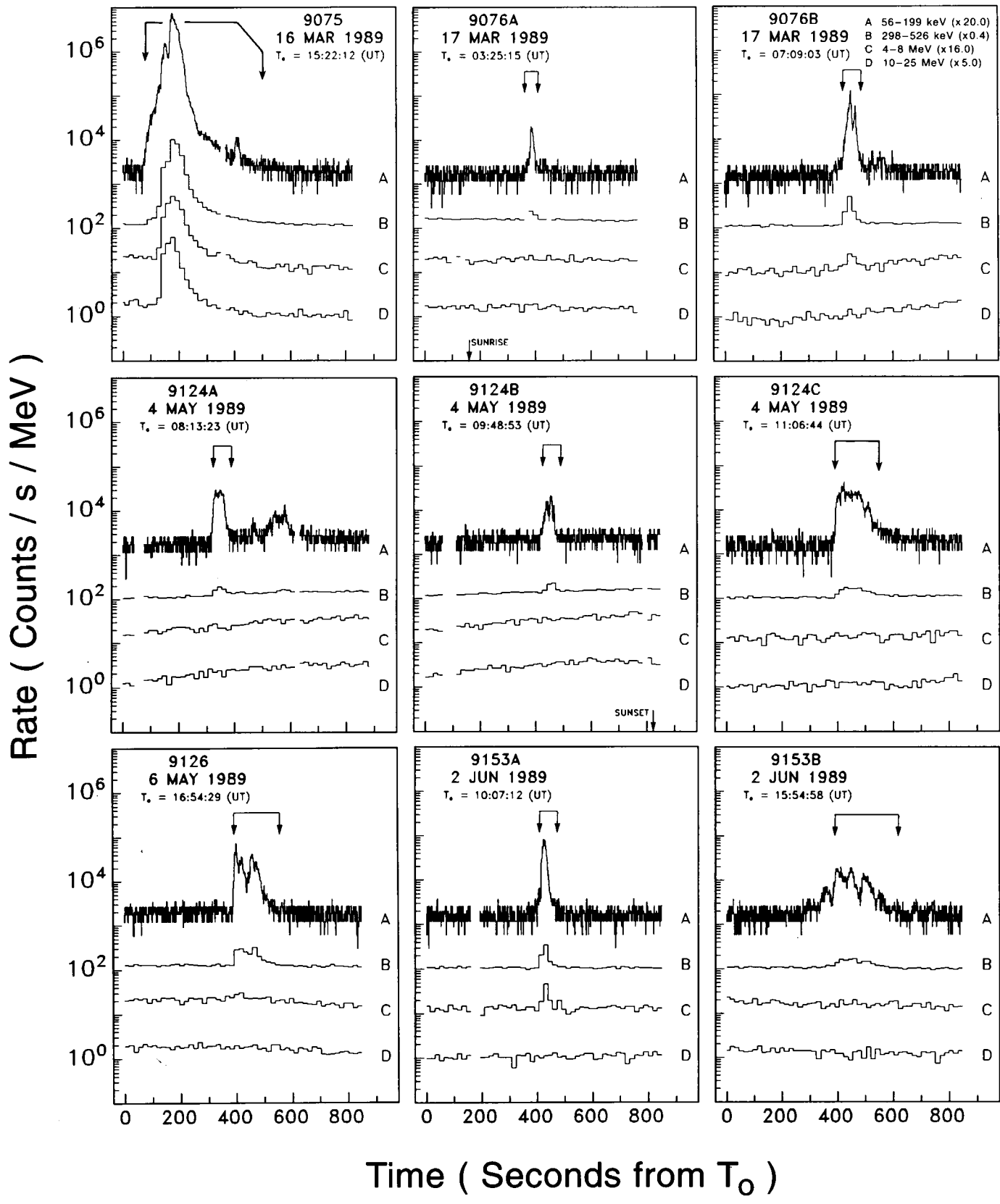


FIG. 15a

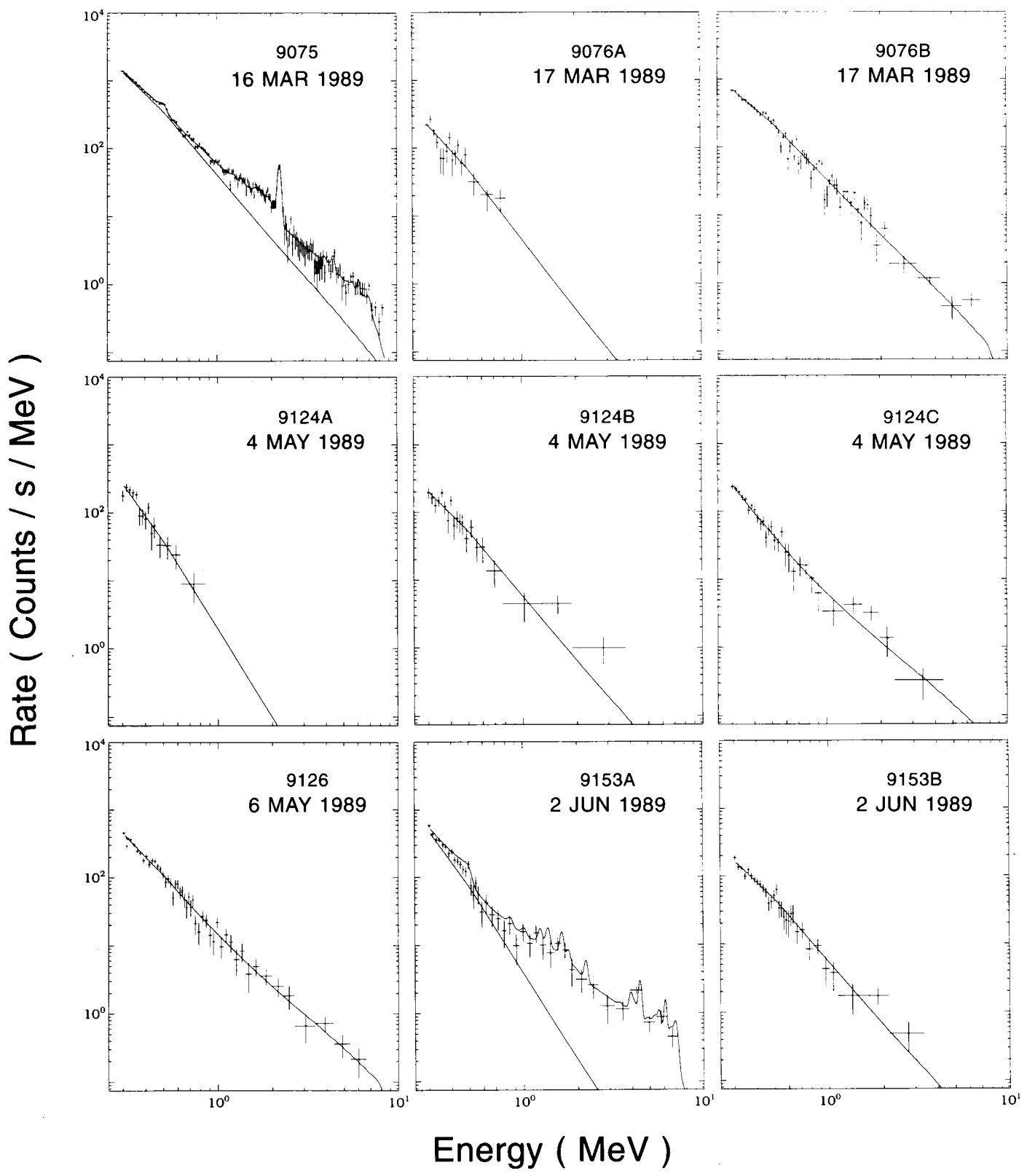


FIG. 15b

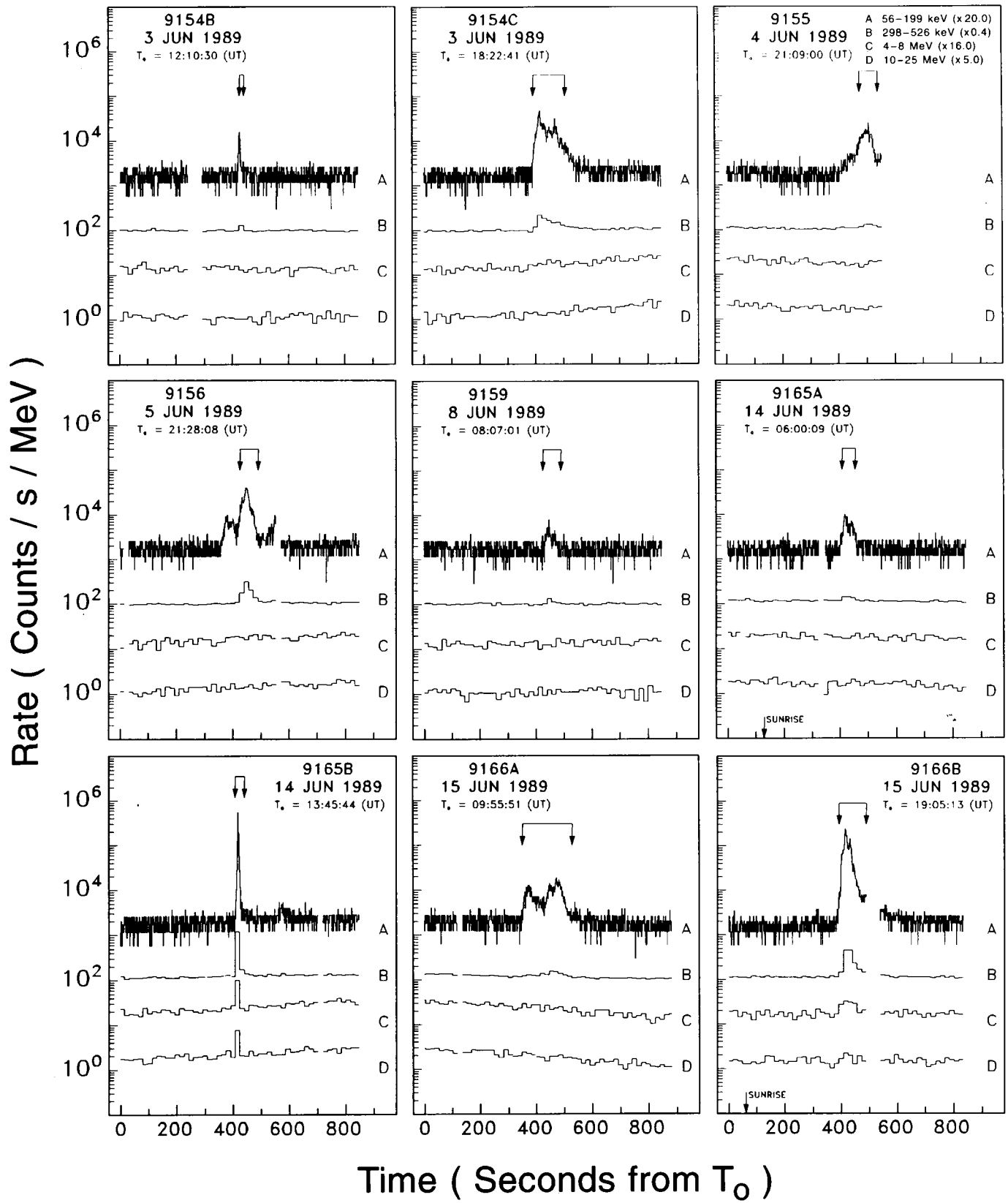


FIG. 16a

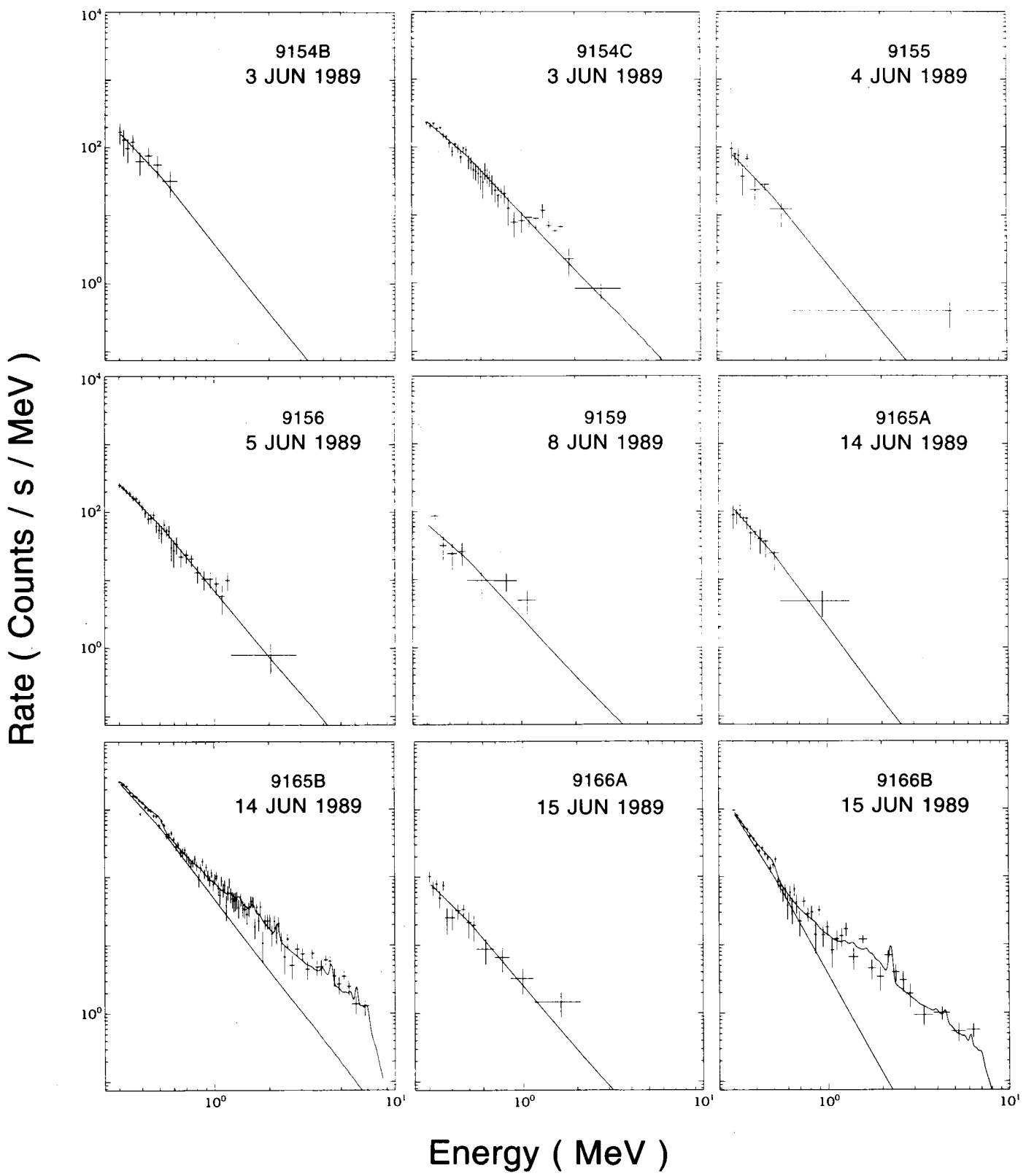


FIG. 16b

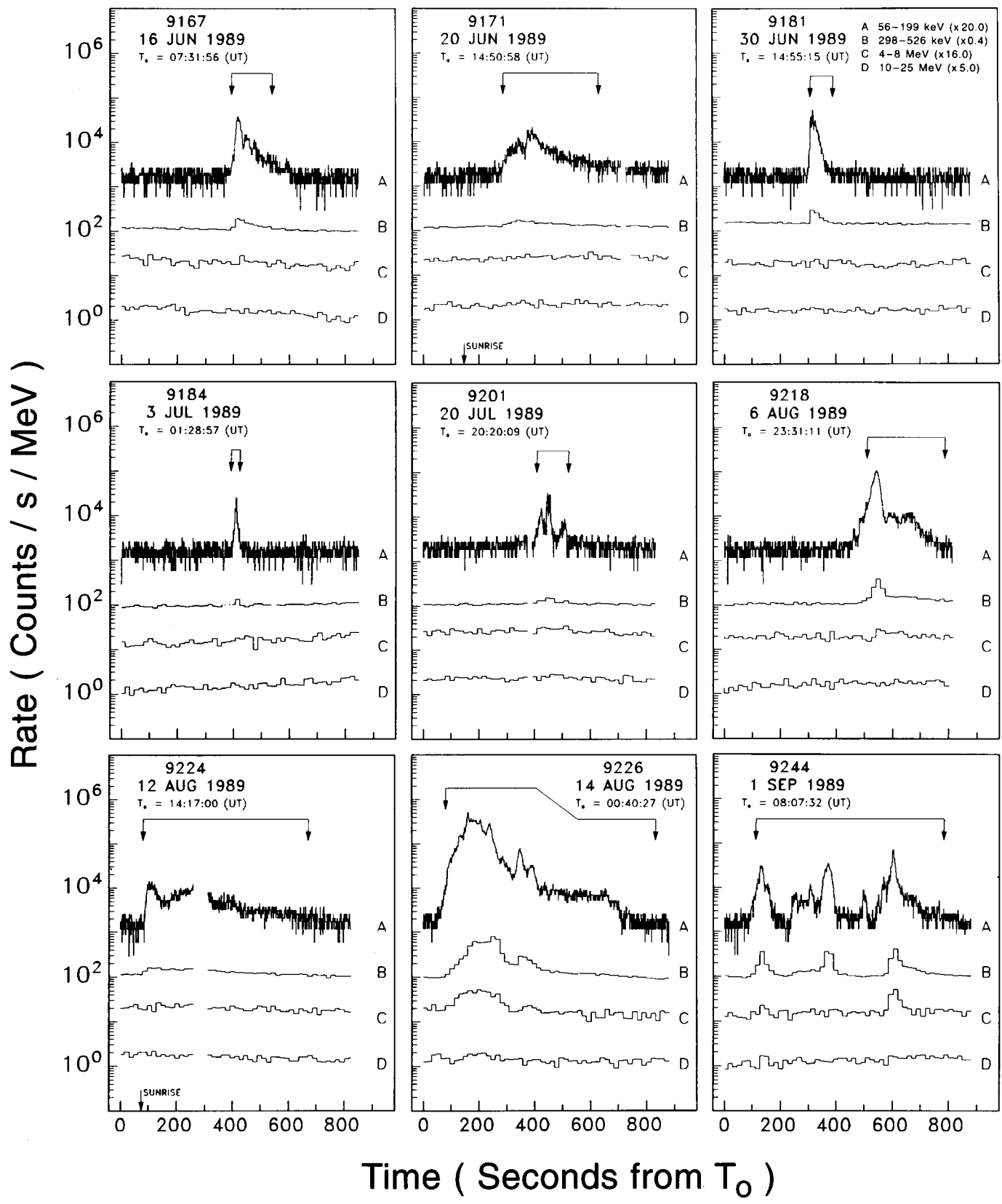


FIG. 17a

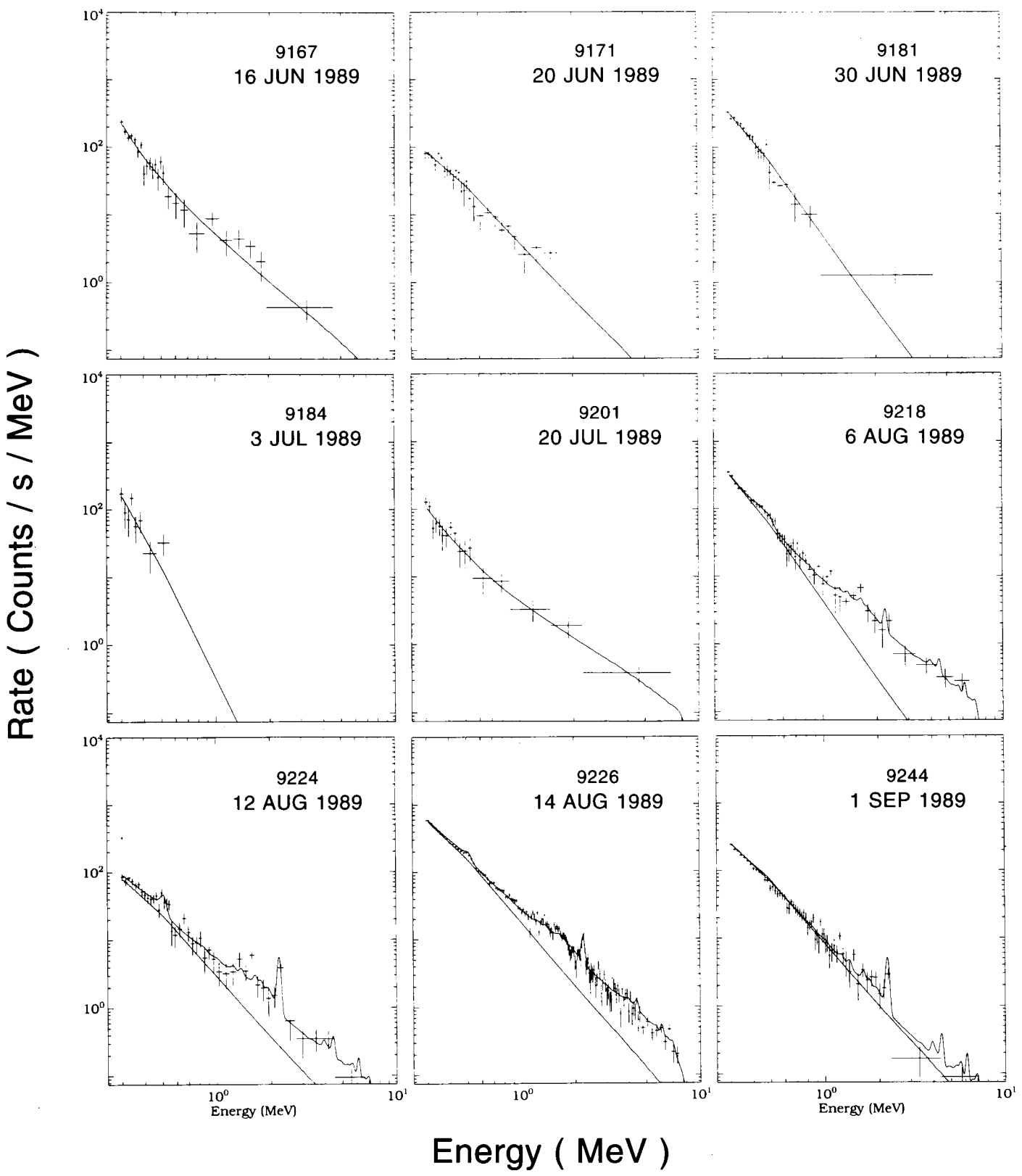


FIG. 17b

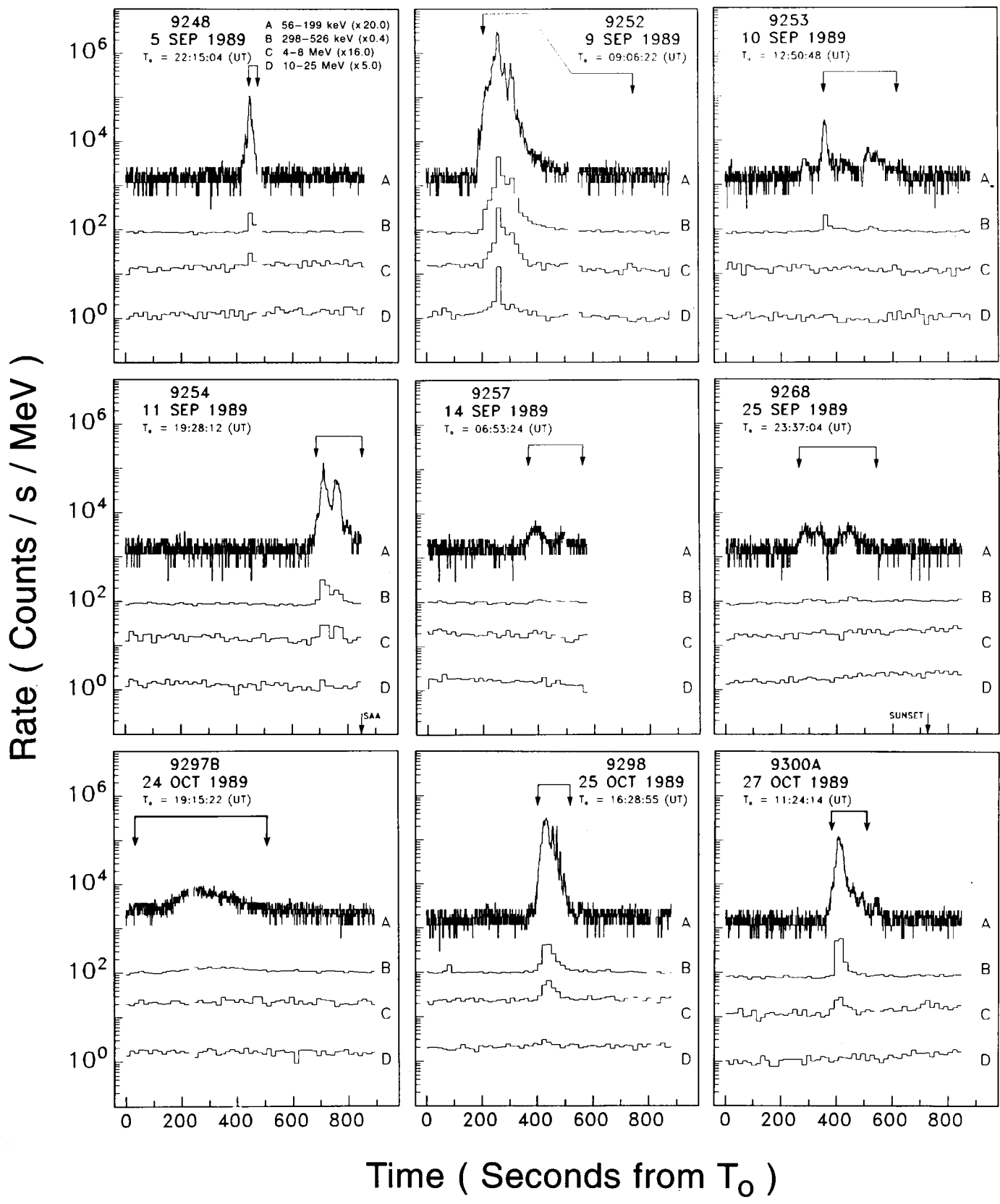


FIG. 18a

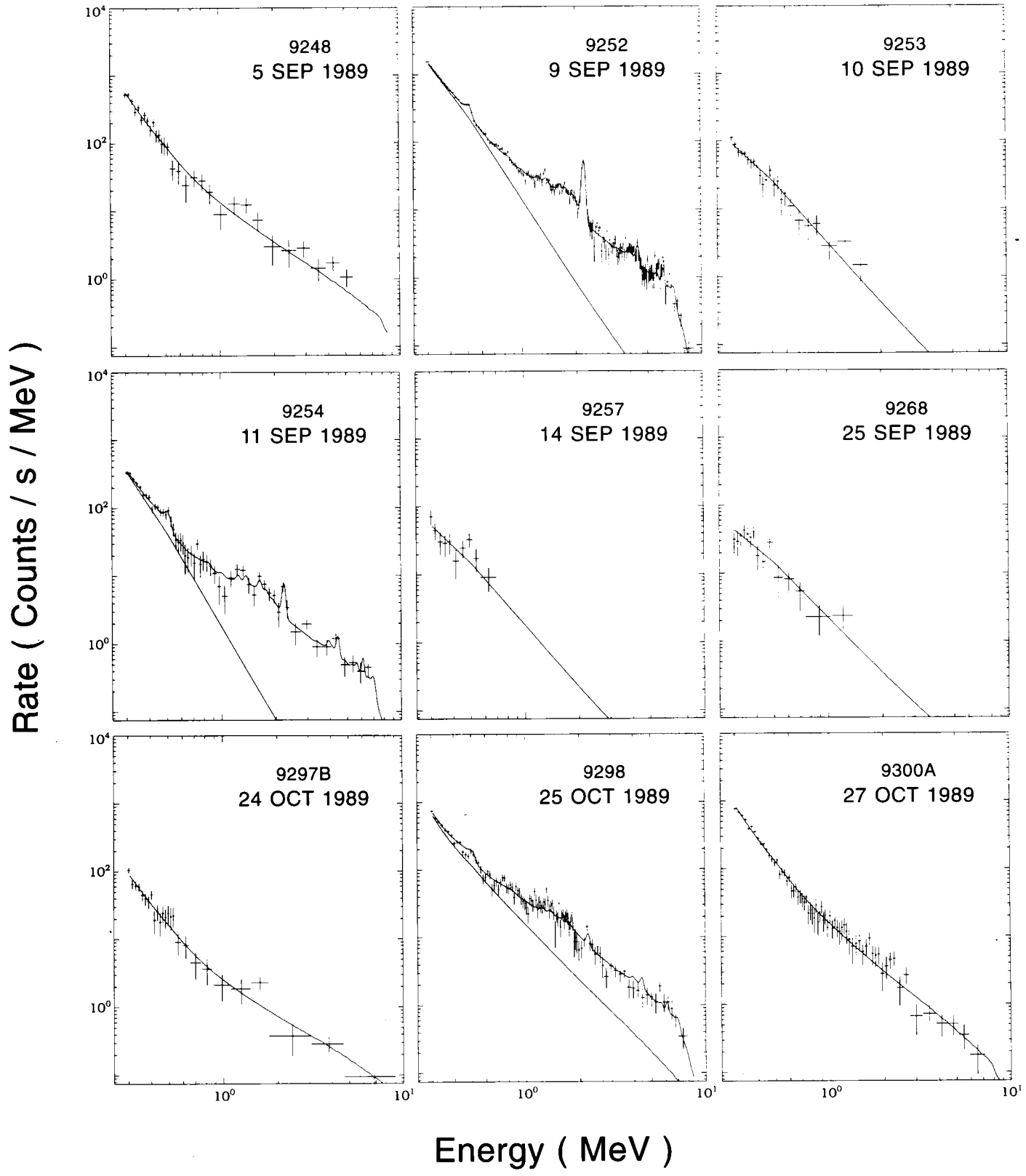


FIG. 18b

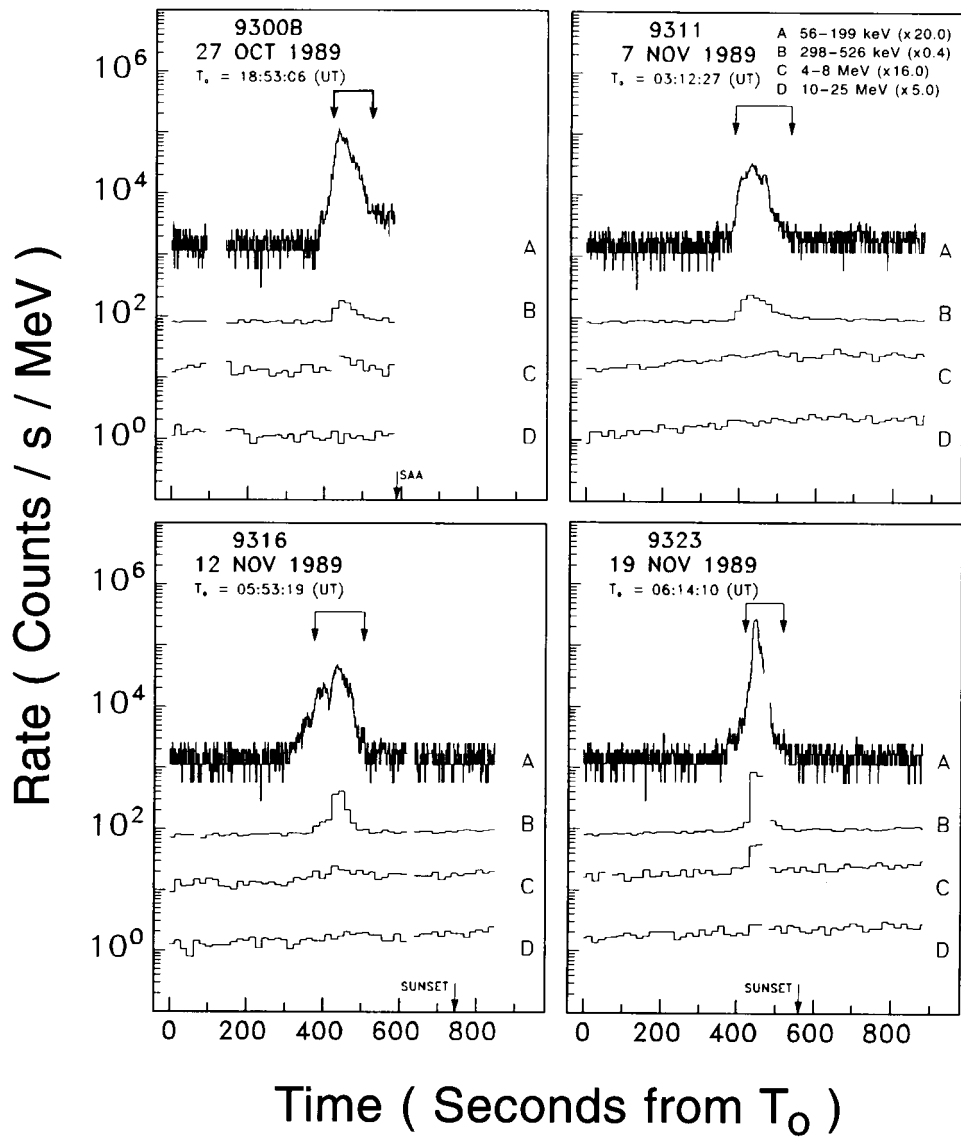


FIG. 19a

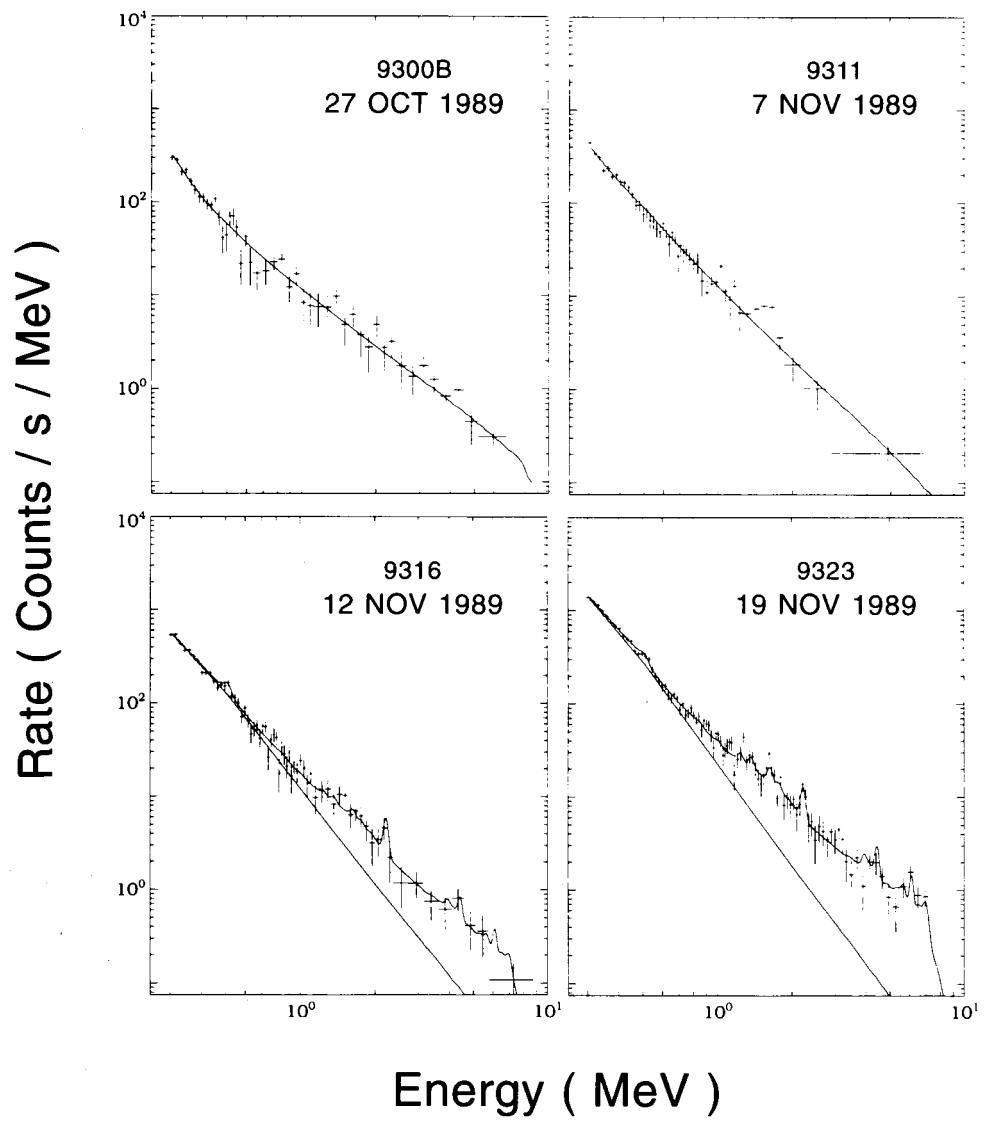


FIG. 19b

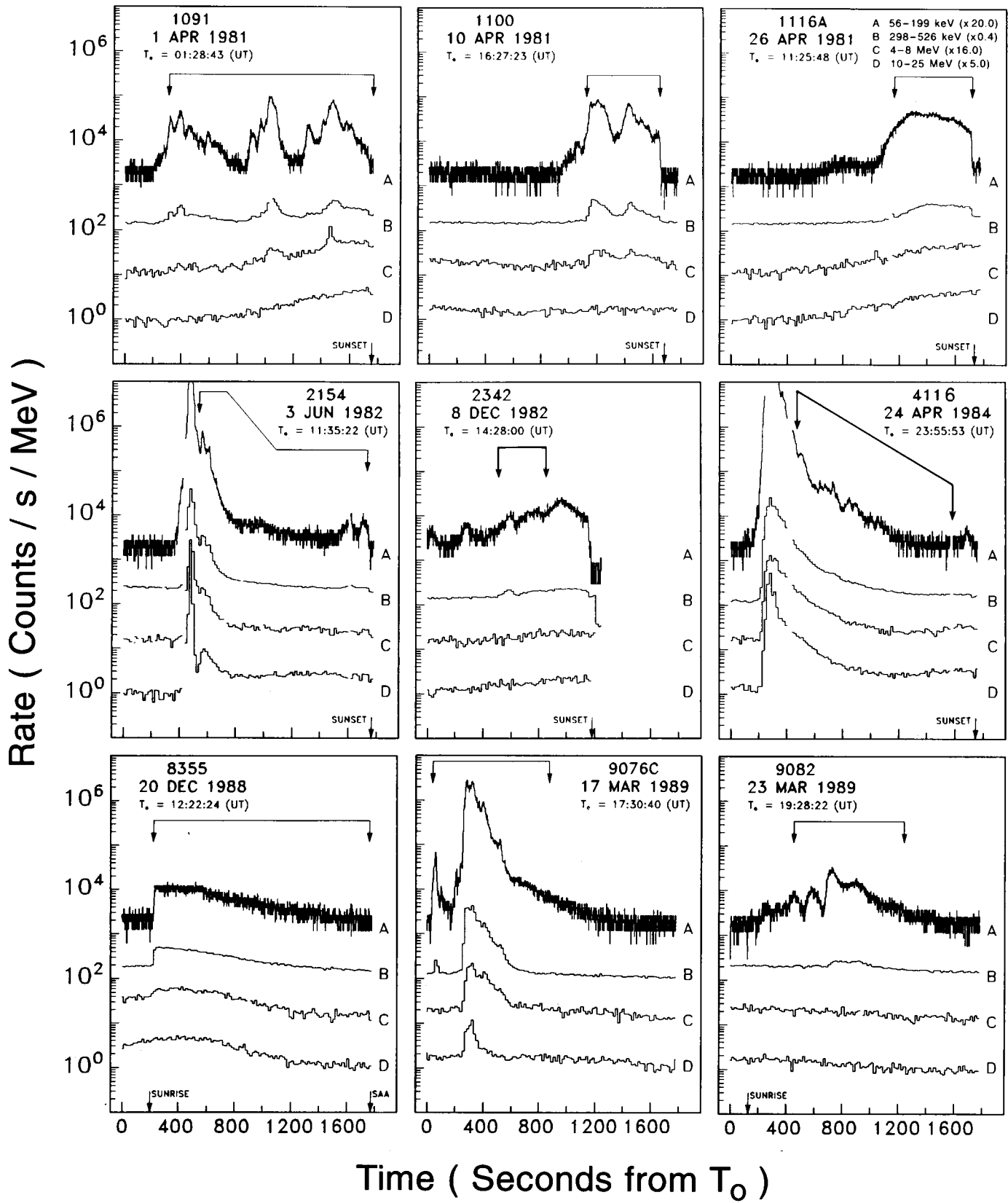


FIG. 20a

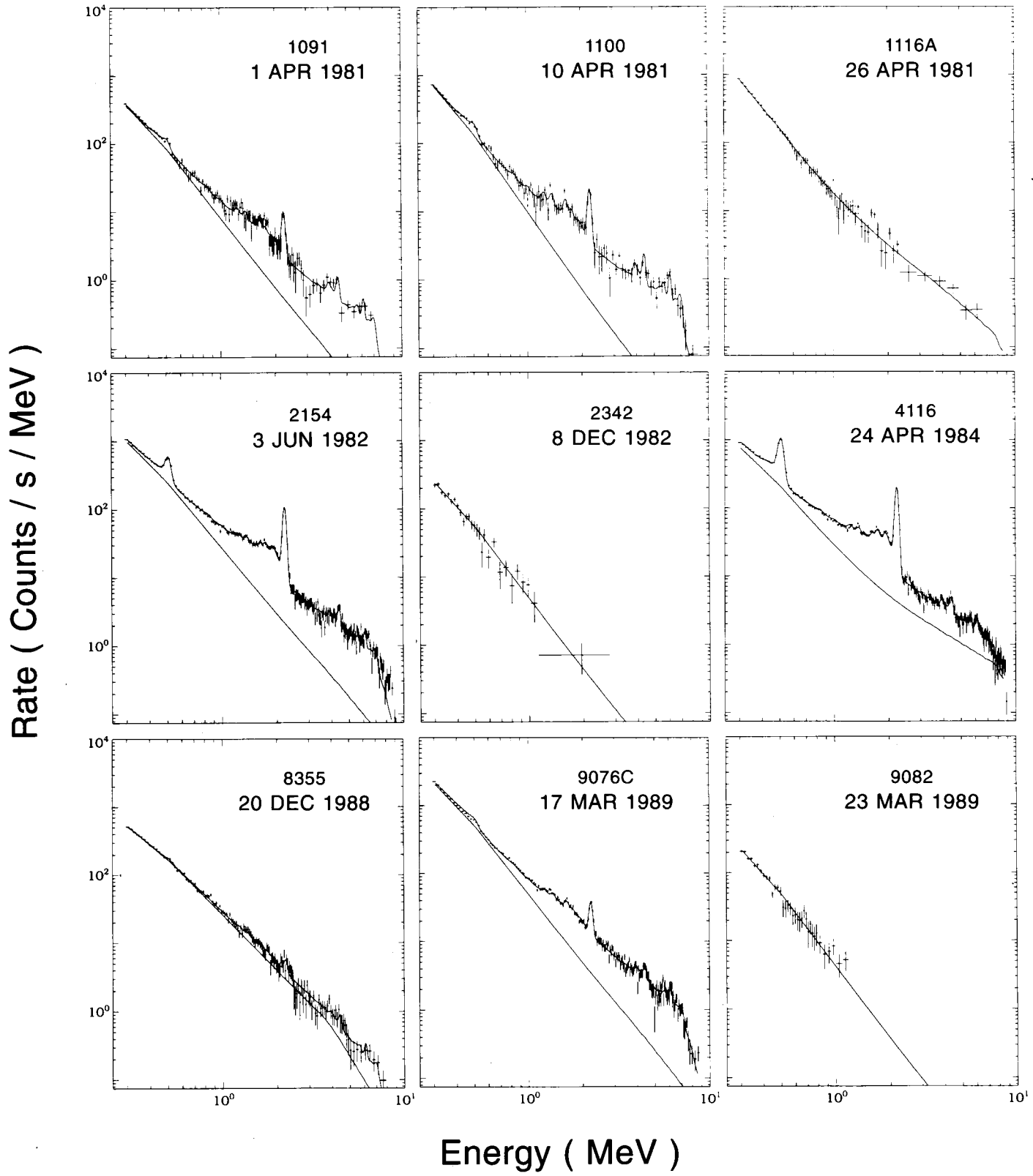


FIG. 20b

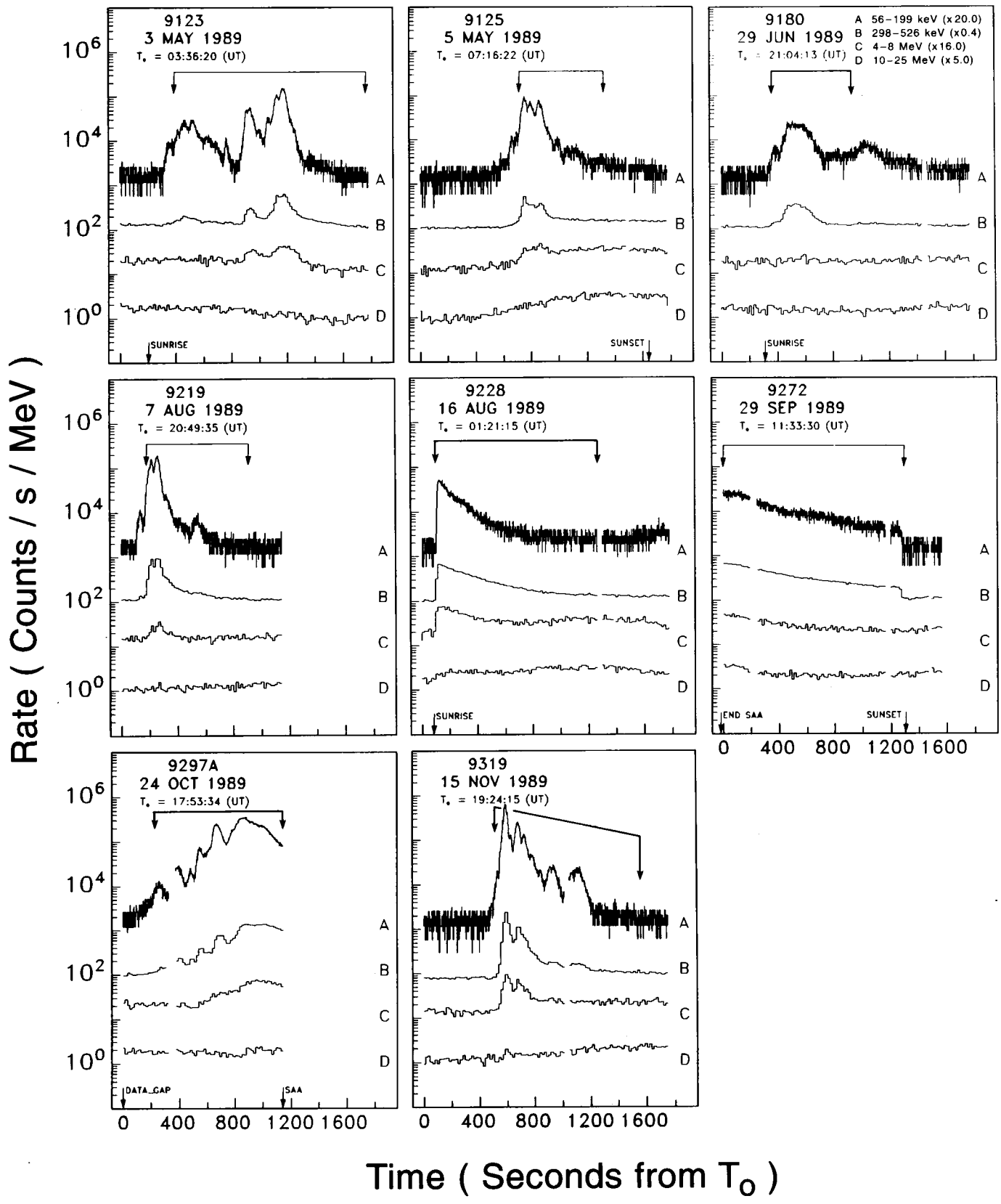


FIG. 21a

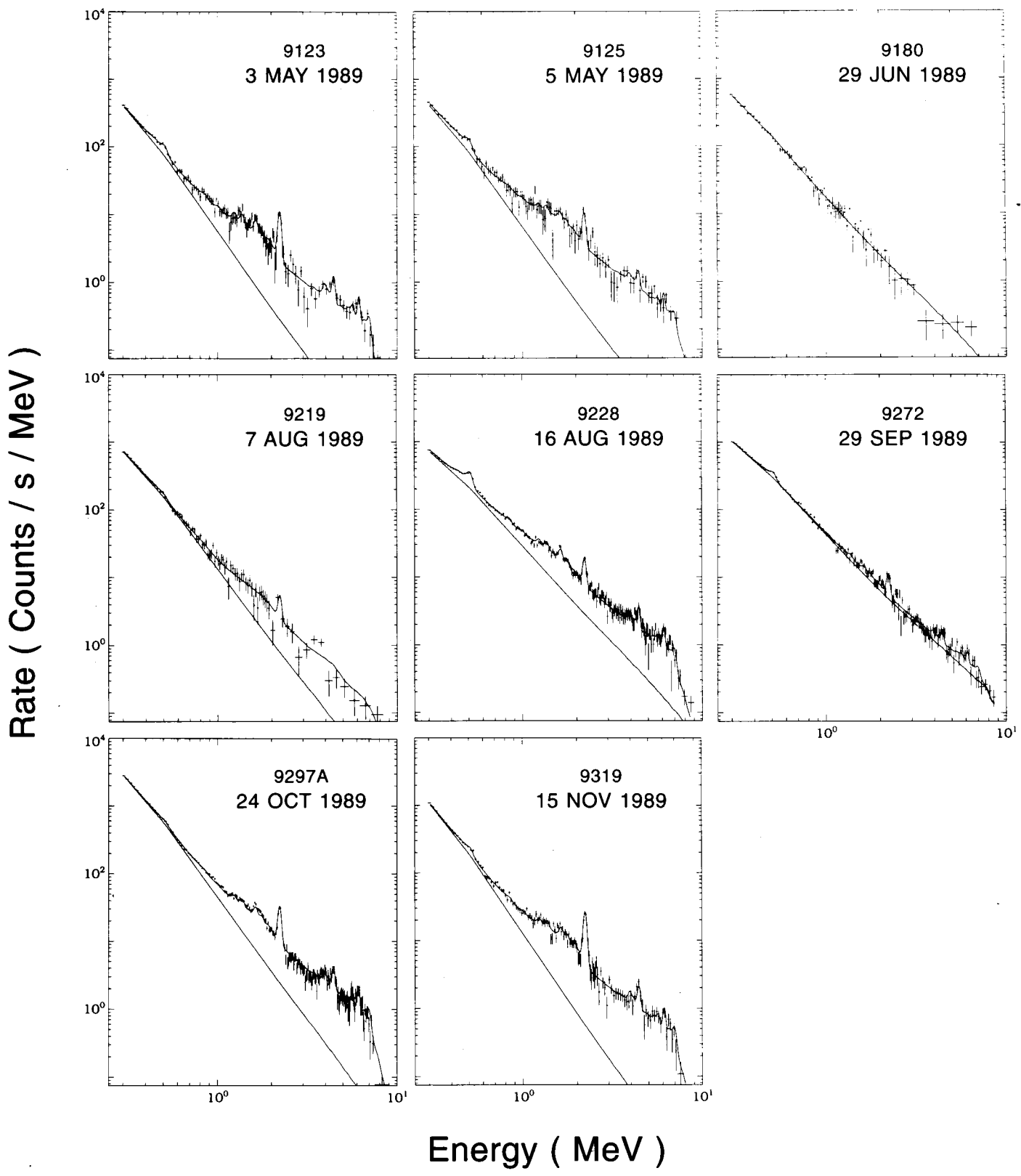


FIG. 21b

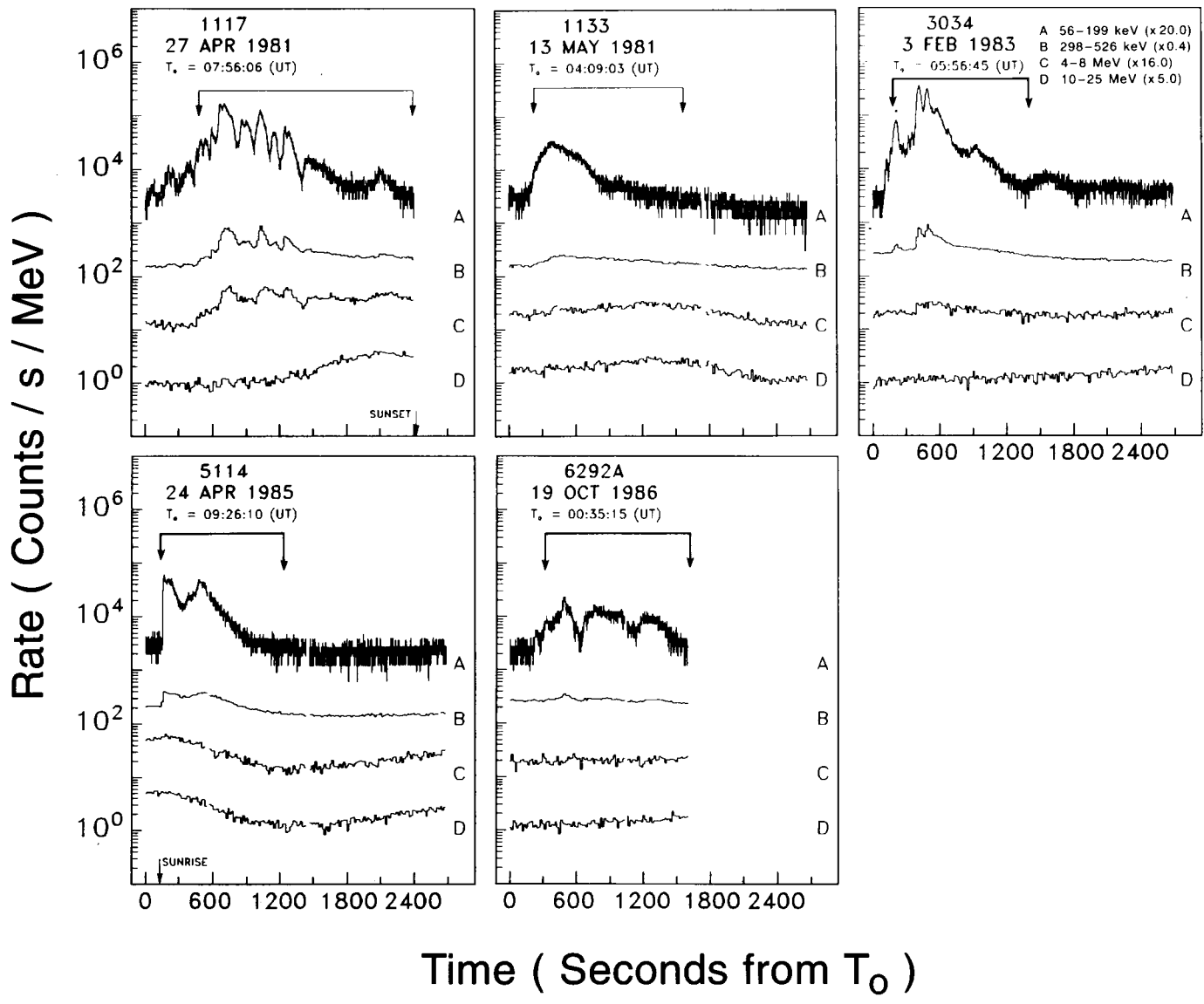


FIG. 22a

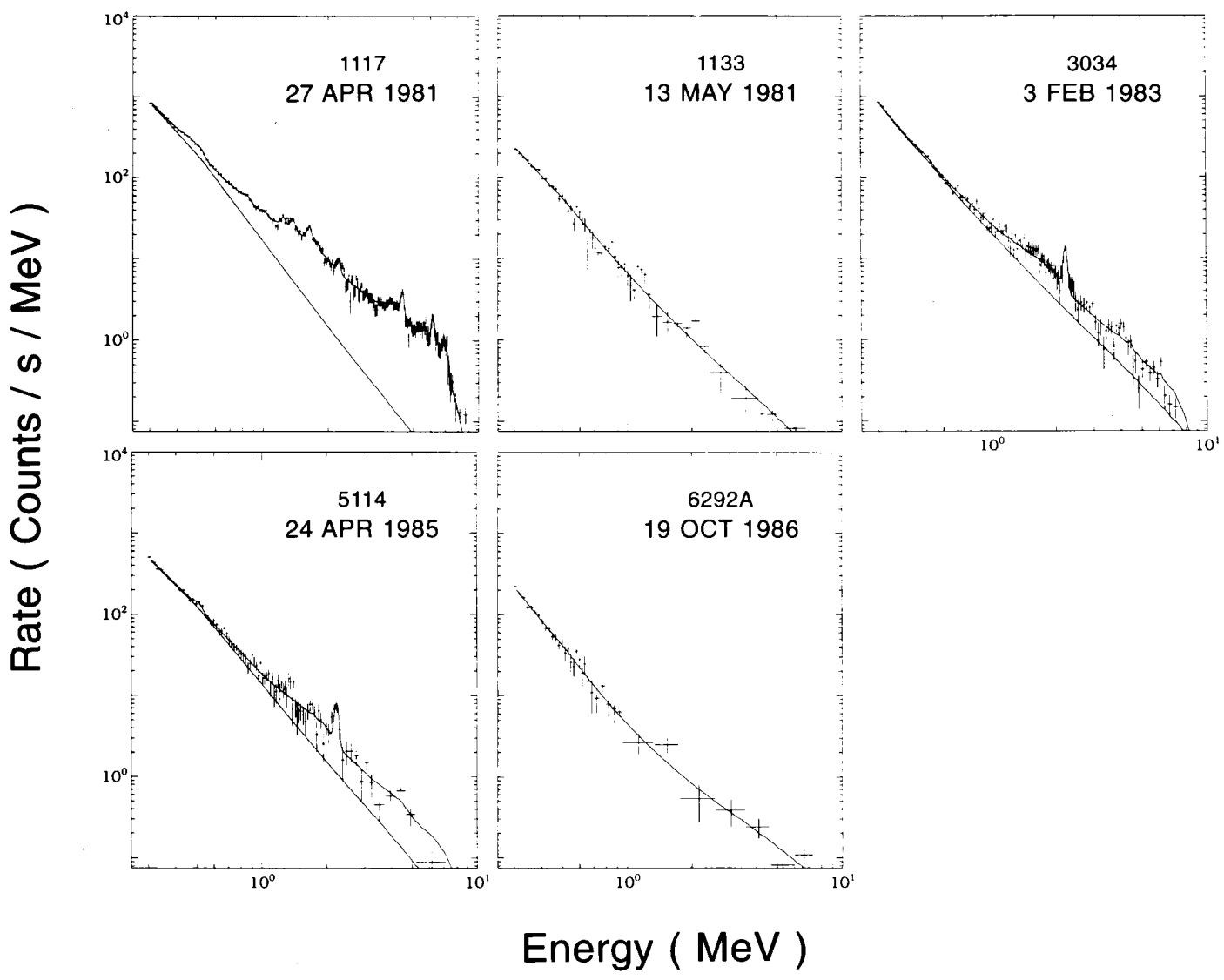


FIG. 22b

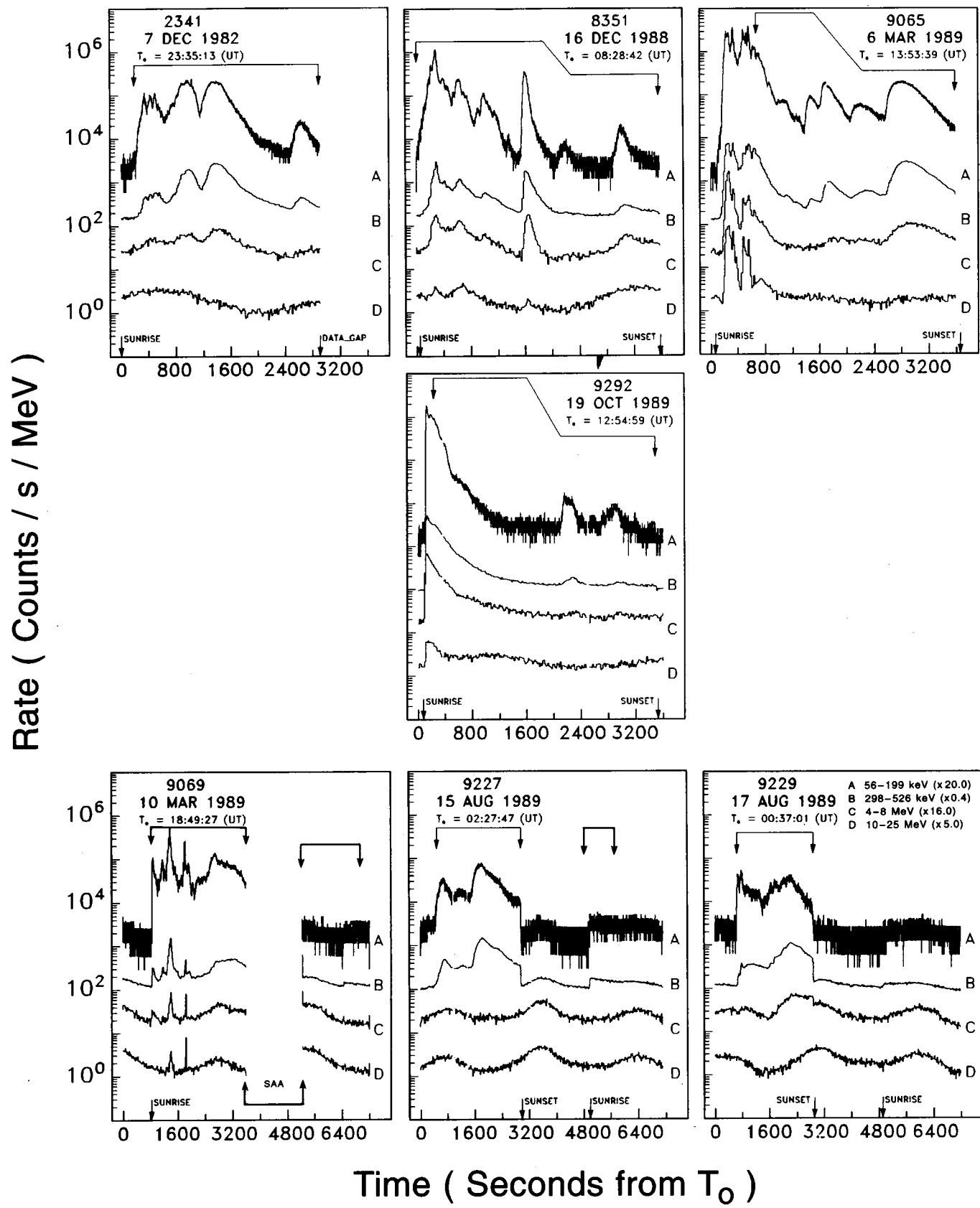


FIG. 23a

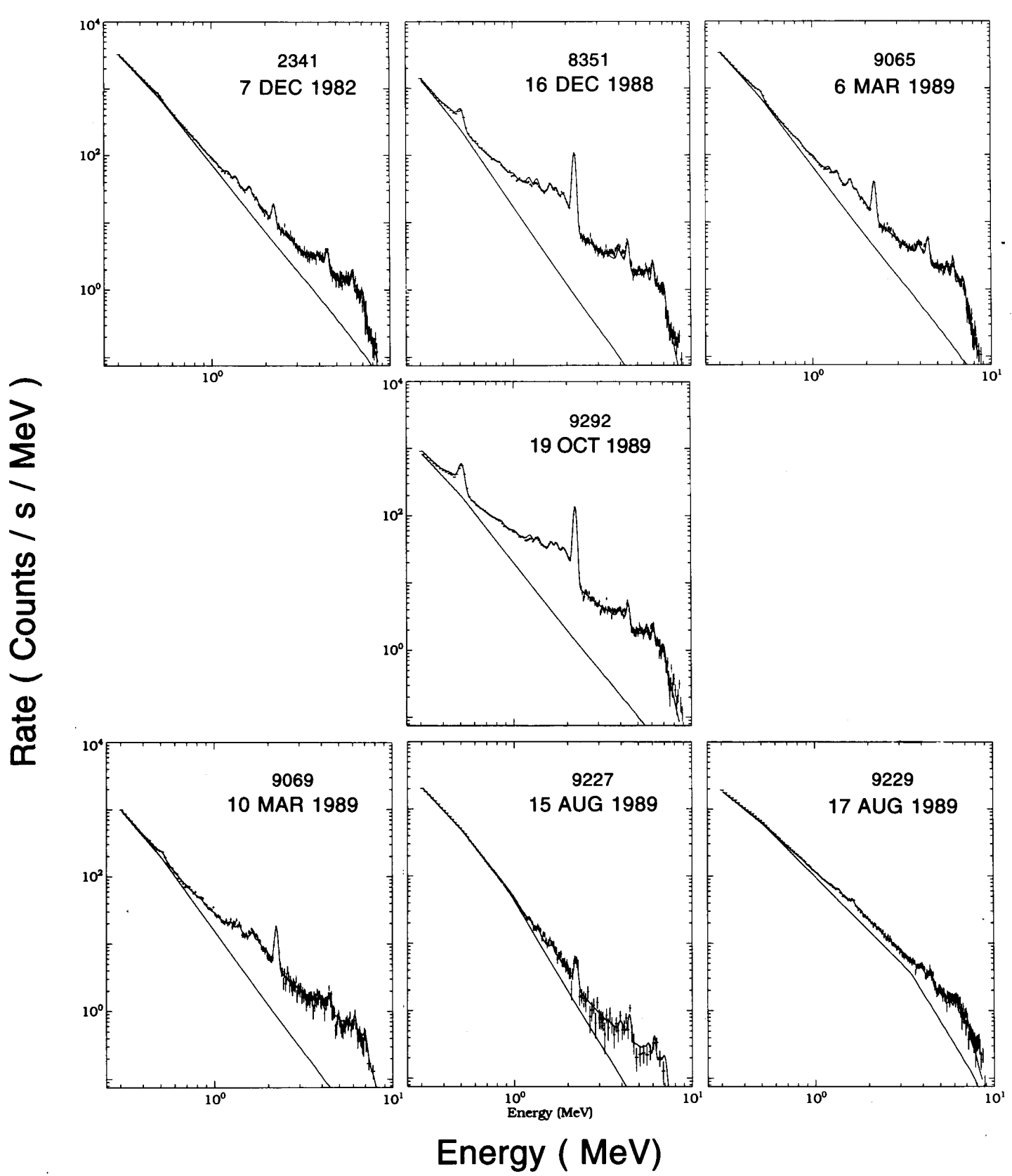


FIG. 23b